

## ABSTRACT

Title of dissertation:      **NUMERICAL STUDY OF PLASMON  
RESONANCES IN NANOPARTICLES**

Zhenyu Zhang, Doctor of Philosophy, 2007

Dissertation directed by:  Professor Isaak D. Mayergoyz  
Department of Electrical and Computer Engineering

Surface plasmon resonances in nanoparticles have numerous promising scientific and technological applications in such areas as nanophotonics, near-field microscopy, nano-lithography, biosensor, metamaterial and optical data storage. Consequently, the understanding of plasmon resonances in nanoparticles has both fundamental and practical significance. In this dissertation, a new numerical technique to fully characterize the plasmon resonances in three-dimensional nanoparticles is presented.

In this technique, the problem of determining the plasmon resonant frequencies is framed as an integral equation based eigenvalue problem, and the plasmon resonant frequencies can be directly found through the solution of this eigenvalue problem. For this reason, it is computationally more efficient than other “trial-and-error” numerical techniques such as the finite-difference time-domain (FDTD) method. This boundary integral equation method leads to fully populated discretized matrix equations that are computationally expensive to solve, especially when a large number of particles are involved in the nanostructures. Since the

fully populated matrices are generated by integrals with  $1/r$ -type kernel, this computational problem is appreciably alleviated by using the fast multipole method (FMM). The boundary integral approach is also extended to the calculation of the extinction cross sections of nanoparticles, which reveal important information such as the strength and the full width at half maximum (FWHM) of these resonances. The numerical implementation of this technique is discussed in detail and numerous computational results are presented and compared with available theoretical and experimental data.

Furthermore, metallic nanoshells for biosensing applications as well as nanoparticle-structured plasmonic waveguides of light are numerically investigated. The integral equation based numerical technique presented throughout this dissertation can be instrumental for the design of plasmon resonant nanoparticles and to tailor their optical properties for various applications.

NUMERICAL STUDY OF PLASMON RESONANCES  
IN NANOPARTICLES

by

Zhenyu Zhang

Dissertation submitted to the Faculty of the Graduate School of the  
University of Maryland, College Park in partial fulfillment  
of the requirements for the degree of  
Doctor of Philosophy  
2007

Advisory Committee:

Professor Isaak D. Mayergoyz, Chair/Advisor  
Dr. Nail A. Gumerov, Co-Advisor  
Professor Ramani Duraiswami  
Professor Perinkulam S. Krishnaprasad  
Professor Howard M. Milchberg  
Professor Thomas E. Murphy  
Professor Howard C. Elman

© Copyright by  
Zhenyu Zhang  
2007

# DEDICATION

To My Parents, Jianlin and Xinli.

## ACKNOWLEDGMENTS

First and foremost I would like to thank my advisor, Professor Isaak D. Mayergoyz for introducing me to the field of plasmonics and providing me an invaluable opportunity to work on the challenging and interesting problems over the past four years. He has always made himself available for help and advice. It has been a great pleasure to work with and learn from such an extraordinary individual.

I would also like to thank my co-advisors, Dr. Nail A. Gumerov and Professor Ramani Duraiswami. They have not only taught me the fast multipole method but also supported me in many ways. Thanks are due to my collaborators Professor Donald Fridkin from University of California, San Diego, Professor Gennady Shvets from the University of Texas at Austin and Professor Giovanni Miano of the University of Naples Federico II, Italy for numerous enlightening discussions.

I also wish to thank Professor Perinkulam S. Krishnaprasad, Professor Howard M. Milchberg, Professor Thomas E. Murphy and Professor Howard C. Elman for agreeing to serve on my dissertation committee and for taking their precious time reviewing the manuscript.

Furthermore, my friends and colleagues at the University of Maryland have enriched my graduate life in different ways and deserve a special mention: Mr. Seokjin Kim, Dr. Tao Shen, Dr. Heng-Tung Hsu, Dr. Su Li, Dr. Zhiyun Li, Mr. Patrick McAovy, Dr. Iulian Nistor, Dr. Mihai Dimian, Dr. Petru Andrei, and Dr.

Chun Tse.

I owe my deepest thanks to my family - my father and mother who have always been loving and supporting me during this long journey. Words can not express the gratitude I owe them.

College Park, April 2007

Zhenyu Zhang

# TABLE OF CONTENTS

List of Tables	viii
List of Figures	ix
<b>1 Introduction</b>	<b>1</b>
1.1 General overview . . . . .	1
1.2 Current state of the research . . . . .	6
1.3 Outline . . . . .	12
<b>2 Plasmon Resonances As an Eigenvalue Problem</b>	<b>14</b>
2.1 Theory of (electrostatic) plasmon resonances . . . . .	15
2.1.1 General considerations of (electrostatic) plasmon resonances .	15
2.1.2 Perturbation formulations . . . . .	17
2.1.3 Zero order solution . . . . .	19
2.1.4 First order correction . . . . .	25
2.1.5 Second order correction . . . . .	27
2.2 Comparison with the Mie theory for sphere . . . . .	29
2.2.1 Zero order solution . . . . .	30
2.2.2 Second order solution . . . . .	32
2.3 Numerical analysis of plasmon resonances in nanoparticles . . . . .	34
2.3.1 Numerical technique for solution of integral equation . . . . .	34
2.3.2 Numerical results . . . . .	36
2.4 Plasmon resonances in shell structures . . . . .	47
2.4.1 A generalized eigenvalue problem . . . . .	47
2.4.2 Analytical results for spherical and ellipsoidal shells . . . . .	52



<b>3</b>	<b>Fast Multipole Method for the Solution of Eigenvalue Problem</b>	<b>57</b>
3.1	Why fast multipole method is needed? . . . . .	58
3.2	Factorization and translations of the kernel function . . . . .	60
3.2.1	Factorization of the kernel function . . . . .	60
3.2.2	Translation in 3D . . . . .	62
3.2.3	Differentiation of the $\frac{1}{r}$ kernel in 3D . . . . .	65
3.3	FMM algorithm and implementation . . . . .	68
3.3.1	FMM algorithm . . . . .	68
3.3.2	Date structure for FMM implementation . . . . .	72
3.4	Numerical results . . . . .	76
3.5	Multipole expansion method for spherical nanoparticles . . . . .	82
3.5.1	The dual formulation for multiple spheres . . . . .	82
3.5.2	Multipole expansion method . . . . .	84
3.5.3	Numerical results . . . . .	92
<b>4</b>	<b>Extinction Cross Sections of Nanoparticles</b>	<b>94</b>
4.1	What is the extinction cross section ? . . . . .	95
4.1.1	Concept of extinction cross section . . . . .	95
4.1.2	The optical theorem . . . . .	98
4.1.3	Measurement of ECS . . . . .	99
4.2	Computation of ECS . . . . .	100
4.2.1	Near field computation . . . . .	100
4.2.2	Far field computation . . . . .	106
4.3	Numerical techniques to compute ECS . . . . .	108
4.3.1	Discretization of the inhomogeneous integral equation . . . . .	108

4.3.2	Far field and dipole moment . . . . .	109
4.3.3	Numerical results . . . . .	111
4.4	Numerical analysis of plasmon waveguides of light . . . . .	117
4.4.1	The numerical technique . . . . .	117
4.4.2	Numerical results . . . . .	120
5	<b>Conclusion</b>	126
	Bibliography	130

## LIST OF TABLES

2.1	Eigenvalues for a single nanosphere. . . . .	38
2.2	Eigenvalues for a single nanoellipsoid with aspect ratio 1:1:1.55. . . .	39
2.3	Comparison with experimental results [72] for gold nanoring. . . . .	41
2.4	Comparison with experimental results [42, 73] for gold ellipsoidal cylinder and triangular prism. . . . .	41
2.5	Comparison of the resonance wavelengths for Au spherical nanoshells with silicon cores. . . . .	50
2.6	Comparison of the resonance values of $\epsilon_+$ for spherical nanoshells, $\epsilon_1 = 5\epsilon_0$ . . . . .	53
2.7	Comparison of the resonance values of $\epsilon_+$ for ellipsoidal nanoshells, $\epsilon_1 = 15.2\epsilon_0$ . . . . .	55
3.1	Comparison of the resonance wavelengths for three silver spherical nanoparticle system. . . . .	77
3.2	Computation times in seconds. . . . .	82
3.3	Computed eigenvalue for two spheres with truncation number $p = 10$ . . . . .	91
3.4	Computed eigenvalue for two spheres with truncation number $p = 10$ using submatrix. . . . .	92
3.5	Comparison of numerical results of BEM and MEM for two-nanosphere and three-nanosphere configurations. . . . .	93
3.6	Comparison of computation costs of BEM and MEM for two-nanosphere and three-nanosphere configurations. . . . .	93
4.1	Resonance frequencies for gold 7-sphere-chain waveguide. . . . .	121

## LIST OF FIGURES

1.1	Darkfield image of plasmon resonant silver nanoparticles. . . . .	2
1.2	Schematic of plasmonic waveguide of light. . . . .	3
1.3	Local plasmon photonic transistor proposed in [21]. . . . .	4
2.1	Measured relative permittivity [68] of silver as a function of wavelength(frequency). . . . .	16
2.2	Measured relative permittivity [68] of gold as a function of wavelength(frequency). . . . .	16
2.3	The dielectric nanoparticle bounded by surface S. . . . .	17
2.4	Nanoparticles on substrate. The “dash particle” is the mirror image of the actual particle on the substrate (see formula (2.25)). . . . .	22
2.5	Surface charge distribution (eigenfunction) for the first 10 eigenmodes of single nanosphere. . . . .	39
2.6	Surface charge distribution (eigenfunction) for the first 10 eigenmodes of single nano-ellipsoidal. . . . .	40
2.7	Two nanospheres on substrate. . . . .	42
2.8	Resonance wavelength for two nanospheres on substrate. . . . .	42
2.9	Two ellipsoidal cylinders on substrate. . . . .	43
2.10	Resonance wavelength for two ellipsoidal cylinders on substrate. . . . .	43
2.11	The plasmon mode light intensity of first two resonance modes for triangular nanoprism, colorbars indicate the ratio of optical near field intensity normalized to incident fields. . . . .	44
2.12	Comparison of the plasmon resonance wavelength of (A) nanocube ensemble in water and (B) single nanocube on a glass substrate. The down arrows indicate the experimental results (432 nm and 452 nm in (A), 395 nm and 457 nm for (B)) while the up arrows show the computational results (420 nm and 478 nm in (A), 410 nm and 443 nm in (B)). . . . .	45
2.13	Examples of surface mesh used in computations for different geometry of three dimensional nanoparticles. . . . .	46

2.14	(a) Schematic of a nanoshell with dielectric core; (b) the equivalent problem for plasmon resonance in nanoshells. . . . .	48
2.15	Plasmon resonant wavelengths for Au spherical nanoshells with different shell thickness. The core of these shells is silicon. . . . .	51
3.1	Space partitioning. . . . .	59
3.2	Data structure. . . . .	59
3.3	Multipole expansion. . . . .	61
3.4	Local expansion. . . . .	62
3.5	Illustration of local-to-local ( $R R$ ), multipole-to-local ( $S R$ ), and multipole-to-multipole ( $S S$ ) translations from expansion center $\mathbf{r1}$ to expansion center $\mathbf{r2}$ (translation vector $\mathbf{t} = \mathbf{r2} - \mathbf{r1}$ ). The star shows location of a source. Expansion about center $\mathbf{r1}$ is valid inside the lighter and darker gray area, while expansion about center $\mathbf{r2}$ is valid only in the darker gray area. . . . .	63
3.6	Step 2 of FMM algorithm: Multipole to multipole translation. . . . .	69
3.7	Step 3 of FMM algorithm: Local to Local translation. . . . .	70
3.8	Step 3 of FMM algorithm: Multipole to local translation. . . . .	71
3.9	Step 3 of FMM algorithm: Multipole to local translation. . . . .	71
3.10	A flow chart of the standard FMM. . . . .	72
3.11	Hierarchical cells at three levels in three dimensions. . . . .	73
3.12	The CPU time in seconds required for computation of problems of size $N$ using direct method and FMM. FMM computations using truncation number $p = 5$ . Computation is performed on Dell workstation with Pentium 3.0 GHz processor, 4.0 GB RAM. . . . .	78
3.13	Absolute error vs truncation numbers $p^2$ for the case $N = 14496$ . Computation is performed on Dell workstation with Pentium 3.0 GHz processor, 4.0 GB RAM. . . . .	79
3.14	CPU times vs group parameters $s$ (number of points in the smallest box) for $N = 14496$ . Computation is performed on Dell workstation with Pentium 3.0 GHz processor, 4.0 GB RAM. . . . .	80
3.15	Three-sphere system for the nano-lens proposed in [83]. . . . .	81

3.16	The schematic of a 7-sphere cluster. . . . .	81
3.17	Multiple spherical nanoparticles located in proximity. . . . .	82
3.18	Points $\mathbf{x}$ and $\mathbf{y}$ are located at same sphere. . . . .	86
3.19	Points $\mathbf{x}$ and $\mathbf{y}$ are located at different spheres. . . . .	87
3.20	Truncation number as a function of the gap between two spheres. . .	90
4.1	Scattering diagram of a nanoparticle. . . . .	95
4.2	Schematic illustration for the measurement of extinction cross sections.	100
4.3	Computational results compared with the Mie theory predictions for the extinction cross section of a single Au nanoparticle (diameter = 10 nm). . . . .	112
4.4	Computational results compared with the Mie theory predictions for the extinction cross section of a single Ag nanosphere (diameter = 20 nm). . . . .	113
4.5	Computational results of the extinction cross section of a single Ag nanoellipsoid, with different aspect ratios: 1:1:0.8, 1:1:1, 1:1:1.2, 1:1:1.4, 1:1:1.6 for curve 1, 2, 3, 4, 5, respectively. . . . .	114
4.6	Computed extinction cross sections of Au nanorings placed on substrate, the dimensions of these rings are provided in Table 2.3. . . . .	115
4.7	Computational extinction cross section of a single InSb nanosphere (diameter = 20 nm) placed on a glass substrate $\epsilon = 2.25\epsilon_0$ . . . . .	116
4.8	Schematic of plasmonic waveguide of light. . . . .	118
4.9	Computed extinction cross sections of gold 7-sphere-chain waveguide for the transverse and longitudinal polarization modes (diameter = 50nm, center-to-center distance = 25nm). . . . .	122
4.10	Schematic of gold 11-sphere-chain waveguide of light . . . . .	123
4.11	Computed extinction cross sections of gold 11-sphere-chain waveguide for the longitudinal polarization mode (diameter = 50nm, center-to-center distance = 25nm). . . . .	123
4.12	Schematic of gold L-shape 11-sphere waveguide of light . . . . .	124

4.13	Computed extinction cross sections of gold L-shape 11-sphere waveguide for the longitudinal polarization mode (diameter = 50nm, center-to-center distance = 25nm). . . . .	124
4.14	Schematic of gold T-shape 11-sphere waveguide of light . . . . .	125
4.15	Computed extinction cross sections of gold T-shape 11-sphere waveguide for the longitudinal polarization mode (diameter = 50nm, center-to-center distance = 25nm). . . . .	125

## Chapter 1

### **Introduction**

#### 1.1 General overview

Due to their reduction of size and dimensionality, nanoparticles exhibit optical properties that differ in fundamental and valuable ways from the properties of individual atoms, molecules and bulk matter [1]. For example, the bright colors in stained glass windows or colloidal solutions are caused by small noble metallic particles [2]. This optical effect is due to the strong interaction between incident light and conduction electrons confined to the small volume of the metallic nanoparticle. Under the influence of an oscillating electric field, the negatively charged conduction electrons perform a collective motion with respect to the positive-ion background, creating an effective charge at the surface that results in a restoring force. The electron oscillations are therefore called surface plasmon resonances. The resonance modes are localized near the surface of the nanoparticle and exponentially decay along the depth from the surface. Surface plasmon resonances in metallic nanoparticles lead to strong light scattering and absorption and remarkable enhancement of local electromagnetic fields [3].

The optical properties of small metallic particles have fascinated many researchers in the past. For instance, Faraday first recognized that the red color in stained glasses is due to small-sized Au particles in 1857, and this peculiar phenom-



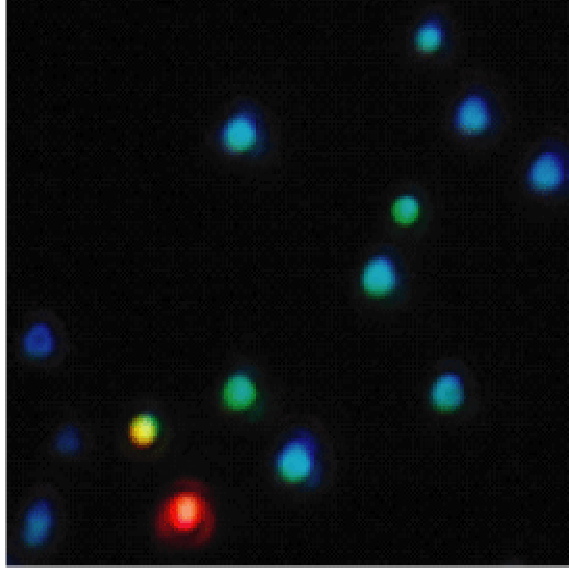


Figure 1.1: Darkfield image of plasmon resonant silver nanoparticles.

enon was theoretically explained by the groundbreaking work of Mie in 1908 [4]. Nevertheless, the research on surface plasmon resonances has increased in volume considerably in the past decade. This recent revival of interest is caused by the advances and new capabilities in fabrication methods to produce metallic nanostructures of well-defined sizes and shapes [5, 6, 7], and subsequently the possibilities to utilize plasmon resonant nanoparticles in scientific and technological applications ranging from optics and sensors to biology and medicine.

A key feature of plasmonic nanostructures is that light can be confined and manipulated on a scale below the diffraction limit governed by conventional optics [8]. This opens opportunities for new optical devices and technology. For example, plasmon-resonant metal nanoparticles can be used to construct miniature optical waveguides. The plasmon waveguides consist of arrays (chains) of metallic nanoparticles (see Figure 1.2) with their plasmon resonance frequencies in the region of

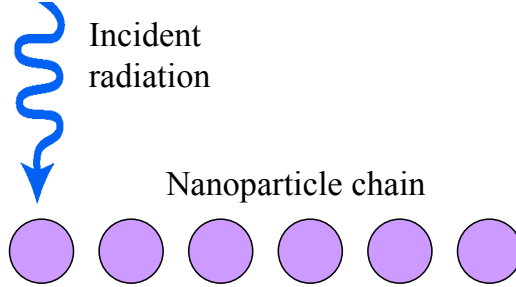


Figure 1.2: Schematic of plasmonic waveguide of light.

optical waveguiding. At specific frequencies, incident optical radiation can excite plasmon resonances in the first nanoparticle, which then through near-field coupling can induce plasmon resonances in all nanoparticles that form the chain [9]. Atwater et al have demonstrated that optical signals can propagate over a micrometer along the waveguide [10, 11, 12]. Surface plasmon resonances can also be exploited in the field of optical lithography for the fabrication of nanoscale features beyond the diffraction limit [13, 14, 15]. By using a photoresist that is sensitive at the surface plasmon resonant frequency, the exposure of a thin layer of photoresist directly below a contact mask can create an aerial image on nanometer length scales. This surface plasmon resonant nanolithography technique is not diffraction limited, and can produce subwavelength features using broad beam illumination with visible light.

Another salient feature associated with plasmon resonances is the strong local field enhancement. For instance, plasmon-resonant metallic nanoparticles have been used in surface enhanced Raman spectroscopy [16, 17, 18]. Moreover, active photonic devices have been proposed which utilize plasmon resonances. Mayergoyz and

Fredkin [19, 20] suggested that the optical controllability of semiconductor nanoparticles can be utilized for the development of nanoscale light switches and all-optical nanotransistors. On the other hand, Tominnaga and co-workers [21] showed that by focusing two laser beams (405 and 635 nm) in one small spot on a high-speed rotating optical disk, a large signal enhancement is observed (Figure 1.3). It was found that a plasmon interaction generated between a silver light-scattering nanoparticle and small marks recorded in the optical disk with a super-resolution near-field structure produced the large signal amplification in the spot ( $< 1 \mu\text{m}$ ). A modulated signal of the blue laser was enhanced by 60 times by controlling the red laser power from 1.5 to 3.5 mW. It has been shown that the system has the potential to realize all-thin-films photonic transistors by using local plasmon amplification.

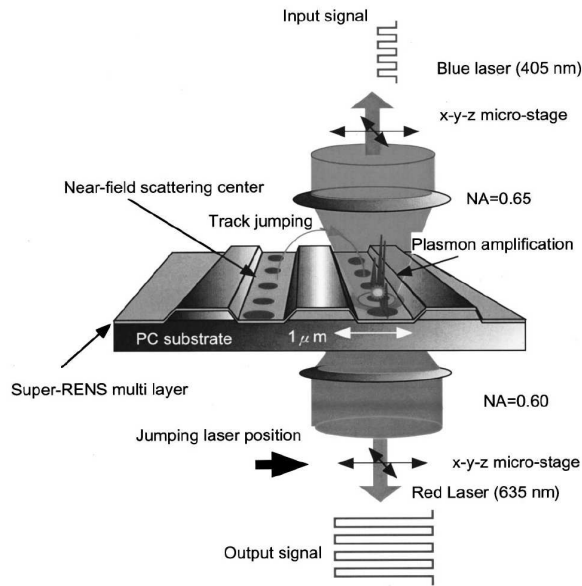


Figure 1.3: Local plasmon photonic transistor proposed in [21].

Surface plasmon resonances are very sensitive to the local dielectric environ-

ment. In other words, a small change of the refractive index of surrounding medium will result in appreciable shift of plasmon resonant frequencies as well as the extinction coefficients. A variety of nanoscale biosensors have been demonstrated based on this principle [22, 23, 24]. For example, Storhoff and Mirkin linked a single-stranded DNA to a gold nanoparticle of 15 nm in diameter. When this DNA hybridizes with its complementary DNA in the test sample, the duplex formation leads to aggregation of nanoparticles, shifting the plasmon resonance from burgundy-red color (single nanoparticle) to blue black (aggregation of nanoparticles) [25, 26]. In a similar manner, Halas and co-workers used gold nanoshells to demonstrate a rapid immunoassay, capable of detecting analyte within a complex biological media such as blood [27, 28].

Another area which attracts considerable interest lately is the design and engineering of metamaterials. Metamaterials are artificial composite materials that have negative permeability and permittivity simultaneously, also known as left-handed or double negative materials [29]. Due to their unique electromagnetic properties, metamaterials are promising for many optical and microwave applications, such as perfect lenses, transmission lines, and antennas. It is well known that many metals (e.g. silver and gold) have negative  $\epsilon$  at visible wavelengths. Relying on the plasmon resonances of individual metallic nanoparticles and arranging the geometry of composite inclusions to resemble magnetic nanoloops, negative  $\mu$  and left-handed metamaterials with a negative index of refraction in the optical frequency range can be realized [30, 31].

In addition to the aforementioned applications, the surface plasmon resonance

also has potential in next generation optical storage [32, 33, 34], scanning near-field optical microscopy [35, 36] and energy solar cells [37, 38]. Since the understanding of the optical properties of metallic nanoparticles holds both fundamental and practical significance, it is important to have the capability to model and predict the plasmon resonance behavior of nanoparticles with complex shape. The goal of this dissertation is to present a new and efficient method for the analysis of plasmon resonances in nanoparticles.

## 1.2 Current state of the research

In the classical picture, the optical property of nanoparticles is treated as a scattering problem, which can be described by Maxwell's equations. In this framework, the complete description of the material properties is included in the dispersion relation, which gives the complex permittivity  $\epsilon(\omega)$  as a function of the frequency or wavelength. At specific negative permittivity values, plasmon resonances will be excited in these small particles. These specific permittivity values strongly depend on the particle shape, size and surrounding medium, since the boundary conditions imposed by Maxwell's equations determine whether such a particle resonance can build up. One may wonder whether the classical description of the material based solely on Maxwell's equations and bulk dispersion relations is appropriate for the small particles. In fact, it has been experimentally demonstrated that this macroscopic approach is adequate for particle dimensions as small as a few nanometers [3, 39]. Furthermore, this question has been discussed in a recent paper by Levi

et al [40]. According to their quantum mechanical computations, it can be concluded that there is no appreciable discrepancy between quantum model and classic electrodynamics for particle size above 8 nanometers.

The optical properties of small spherical metallic particles accounting for the surface plasmon resonance were first explained theoretically by the groundbreaking work of Mie in 1908 [4]. Mie solved Maxwell's equations for an electromagnetic light wave interacting with a small sphere that has the same macroscopic, frequency-dependent material dielectric constant as the bulk metal. Mie's electrodynamics computation gave a series of multipole oscillations for the extinction and scattering cross sections of the particles as a function of the particle radius. For small but finite-sized particles, Mie theory gives the resonance values of dielectric permittivity of the spherical particle as [39]:

$$\epsilon_+ = - \left( 2 + \frac{12}{5} \omega^2 \mu_0 \epsilon_0 a^2 \right) \epsilon_0, \quad (1.1)$$

where  $\omega$  is the angular frequency of the optical radiation,  $a$  is the radius of the sphere, and  $\mu_0$  and  $\epsilon_0$  have their usual meaning. Mie's results are still widely used today since it is the only available analytical solution and most of the nanoparticles produced by the colloidal or wet chemistry method are more or less spherical.

As soon as one considers particles other than spheres or even spheres within an asymmetric dielectric environment, it is usually not possible to obtain analytical solutions to Maxwell's equations. Due to this fact, there has been a great deal of effort put into developing numerical methods. Indeed, the literature on numerical methods for classical electrodynamics problem is enormous. However, there are some

important challenges and simplifications associated with metallic nanoparticles that limit the applicability of methods used to study problems with much longer wavelength and length scales. In recent years, there are several numerical techniques that have been used to describe optical properties of non-spherical metallic nanoparticles. They can be briefly summarized as follows.

(1) Discrete dipole approximation (DDA) method. Schatz and co-workers [41, 42] have applied the DDA method to non-spherical nanoparticles which can be traced to Purcell [43] and Draine [44]. In DDA, a particle with arbitrary shape is treated as a three-dimensional assembly of dipoles on a cubic grid. Each dipole cell is assigned a complex polarizability  $\alpha_i$  which can be computed from the complex dispersion relation and the number of dipoles in a unit volume. This polarizability causes an oscillating dipole moment or a polarization  $\mathbf{P}_i$  at each cell, depending on the total electric field at the respective position and given by

$$\mathbf{P}_i = \alpha_i \cdot \mathbf{E}_i. \quad (1.2)$$

The total field  $\mathbf{E}_i$  is the sum of the incident field  $\mathbf{E}_{inc,i}$  (usually a plane wave) and a contribution from all other dipoles  $\mathbf{E}_{dip,i}$ :

$$\mathbf{E}_i = \mathbf{E}_{inc,i} + \mathbf{E}_{dip,i} = \mathbf{E}_0 e^{i\mathbf{k}\cdot\mathbf{r}_i} + \sum_{i \neq j} \mathbf{A}_{ij} \cdot \mathbf{P}_j. \quad (1.3)$$

The matrix  $\mathbf{A}_{ij}$  includes the interaction of all dipoles depending on the distance of the dipoles; thus, a full dense matrix results. This equation can be solved by iteration. Once the polarizations  $\mathbf{P}_i$  are found, the extinction and absorption cross sections can be computed by using standard formulas. The DDA technique has been applied to different shape of nanoparticles and was able to reproduce the

spectral shape of the plasmon resonances. It has two weaknesses, however. The total volume of material that can be described is limited by available computer resources to dimensions of a few hundred nanometers and the electric fields close to particle surface are inaccurate [41].

(2) Finite-difference time-domain (FDTD) methods. The popular FDTD technique has also been used for the modeling of plasmon resonances [45, 46, 47]. In this technique, the Maxwell's equations in differential form are solved directly. The space and time are both discretized and a difference approximation is applied to evaluate the space and time derivatives of the field. The equations are solved in a leap-frog manner; that is, the electric field is solved at a given instant in time, then the magnetic field is solved at the next instant in time, and the process is repeated over and over again. Although the FDTD technique is rather versatile and easy to implement, it has several drawbacks as far as the analysis of plasmon resonance modes in nanoparticles is concerned. First, it is a “probing” technique when a nanoparticle is “numerically probed” many times by incident radiation of different frequencies and polarizations. In other words, FDTD is a “trial-and-error” approach to the analysis of plasmon resonance modes in nanoparticles, and this is detrimental to the effectiveness of FDTD for plasmon mode computations. Second, FDTD requires discretization of three-dimensional space, since only a finite region of three-dimensional space can be discretized and used in computations, FDTD requires the introduction of artificial external boundaries and special absorbing boundary conditions on these boundaries to minimize distortions and errors caused by the introduction of artificial boundaries. Finally, plasmon resonances occur in dispersive dielectric media with



non-instantaneous in time (convolution-type) constitutive relations between electric displacement and electric field. These non-instantaneous constitutive relations lead to finite difference schemes with the electric field coupling at all previous time-steps. This past history coupling of electric field diminishes the effectiveness of FDTD for plasmon resonance computations.

(3) T-matrix method [48, 49, 50]. In T-matrix method, the incident and scattered electric fields are expanded in series of suitable vector spherical wave functions, and the relation between the columns of the respective expansion coefficients is established by means of a transition matrix (or T-matrix). The elements of the T-matrix are independent of the incident and scattered electric fields and only depend on the shape, size, refractive index of the particle as well as its orientation with respect to the reference frame. These elements are obtained by numerical integration. While the T-matrix method is very accurate and powerful, it suffers from two major disadvantages. First, for a particle with arbitrary shape, the elements of T-matrix have to be computed through a surface integral. As this is computationally expensive, most implementations of this method are restricted to axisymmetric scatterers. In this case, the surface integrals can be reduced to line integrals. Second, the numerical stability of this method is compromised for highly aspherical particles, for which the convergent size of the T-matrix should be large, and T-matrix computations may converge very slowly or even diverge.

(4) Multiple multipole (MMP) method [51, 52, 53]. In MMP method, the fields in the individual domains of the structure under investigation are described by series expansion of known analytical solutions of Maxwell equations (multipole functions,

plane waves, waveguide modes, etc.). Each solution has a free parameter that can be determined from the boundary conditions to be satisfied in a suitably selected set of points on the interfaces between the domains. Usually more conditions than free parameters are used, and the resulting over-determined system of equations is solved in the least-squares sense. With this procedure a smooth error distribution is obtained on the boundaries, and one can evaluate the errors in the individual boundary points to estimate the quality of the solution. Note that Maxwell equations are exactly fulfilled inside the domains but are only approximated on the boundaries. In this case, the computational effort varies with the number of matching points, expansion functions, and basis functions used in the expansions. The computational advantage of the MMP is that only the boundaries need to be discretized and not the domains themselves.

It can be seen that by using the above mentioned methods, plasmon resonances in metallic nanoparticles are found numerically by using a “trial-and-error” method, i.e., by probing metallic nanoparticles of complex shapes with radiation of various frequencies and polarizations. A mode-based approach and the direct calculations of plasmon resonance modes are clearly preferable. In this dissertation, an integral equation based numerical technique is presented to fully characterize the plasmon resonances in nanoparticles [9, 20, 58, 59, 60, 61, 62, 63]. The basic idea of the technique is to frame the plasmon resonance as an integral equation based eigenvalue problem, which was proposed by Mayergoyz and Fredkin [19] and can be traced back to publications of Mayergoyz [54, 55]. The integral equation technique has been also used for the analysis of plasmon resonances in a limited form by Ouyang

and Isaakson [56, 57]. By using this technique, the plasmon resonance modes and resonant frequencies of three dimensional nanoparticles can be computed directly at the quasi-electrostatic limit by solving an eigenvalue problem for specific homogeneous surface integral equations. The calculation of high order corrections which counts for the finite wavelength nature of radiation has been developed through perturbation technique. The integral equation technique has been also extended to the computation of extinction cross-sections of nanoparticles, where the problem is reduced to the solution of an inhomogeneous integral equation. Furthermore, in this dissertation work, the fast multipole method (FMM) [64, 65] is applied for the large scale eigenvalue problem to reduce the computational cost from  $O(N^2)$  to  $O(N \log N)$  which is a great advance when  $N$  is large. For these reasons, the integral equation based numerical technique is very efficient and can be instrumental for the design of plasmon resonant nanoparticles and to tailor their optical properties for various applications.

### 1.3 Outline

This dissertation is organized as follows. Chapter 2 presents the basic idea of the electrostatic (plasmon) resonance (ESR) model. It is shown that the plasmon resonant frequency of a nanoparticle can be directly computed through the solution of an integral equation based eigenvalue problem. The technique for the discretization of the integral equation is discussed and numerous numerical results are presented and compared with theoretical results as well as available experimental

data for various three-dimensional nanoparticles. In the last part of this chapter, the ESR model is extended for the analysis of plasmon resonances in metallic nanoshells, which is very promising for biological sensing applications.

The numerical aspect of computations of the eigenvalue problem is considered in Chapter 3. The fast multiple method (FMM) is introduced for the large scale eigenvalue problem. The applicability of FMM and its implementation in the iterative algorithm are presented in detail. Numerical results which illustrate the efficiency of FMM and a comparison with traditional methods for the numerical analysis of plasmon resonances are presented. In addition, a semi-analytical method based on multipole expansions is developed for the analysis of plasmon resonances in spherical nanoparticles.

In Chapter 4, the computation of extinction cross sections (ECS) of nanoparticles is demonstrated. In this chapter, the plasmon resonance in nanoparticles is treated as a scattering problem. It is shown that the scattered electromagnetic fields can be obtained via the solution of an inhomogeneous integral equation and then the ECS is computed by invoking the optical theorem. Simulation results are presented and compared with theoretical results and available experimental data for three-dimensional nanoparticles. In the last section of Chapter 4, the plasmonic waveguide of light is discussed and numerically investigated.

Finally, conclusions and further work are presented in Chapter 5.

## Chapter 2

### **Plasmon Resonances As an Eigenvalue Problem**

In this chapter, the theory and numerical analysis of (electrostatic) plasmon resonance modes in three-dimensional nanoparticles is presented. It is shown that the problem of determining plasmon resonance modes in nanoparticles can be treated as an integral-equation-based classical eigenvalue problem, and the plasmon resonant frequencies can be directly found through the solution of this eigenvalue problem (sections 2.1). It is also demonstrated that radiation corrections due to finite sizes of nanoparticles can be computed through perturbation technique. The comparison between this method and the Mie theory for spherical nanoparticle is demonstrated in section 2.2. The numerical technique to solve the integral equation as well as the numerical analysis of plasmon resonances in three-dimensional nanoparticles are presented in section 2.3. Finally, the integral equation technique is extended to the generalized eigenvalue problem for the analysis of nanoshell structures in section 2.4.

## 2.1 Theory of (electrostatic) plasmon resonances

### 2.1.1 General considerations of (electrostatic) plasmon resonances

It is known that plasmon resonances in nanoparticles occur at specific frequencies for which the particle permittivity is negative and the free-space wavelength of the radiation is large in comparison with particle dimensions. The latter condition suggests that these resonances are electrostatic in nature. Indeed, since particle dimensions are small compared to the free-space wavelength of the radiation (when resonances occur), time-harmonic electromagnetic fields within the nanoparticles and around them vary almost with the same phase. As a result, at any instant of time these fields look like electrostatic fields. Therefore, in the study of plasmon resonances in nanoparticles, we shall follow the traditional approach where all losses are first neglected and resonance frequencies are found for lossless systems as frequencies for which source-free electromagnetic fields may exist. This approach leads to the consideration of resonances in the electrostatic limit where all radiation losses are first neglected. When the dielectric permittivity of nanoparticles is negative, the uniqueness theorem of electrostatics is broken. For this reason, source-free electrostatic fields may appear for certain negative values of dielectric permittivities, which is the manifestation of resonances. The frequencies corresponding to the above negative values of permittivity are the resonance frequencies.

It is clear from the previous discussion that electrostatic resonances may occur only in particles whose media exhibit dispersion and the real part of the permittivity assumes negative value for some range of frequencies. For metals, this frequency

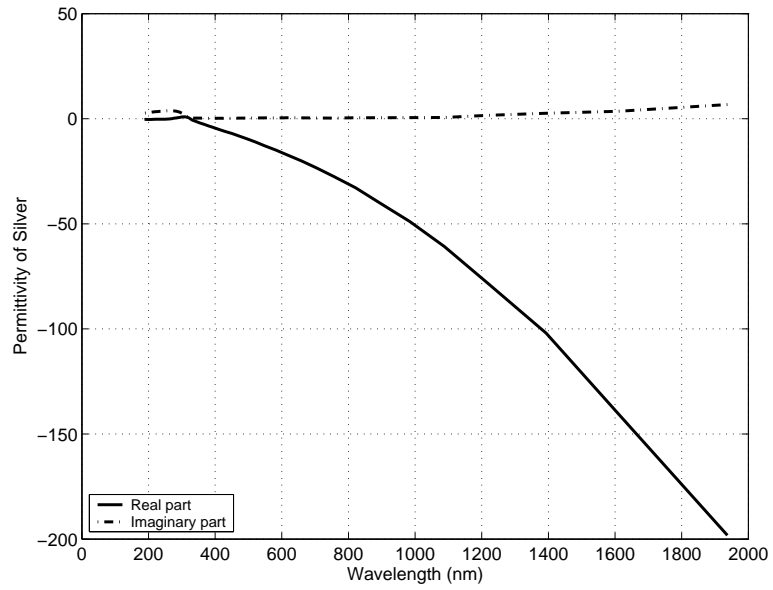


Figure 2.1: Measured relative permittivity [68] of silver as a function of wavelength(frequency).

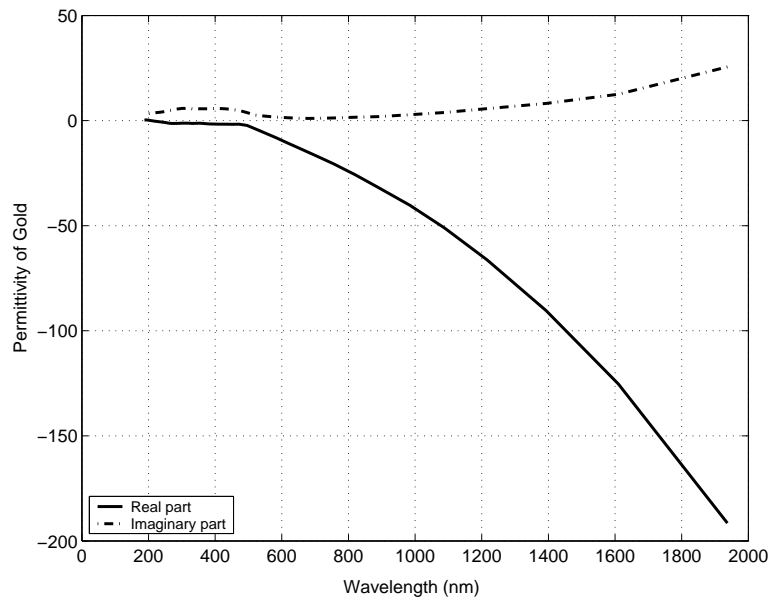


Figure 2.2: Measured relative permittivity [68] of gold as a function of wavelength(frequency).

range is below the plasma frequencies  $\omega_p$ , but at sufficiently high frequencies for collisions to be unimportant. The dispersion relation of many metals (but not all) can be well described by the Drude model:

$$\epsilon(\omega) = \epsilon_0 \left[ 1 - \frac{\omega_p^2}{\omega(\omega + i\gamma)} \right], \quad (2.1)$$

$$\omega_p^2 = \frac{n_e e^2}{\epsilon_0 m_e}. \quad (2.2)$$

where  $\gamma$  is the damping factor or electron relaxation rate. The most commonly used data from literature for  $\epsilon(\omega)$  are the tables in Paliks Handbook of Optical Constants [69] and the tables by Johnson and Christy [68]. As an example, the dispersion relations for silver and gold [68] are shown in Figures 2.1 and 2.2, respectively.

### 2.1.2 Perturbation formulations

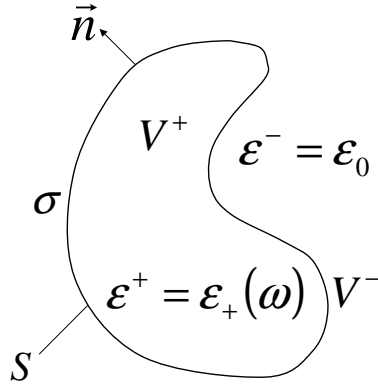


Figure 2.3: The dielectric nanoparticle bounded by surface  $S$ .

Consider a nanoparticle of arbitrary shape with uniform dielectric permittivity  $\epsilon_+(\omega)$  (Fig. 2.3). We are interested in negative values of  $\epsilon_+(\omega)$  for which a source-free electromagnetic field may exist. To find such permittivities, we shall start with



Maxwell equations in term of the vectors (where  $e^{-i\omega t}$  is assumed for  $\mathbf{E}$ ,  $\mathbf{H}$ ,  $\mathbf{e}$ ,  $\mathbf{h}$ ):

$$\mathbf{e} = \epsilon_0^{\frac{1}{2}} \mathbf{E}, \quad \mathbf{h} = \mu_0^{\frac{1}{2}} \mathbf{H} \quad (2.3)$$

and spatial coordinates scaled by the general diameter  $d$  of the nanoparticle. This leads to the following boundary value problem:

$$\nabla \times \mathbf{e}^+ = -i\beta \mathbf{h}^+, \quad \nabla \times \mathbf{h}^+ = i \frac{\epsilon_+}{\epsilon_0} \beta \mathbf{e}^+, \quad (2.4)$$

$$\nabla \cdot \mathbf{e}^+ = 0, \quad \nabla \cdot \mathbf{h}^+ = 0, \quad (2.5)$$

$$\nabla \times \mathbf{e}^- = -i\beta \mathbf{h}^-, \quad \nabla \times \mathbf{h}^- = i\beta \mathbf{e}^-, \quad (2.6)$$

$$\nabla \cdot \mathbf{e}^- = 0, \quad \nabla \cdot \mathbf{h}^- = 0, \quad (2.7)$$

$$\mathbf{n} \times (\mathbf{e}^+ - \mathbf{e}^-) = 0, \quad \mathbf{n} \times (\mathbf{h}^+ - \mathbf{h}^-) = 0, \quad (2.8)$$

$$\mathbf{n} \cdot \left( \frac{\epsilon_+}{\epsilon_0} \mathbf{e}^+ - \mathbf{e}^- \right) = 0, \quad \mathbf{n} \cdot (\mathbf{h}^+ - \mathbf{h}^-) = 0, \quad (2.9)$$

where superscripts “+” and “-” are used for physical quantities inside ( $V^+$ ) and outside ( $V^-$ ) the nanoparticle, respectively,  $\mathbf{n}$  is the outward unit normal to  $S$ , and

$$\beta = \omega \sqrt{\mu_0 \epsilon_0} d. \quad (2.10)$$

Since the free-space wavelength  $\lambda$  is large in comparison with the dimension of nanoparticle,  $\beta$  can be treated as a small parameter and source-free solutions of the boundary value problem (2.4)–(2.9) and dielectric permittivities  $\epsilon_+(\omega)$  at which they occur can be expanded in terms of  $\beta$ :

$$\mathbf{e}^\pm = \mathbf{e}_0^\pm + \beta \mathbf{e}_1^\pm + \beta^2 \mathbf{e}_2^\pm + \dots, \quad (2.11)$$

$$\mathbf{h}^\pm = \mathbf{h}_0^\pm + \beta \mathbf{h}_1^\pm + \beta^2 \mathbf{h}_2^\pm + \dots, \quad (2.12)$$

$$\epsilon_+ = \epsilon_+^{(0)} + \beta\epsilon_+^{(1)} + \beta^2\epsilon_+^{(2)} + \dots \quad (2.13)$$

By substituting formulas (2.11)–(2.13) into equations (2.4)–(2.7) as well as boundary conditions (2.8)–(2.9) and equating terms of equal powers of  $\beta$ , we can obtain the boundary value problems for  $\mathbf{e}_k^\pm$  and  $\mathbf{h}_k^\pm$  ( $k = 0, 1, 2, \dots$ ).

### 2.1.3 Zero order solution

For zero-order terms, these boundary value problems are written in terms of  $\mathbf{E}_0^\pm = \epsilon_0^{-\frac{1}{2}}\mathbf{e}_0^\pm$  and  $\mathbf{H}_0^\pm = \mu_0^{-\frac{1}{2}}\mathbf{h}_0^\pm$  as follows:

$$\nabla \times \mathbf{E}_0^\pm = 0, \quad \nabla \cdot \mathbf{E}_0^\pm = 0, \quad (2.14)$$

$$\mathbf{n} \times (\mathbf{E}_0^+ - \mathbf{E}_0^-) = 0, \quad \mathbf{n} \cdot \left( \frac{\epsilon_+^{(0)}}{\epsilon_0} \mathbf{E}_0^+ - \mathbf{E}_0^- \right) = 0, \quad (2.15)$$

and

$$\nabla \times \mathbf{H}_0^\pm = 0, \quad \nabla \cdot \mathbf{H}_0^\pm = 0, \quad (2.16)$$

$$\mathbf{n} \times (\mathbf{H}_0^+ - \mathbf{H}_0^-) = 0, \quad \mathbf{n} \cdot (\mathbf{H}_0^+ - \mathbf{H}_0^-) = 0. \quad (2.17)$$

From equations (2.16) and (2.17), it is clear that:

$$\mathbf{H}_0^\pm = 0. \quad (2.18)$$

To solve  $\mathbf{E}_0$  from (2.14)–(2.15), an electric potential  $\varphi$  can be introduced for this source-free electric field and the potential can be represented as the electric potential of single layer of electric charges  $\sigma$  distributed over the boundary  $S$  of the particle (Fig. 2.3):

$$\varphi(Q) = \frac{1}{4\pi\epsilon_0} \oint_S \frac{\sigma(M)}{r_{MQ}} dS_M, \quad (2.19)$$

where  $Q$  and  $M$  are the observation point and integration point on boundary  $S$ , respectively. In other words, a single layer of electric charges on  $S$  may create the same electric field in the free space as the source-free electric field that may exist in the presence of the dielectric nanoparticle with negative permittivity. It is clear that the electric field of surface charges  $\sigma$  is curl and divergence free in  $V^+$  and  $V^-$  and satisfies the first boundary condition in (2.15). Next, we recall that the normal components of electric field induced by surface electric charges are given by the formulas[70, 71]:

$$\mathbf{n}(Q) \cdot \mathbf{E}_0^\pm(Q) = \mp \frac{\sigma(Q)}{2\epsilon_0} + \frac{1}{4\pi\epsilon_0} \oint_S \sigma(M) \frac{\mathbf{r}_{MQ} \cdot \mathbf{n}_Q}{r_{MQ}^3} dS_M. \quad (2.20)$$

By substituting formulas (2.20) into the second boundary condition (2.15), after simple transformations we arrive at the following homogeneous boundary integral equation:

$$\sigma(Q) = \frac{\lambda}{2\pi} \oint_S \sigma(M) \frac{\mathbf{r}_{MQ} \cdot \mathbf{n}_Q}{r_{MQ}^3} dS_M, \quad (2.21)$$

where the eigenvalue  $\lambda$  (not wavelength) is defined by:

$$\lambda = \frac{\epsilon_+^{(0)}(\omega) - \epsilon_0}{\epsilon_+^{(0)}(\omega) + \epsilon_0}. \quad (2.22)$$

Thus, source-free electric fields may exist only for such values of permittivity  $\epsilon_+^{(0)}$  that the integral equation (2.21) has nonzero solutions. In other words, in order to find the resonance values of  $\epsilon_+^{(0)}$  (and the corresponding resonance frequencies) as well as resonance modes, the eigenvalues and eigenfunctions of the integral equation (2.21) must be computed. Integral equation (2.21) and its spectrum for the calculations of electrostatic and scattering problem with negative  $\epsilon$  were extensively studied in

publications of Mayergoyz [54, 55] and later introduced for the analysis of plasmon resonances by Ouyang and Isaacson [56, 57]. Then it was greatly expanded in publications [19, 9, 20, 58, 59, 60, 61, 62, 63]

For particles of complex shapes the resonance frequencies and resonance modes can be found through numerical solution of integral equation (2.21). If the boundary  $S$  of the particle is not smooth, then  $\sigma(M)$  may have singularities at the corners and the edges of  $S$  that may negatively affect the accuracy of numerical computations. In this situation, the dual formulation can be employed, where dipole (double layer of electric charges) density  $\tau(M)$  is distributed over  $S$  in such a way that it creates the same electric displacement field ( $\mathbf{D}_0$ ) in free space as the source-free electric displacement field that may exist in the presence of the dielectric particle with negative permittivity. By using the known properties of double-layer potential[70, 71], it can be shown that the two displacement fields mentioned above will be identical if the dipole density  $\tau(M)$  satisfies the following homogeneous boundary integral equation:

$$\tau(Q) = \frac{\lambda}{2\pi} \oint_S \tau(M) \frac{\mathbf{r}_{QM} \cdot \mathbf{n}_M}{r_{QM}^3} dS_M, \quad (2.23)$$

where  $\lambda$  is given by formula (2.22). It is apparent that the boundary integral equation (2.23) is adjoint to the integral equation (2.21). For this reason, it has the same spectrum as one can expect on the physical grounds. The dipole density  $\tau(M)$  is proportional to the discontinuity of double-layer potential across  $S$  and, consequently, it is finite even for non-smooth boundaries  $S$ . This is the advantage of integral equation (2.23) for numerical computations with non-smooth boundaries

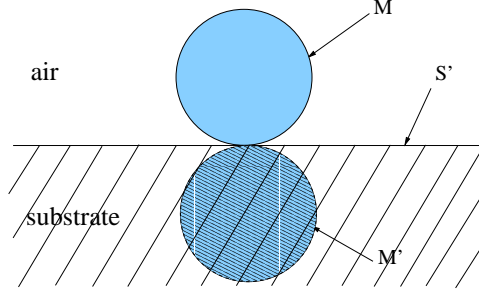


Figure 2.4: Nanoparticles on substrate. The “dash particle” is the mirror image of the actual particle on the substrate (see formula (2.25)).

$S$ . In applications, nanoparticles are usually placed on dielectric substrates (see Fig. 2.4). In this case, the integral equation (2.21) can be modified as follows:

$$\sigma(Q) = \frac{\lambda}{2\pi} \oint_S \sigma(M) \mathbf{n}(Q) \cdot \nabla_Q [G(Q, M)] dS_M, \quad (2.24)$$

where  $\lambda$  is given by formula (2.22), while  $G(M, Q)$  is the Green function defined by the formula:

$$G(Q, M) = \frac{1}{r_{MQ}} - \frac{\epsilon - \epsilon_0}{\epsilon + \epsilon_0} \frac{1}{r_{M'Q}} \quad (2.25)$$

Here,  $\epsilon$  is the permittivity of the substrate and  $M'$  is the image of  $M$  with respect to the substrate plane  $\tilde{S}$ .

The presented discussion can be easily extended to the analysis of electrostatic (plasmon) resonances of several particles located in proximity to one another. In this case  $S$  in integral equations (2.21) and (2.23) must be construed as the union of boundaries of all dielectric particles, while  $\sigma(M)$  (and  $\tau(M)$ ) are defined on this union. It has to be noted, however, as the number of nanoparticles increases, the computational cost for solving the integral equations (2.21) and (2.23) becomes very expensive and this bottleneck problem will be addressed in Chapter 3.

The kernels in integral equations (2.21) and (2.23) have weak (integrable in the usual sense) singularities. For this reason, the integral operators in the above integral equations are compact. This implies that the plasmon spectrum is discrete despite the infinite region of field distribution. It has been proved [70, 71] that the spectrum of integral equation (2.21) has the following properties: for any shapes of  $S$  all eigenvalues are real,  $\lambda = 1$  is an eigenvalue, and for all other eigenvalues  $|\lambda| > 1$ . It is apparent from (2.21) that the eigenvalue  $\lambda = 1$  corresponds to the case of  $\epsilon_+^{(0)} \rightarrow \infty$ , and the respective eigenfunction  $\sigma(M)$  can be construed as the distribution of surface electric charges over the boundary  $S$  of a conductor  $V^+$ . This eigenvalue is irrelevant as far as the discussion of electrostatic (plasmon) resonances is concerned. All other eigenvalues correspond to source-free (resonance) configurations of electrostatic fields and, according to (2.21), these configurations may exist (as expected) only for negative values of  $\epsilon_+^{(0)}$ . After these negative resonance values of  $\epsilon_+^{(0)}$  are found through the solution of integral equation (2.21), the appropriate dispersion relation can be employed to find the corresponding resonance frequencies. When losses are not neglected, actual permittivities are complex-valued functions of frequency  $\omega$ . These permittivities may assume real resonance values  $\epsilon_+^{(0)}$  only for complex resonance frequencies.

The kernels in integral equations (2.21) is not Hermitian (not self-adjoint), because the kernel of this equation is not symmetric. For this reason, the eigenfunctions  $\sigma_i(M)$  and  $\sigma_k(M)$  corresponding to different eigenvalues  $\lambda_i$  and  $\lambda_k$  are not orthogonal on  $S$  in the usual sense. Nevertheless, it has been shown [20] that electrical fields  $\mathbf{E}_{0i}$  and  $\mathbf{E}_{0k}$  corresponding to eigenfunctions  $\sigma_i(M)$  and  $\sigma_k(M)$  satisfy

the following strong orthogonality conditions:

$$\int_{V^\pm} \mathbf{E}_{0i} \cdot \mathbf{E}_{0k} dV = 0. \quad (2.26)$$

Furthermore, the eigenfunctions  $\sigma_k(M)$  and  $\tau_i(M)$  of adjoint equations (2.21) and (2.23) form two biorthogonal sets

$$\oint_S \sigma_k(M) \tau_i(M) dS = \delta_{ki}. \quad (2.27)$$

This biorthogonal property is very important and can be used for the analysis of time-dynamics of plasmon resonances in nanoparticles [61].

It is instructive to note that the “plasmon” eigenfunctions of integral equation (2.21) have the property:

$$\oint_S \sigma(M) dS_M = 0. \quad (2.28)$$

Indeed, by integrating both sides of equation (2.21) with respect to  $Q$  and by using the facts that:

$$\oint_S \frac{\mathbf{r}_{MQ} \cdot \mathbf{n}_Q}{r_{MQ}^3} dS_M = 2\pi \quad (2.29)$$

and  $\lambda \neq 1$  for plasmon resonances, we arrive at (2.28).

It is apparent that the mathematical structure of integral equation (2.21) is invariant with respect to the scaling of  $S$ , i.e. the scaling of the dimensions of the particle. This leads to the unique property of electrostatic (plasmon) resonances: *resonance frequencies depend on particle shape but they are scale invariant with respect to particle dimensions, provided that they remain appreciably smaller than the free-space wavelength.*

### 2.1.4 First order correction

From formulas (2.4)–(2.9), (2.11)–(2.13) and (2.18), we derive the following boundary value problems for the first-order corrections  $\mathbf{e}_1^\pm, \epsilon_+^{(1)}$  and  $\mathbf{h}_1^\pm$ , respectively:

$$\nabla \times \mathbf{e}_1^\pm = 0, \quad \nabla \cdot \mathbf{e}_1^\pm = 0, \quad (2.30)$$

$$\mathbf{n} \times (\mathbf{e}_1^+ - \mathbf{e}_1^-) = 0, \quad \mathbf{n} \cdot \left( \frac{\epsilon_+^{(0)}}{\epsilon_0} \mathbf{e}_1^+ - \mathbf{e}_1^- \right) = -\frac{\epsilon_+^{(1)}}{\epsilon_0} \mathbf{n} \cdot \mathbf{e}_0^+, \quad (2.31)$$

and

$$\nabla \times \mathbf{h}_1^+ = i \frac{\epsilon_+^{(0)}}{\epsilon_0} \mathbf{e}_0^+, \quad \nabla \times \mathbf{h}_1^- = i \mathbf{e}_0^-, \quad \nabla \cdot \mathbf{h}_1^\pm = 0, \quad (2.32)$$

$$\mathbf{n} \times (\mathbf{h}_1^+ - \mathbf{h}_1^-) = 0, \quad \mathbf{n} \cdot (\mathbf{h}_1^+ - \mathbf{h}_1^-) = 0, \quad (2.33)$$

where as before  $\mathbf{e}_0^\pm = \epsilon_0^{\frac{1}{2}} \mathbf{E}_0^\pm$ .

To solve (2.30)–(2.31), the electric potential  $\varphi_1$  of a single layer of electric charges  $\sigma_1$  distributed over  $S$  can be introduced for the electric field  $\mathbf{e}_1^\pm$ . Then, by using formulas (2.20) and the same reasoning as in the derivation of integral equation (2.21), we arrive at the following integral equation for  $\sigma_1(M)$ :

$$\sigma_1(Q) - \frac{\lambda}{2\pi} \oint_S \sigma_1(M) \frac{\mathbf{r}_{MQ} \cdot \mathbf{n}_Q}{r_{MQ}^3} dS_M = \epsilon_+^{(1)} \frac{2\epsilon_0}{\epsilon_+^{(0)} + \epsilon_0} \mathbf{n}_Q \cdot \mathbf{e}_0^+(Q), \quad (2.34)$$

where  $\lambda$  is given by formula (2.22).

It is clear that  $\lambda$  is one of the eigenvalues of integral equation (2.21), because only for such  $\lambda$  nonzero field  $\mathbf{e}_0$  exists. Since  $\lambda$  in (2.34) is an eigenvalue, a solution to equation (2.34) exists only under the condition that the right-hand side of equation (2.34) is orthogonal on  $S$  to a nonzero solution  $\tau(Q)$  of the corresponding homogeneous adjoint equation (2.23) with the same eigenvalue  $\lambda$  (this is the



so-called “normal solvability condition”). It is clear that  $\mathbf{n}_Q \cdot \mathbf{e}_0^+(Q)$  is proportional to  $\frac{\partial \varphi^+}{\partial n}(Q)$ . By using the well-known properties of double-layer potential [70, 71], it can be shown that  $\tau(Q)$  is proportional to  $\varphi^+(Q)$ . Consequently,

$$\oint_S \tau(Q) \mathbf{n}_Q \cdot \mathbf{e}_0^+ dS_Q = \alpha \oint_S \varphi^+(Q) \frac{\partial \varphi^+}{\partial n}(Q) dS_Q = \alpha \oint_{V^+} |\nabla \varphi^+|^2 dV \neq 0. \quad (2.35)$$

This means that the integral equation (2.34) is only solvable if

$$\epsilon_+^{(1)} = 0. \quad (2.36)$$

Thus, for any shape of nanoparticle the first order correction for resonant values of dielectric permittivity is equal to zero. As a result of (2.36), integral equation (2.34) is reduced to homogeneous integral equation identical to equation (2.21). This implies that up to a scale  $\sigma(M)$  and  $\sigma_1(M)$  as well as  $\mathbf{e}_0^\pm$  and  $\mathbf{e}_1^\pm$  are identical. For this reason, it can be assumed that:

$$\mathbf{e}_1^\pm = 0. \quad (2.37)$$

Next, we proceed to the solution of boundary value problem (2.32)–(2.33). Terms  $i\frac{\epsilon_+^{(0)}}{\epsilon_0}\mathbf{e}_0^+$  and  $i\mathbf{e}_0^-$  in the first two equations (2.32) can be interpreted as current sources and the solution of boundary value problem (2.32)–(2.33) can be written in the following integral form:

$$\mathbf{h}_1(Q) = \frac{i\epsilon_+^{(0)}}{4\pi\epsilon_0} \int_{V^+} \frac{\mathbf{e}_0^+(M) \times \mathbf{r}_{MQ}}{r_{MQ}^3} dV_M + \frac{i}{4\pi} \int_{V^-} \frac{\mathbf{e}_0^-(M) \times \mathbf{r}_{MQ}}{r_{MQ}^3} dV_M. \quad (2.38)$$

The last expression can be appreciably simplified and reduced to an integral over the boundary  $S$ . Indeed, by using the fact that  $\nabla \times \mathbf{e}_0^\pm = 0$  and by employing the “curl-theorem” [87], after simple transformations we arrive at:

$$\mathbf{h}_1(Q) = -\frac{i\left(\frac{\epsilon_+^{(0)}}{\epsilon_0} - 1\right)}{4\pi} \oint_S \frac{\mathbf{n}_M \times \mathbf{e}_0(M)}{r_{MQ}} dS_M. \quad (2.39)$$

### 2.1.5 Second order correction

In this section, we proceed to the discussion of second order corrections for  $\epsilon_+(\omega)$ . From formulas (2.4)–(2.9), (2.11)–(2.13) and (2.36)–(2.37) we derive the following boundary value problems for the second-order corrections of  $\mathbf{e}_2^\pm$ ,  $\epsilon_+^{(2)}$  and  $\mathbf{h}_2^\pm$ , respectively:

$$\nabla \times \mathbf{e}_2^\pm = -i\mathbf{h}_1^\pm, \quad \nabla \cdot \mathbf{e}_2^\pm = 0, \quad (2.40)$$

$$\mathbf{n} \times (\mathbf{e}_2^+ - \mathbf{e}_2^-) = 0, \quad \mathbf{n} \cdot \left( \frac{\epsilon_+^{(0)}}{\epsilon_0} \mathbf{e}_2^+ - \mathbf{e}_2^- \right) = -\frac{\epsilon_+^{(2)}}{\epsilon_0} \mathbf{n} \cdot \mathbf{e}_0^+, \quad (2.41)$$

and

$$\nabla \times \mathbf{h}_2^\pm = 0, \quad \nabla \cdot \mathbf{h}_2^\pm = 0, \quad (2.42)$$

$$\mathbf{n} \times (\mathbf{h}_2^+ - \mathbf{h}_2^-) = 0, \quad \mathbf{n} \cdot (\mathbf{h}_2^+ - \mathbf{h}_2^-) = 0, \quad (2.43)$$

It is apparent from (2.42)–(2.43) that

$$\mathbf{h}_2^\pm = 0. \quad (2.44)$$

To solve (2.40)–(2.41), we shall first decompose the electric field  $\mathbf{e}_2^\pm$  into two distinct components:

$$\mathbf{e}_2^\pm = \tilde{\mathbf{e}}_2^\pm + \tilde{\tilde{\mathbf{e}}}_2^\pm, \quad (2.45)$$

which satisfy the following boundary value problems, respectively:

$$\nabla \times \tilde{\mathbf{e}}_2 = -i\mathbf{h}_1, \quad \nabla \cdot \tilde{\mathbf{e}}_2 = 0, \quad (2.46)$$

$$\mathbf{n} \times (\tilde{\mathbf{e}}_2^+ - \tilde{\mathbf{e}}_2^-) = 0, \quad \mathbf{n} \cdot (\tilde{\mathbf{e}}_2^+ - \tilde{\mathbf{e}}_2^-) = 0, \quad (2.47)$$

and

$$\nabla \times \tilde{\tilde{\mathbf{e}}}_2^\pm = 0, \quad \nabla \cdot \tilde{\tilde{\mathbf{e}}}_2^\pm = 0, \quad (2.48)$$

$$\begin{aligned}\mathbf{n} \times (\tilde{\mathbf{e}}_2^+ - \tilde{\mathbf{e}}_2^-) &= 0, \\ \mathbf{n} \cdot \left( \frac{\epsilon_+^{(0)}}{\epsilon_0} \tilde{\mathbf{e}}_2^+ - \tilde{\mathbf{e}}_2^- \right) &= -\mathbf{n} \cdot \left[ \frac{\epsilon_+^{(2)}}{\epsilon_0} \mathbf{e}_0^+ + \left( \frac{\epsilon_+^{(0)}}{\epsilon_0} - 1 \right) \tilde{\mathbf{e}}_2^+ \right].\end{aligned}\quad (2.49)$$

The solution of the boundary value problem (2.46)–(2.47) is:

$$\tilde{\mathbf{e}}_2(P) = -\frac{i}{4\pi} \int_{R^3} \frac{\mathbf{h}_1(Q) \times \mathbf{r}_{QP}}{r_{QP}^3} dV_Q. \quad (2.50)$$

By substituting the expression (2.39) into the last formula and by changing the order of integration, we arrive at:

$$\tilde{\mathbf{e}}_2(P) = -\frac{\left( \frac{\epsilon_+^{(0)}}{\epsilon_0} - 1 \right)}{16\pi^2} \oint_S (\mathbf{n}_M \times \mathbf{e}_0(M)) \times \left( \int_{R^3} \frac{\mathbf{r}_{QP}}{r_{QP}^3} \frac{1}{r_{QM}} dV_Q \right) dS_M. \quad (2.51)$$

The last expression can be simplified to [20]:

$$\tilde{\mathbf{e}}_2(P) = -\frac{\left( \frac{\epsilon_+^{(0)}}{\epsilon_0} - 1 \right)}{8\pi} \oint_S \frac{(\mathbf{n}_M \times \mathbf{e}_0(M)) \times \mathbf{r}_{MP}}{r_{MP}} dS_M. \quad (2.52)$$

Next, we proceed to the solution of the boundary value problem (2.48)–(2.49). It is apparent that the electric potential  $\varphi_2$  of single layer of electric charges  $\sigma_2(M)$  distributed over  $S$  can be introduced for the electric field  $\tilde{\mathbf{e}}_2^\pm$ . Then, by using formula (2.20) and the same line of reasoning as in the derivation of integral equation (2.21), we obtain the following integral equation for  $\sigma_2(M)$ :

$$\sigma_2(Q) - \frac{\lambda}{2\pi} \oint_S \sigma_2(M) \frac{\mathbf{r}_{MQ} \cdot \mathbf{n}_Q}{r_{MQ}^3} dS_M = \frac{2\epsilon_0^2}{\epsilon_0 - \epsilon_+^{(0)}} \mathbf{n} \cdot \left[ \frac{\epsilon_+^{(2)}}{\epsilon_0} \mathbf{e}_0^+ + \left( \frac{\epsilon_+^{(0)}}{\epsilon_0} - 1 \right) \tilde{\mathbf{e}}_2^+ \right], \quad (2.53)$$

where as before  $\lambda$  is given by formula (2.22) and is one of the eigenvalues of integral equation (2.21). Since  $\lambda$  is an eigenvalue, a solution to equation (2.53) exists (according to the Fredholm Theorem) only under the condition that the right-hand side of the equation (2.53) is orthogonal on  $S$  to a nonzero solution  $\tau(Q)$  of the

corresponding homogeneous adjoint equation (2.23). This normal solvability condition leads to the following expression for the second order correction of resonant permittivity  $\epsilon_+^{(2)}$ :

$$\epsilon_+^{(2)} = \frac{\epsilon_0 \left( \frac{\epsilon_+^{(0)}}{\epsilon_0} - 1 \right) \oint_S \tau(Q) \mathbf{n}_Q \cdot \tilde{\mathbf{e}}_2^+(Q) dS_Q}{\oint_S \tau(Q) \mathbf{n}_Q \cdot \mathbf{e}_0^+(Q) dS_Q}. \quad (2.54)$$

Thus, the algorithm for computations of the second order correction  $\epsilon_+^{(2)}$  can be stated as follows: first, integral equations (2.21) and (2.23) are solved and for each eigenvalue the corresponding  $\epsilon_+^{(0)}$  and eigenfunction  $\sigma(M)$  and  $\tau(M)$  are found; then, by using formula (2.52),  $\tilde{\mathbf{e}}_2^+$  is computed on  $S$ ; finally, by employing expression (2.54), the second-order corrections  $\epsilon_+^{(2)}$  to resonant permittivities  $\epsilon_+^{(0)}$  can be calculated. According to (2.13), the resonant permittivities are given by the formula:

$$\epsilon_+ = \epsilon_+^{(0)} + \beta^2 \epsilon_+^{(2)}, \quad (2.55)$$

where  $\beta$  is defined in (2.10).

## 2.2 Comparison with the Mie theory for sphere

The perturbation formulations have been derived in section 2.1 for the calculation of the values of dielectric permittivity  $\epsilon_+$  for specific plasmon modes. To test its validity, let us first compare with the Mie theory, which provides analytical solutions for spherical nanoparticles. Indeed, according to the Mie theory, the resonance values of dielectric permittivity (up to the second order corrections) for the first three degenerate plasmon modes (spatially uniform modes) is [39]:

$$\epsilon_+ = - \left( 2 + \frac{3}{5} \beta^2 \right) \epsilon_0 = - \left( 2 + \frac{12}{5} \omega^2 \mu_0 \epsilon_0 a^2 \right) \epsilon_0. \quad (2.56)$$

In the following, we demonstrate that the perturbation formulations derived in section 2.1 lead to the same conclusion.

### 2.2.1 Zero order solution

We first consider the zero order solution. The boundary value problem (2.14)-(2.15) subject to a sphere (with radius  $r$ ) can be rewritten in terms of the scalar potential  $\varphi$  as follows:

$$\nabla^2 \varphi^\pm = 0, \quad (2.57)$$

$$\varphi^+ = \varphi^-, \quad (2.58)$$

$$\epsilon_+^{(0)} \frac{\partial \varphi^+}{\partial n} = \epsilon_0 \frac{\partial \varphi^-}{\partial n}, \quad (2.59)$$

and this potential satisfies the Sommerfeld radiation condition

$$\lim_{r \rightarrow \infty} \sqrt{r} \left( \frac{\partial \varphi}{\partial r} - ik\varphi \right) = 0. \quad (2.60)$$

In this case, we are interested in such values of  $\epsilon_+^{(0)}$  that the sourceless fields may exist for the above boundary value problem. The general solutions of (2.55) for regions  $V^+$  and  $V^-$  are:

$$\varphi^+(r, \theta, \phi) = \sum_{l,m} A_{lm} r^l Y_{lm}(\theta, \phi), \quad (2.61)$$

$$\varphi^-(r, \theta, \phi) = \sum_{l,m} B_{lm} r^{-l-1} Y_{lm}(\theta, \phi), \quad (2.62)$$

where  $Y_{lm}(\theta, \phi)$  are spherical harmonics, and  $A_{lm}$  and  $B_{lm}$  are unknown coefficients. Substituting (2.61)-(2.62) into boundary conditions (2.58)-(2.59), and by using orthogonality properties of spherical harmonics, we conclude that:

$$A_{lm} = B_{lm}, \quad (2.63)$$

$$\epsilon_+^{(0)} l = -\epsilon_0 (l + 1). \quad (2.64)$$

Therefore,

$$\epsilon_+^{(0)} = -\frac{l+1}{l} \epsilon_0. \quad (2.65)$$

It is clear that when  $l = 1$ , the solutions of Laplace's equation are three-fold degenerate ( $m = 0, \pm 1$ ) and the associated electric fields are spatially uniform inside the sphere. These modes are the fundamental plasmon modes in spherical nanoparticles and the corresponding resonance value of dielectric permittivity for these modes is  $\epsilon_+^{(0)} = -2\epsilon_0$ . The frequency at which the dispersion relation assumes this value is known as the Fröhlich frequency. To make the zero order solution complete, it is necessary to know the scalar potential, surface charge density and electrical fields. Since the three modes are degenerate and the only difference is spatial orientation, in the following analysis, only the mode which has electric field along the z-axis is considered. It is easy to show that (assuming  $A_{10} = 1$ ):

$$\varphi^+(r, \theta, \phi) = \sqrt{\frac{3}{4\pi}} \cos \theta, \quad (2.66)$$

$$\varphi^-(r, \theta, \phi) = \sqrt{\frac{3}{4\pi}} \cos \theta, \quad (2.67)$$

$$\sigma_0 = \frac{\partial \varphi^+}{\partial n} - \frac{\partial \varphi^-}{\partial n} = 3\sqrt{\frac{3}{4\pi}} \cos \theta, \quad (2.68)$$

$$\mathbf{e}_{01}^+(r, \theta, \phi) = -\mathbf{a}_r \sqrt{\frac{3}{4\pi}} \cos \theta - \mathbf{a}_\theta \sqrt{\frac{3}{4\pi}} \sin \theta. \quad (2.69)$$

In Cartesian coordinates, the electrical field for this mode can be expressed below and it is clear that the electric field is uniform.

$$\mathbf{e}_{01x}^+(x, y, z) = -\sqrt{\frac{3}{4\pi}} \mathbf{a}_x (\sin \theta \cos \phi \cos \theta - \cos \theta \cos \phi \sin \theta) = 0, \quad (2.70)$$

$$\mathbf{e}_{01y}^+(x, y, z) = -\sqrt{\frac{3}{4\pi}} \mathbf{a}_y (\sin \theta \sin \phi \cos \theta - \cos \theta \sin \phi \sin \theta) = 0, \quad (2.71)$$

$$\mathbf{e}_{01z}^+(x, y, z) = -\sqrt{\frac{3}{4\pi}} \mathbf{a}_z (\cos \theta \cos \theta + \sin \theta \sin \theta) = -\sqrt{\frac{3}{4\pi}} \mathbf{a}_z. \quad (2.72)$$

## 2.2.2 Second order solution

Since  $\epsilon_+^{(0)} = 2\epsilon_0$ , the formula (2.54) for the second order correction of resonance values of dielectric permittivity becomes:

$$\epsilon_+^{(2)} = -3 \frac{\oint_S \mathbf{n}_M \cdot \tilde{\mathbf{e}}_2^+(M) \tau_0^+(M) dS_M}{\oint_S \mathbf{n}_M \cdot \mathbf{e}_0^+(M) \tau_0^+(M) dS_M}. \quad (2.73)$$

Although the surface dipole density  $\tau_0^+$  is not explicitly computed in the zero order solution, due to the fact that the resulting electric fields are uniform for the mode under consideration,  $\tau_0^+$  is proportional to  $\sigma_0^+$  up to a constant. Therefore,  $\sigma_0^+$  can be used in the evaluation of the integrals in above formula. We first calculate the denominator of formula (2.73):

$$I_d = \oint_S \mathbf{n}_M \cdot \mathbf{e}_0^+(M) \sigma_0^+(M) dS_M. \quad (2.74)$$

Substituting (2.68) and (2.69) into (2.74), after simple algebra, the analytical result is obtained:

$$I_d = -\frac{9}{4\pi} \int_0^{2\pi} d\phi \int_0^\pi \cos^2 \theta r^2 \sin \theta d\theta = -3. \quad (2.75)$$

Then formula (2.73) becomes:

$$\epsilon_+^{(2)} = \oint_S \mathbf{n}_M \cdot \tilde{\mathbf{e}}_2^+(M) \tau_0^+(M) dS_M. \quad (2.76)$$

Let's denote this integral as  $I_n$ . The evaluation of integral  $I_n$  is somewhat lengthy, nevertheless the main steps are specified as follows. First, we need to express  $\tilde{\mathbf{e}}_2^+$  in

terms of  $\mathbf{e}_0^+$ . According to equation (2.50) and (2.69), it can be shown that:

$$\tilde{\mathbf{e}}_2^+(M) = \alpha \oint_S \hat{\mathbf{r}}_{QM} \times \mathbf{a}_{\phi Q} \sin \theta dS_Q, \quad (2.77)$$

where:

$$\alpha = \frac{\left(\frac{\epsilon_0^+}{\epsilon_0} - 1\right)}{8\pi} \sqrt{\frac{3}{4\pi}} = -\frac{3}{8\pi} \sqrt{\frac{3}{4\pi}}. \quad (2.78)$$

According to equation (2.77), formula (2.74) can be expressed as:

$$I_n = \alpha \oint_S \mathbf{a}_{rM} \cdot \left\{ \oint_S \frac{\mathbf{r}_Q - \mathbf{r}_M}{r_{MQ}} \times (\mathbf{a}_{\phi Q} \sin \theta_Q) dS_Q \right\} \sigma_0^+(M) dS_M. \quad (2.79)$$

Note for the unit sphere that

$$\mathbf{r}_M = \mathbf{a}_{rM} = \mathbf{n}_M, \quad \mathbf{r}_Q = \mathbf{a}_{rQ} = \mathbf{n}_Q, \quad (2.80)$$

which imply that formula (2.79) can be reduced to:

$$I_n = -\alpha \oint_S \mathbf{a}_{\theta Q} \sin \theta_Q \cdot \left\{ \oint_S \frac{\mathbf{a}_{rM}}{r_{MQ}} \sigma_0^+(M) dS_M \right\} dS_Q. \quad (2.81)$$

The integral inside the bracket of (2.81) is a vector, the three components can be analytically evaluated and the results are:

$$I_x = k_1 \cos \theta_Q \sin \theta_Q \cos \phi_Q, \quad (2.82)$$

$$I_y = k_1 \cos \theta_Q \sin \theta_Q \sin \phi_Q, \quad (2.83)$$

$$I_z = k_1 \left( \cos^2 \theta_Q + \frac{4}{3} \right), \quad (2.84)$$

where

$$k_1 = \frac{6}{5} \sqrt{3\pi}. \quad (2.85)$$

Substituting (2.82)-(2.84) into (2.81), we get:

$$I_n = -\alpha k_1 \oint_S \left[ \cos^2 \theta_Q \sin^2 \theta_Q - \sin^2 \theta_Q \left( \cos^2 \theta_Q + \frac{4}{3} \right) \right] dS_Q. \quad (2.86)$$



The rest of the work is straightforward, with some caution in the evaluation, we obtain:

$$\epsilon_+^{(2)} = I_n = -\frac{3}{5}. \quad (2.87)$$

Then the resonance values of dielectric permittivity for spherical nanoparticles up to second order corrections are found as

$$\epsilon_+ = \epsilon_+^{(0)} + \beta^2 \epsilon_+^{(2)} = -\left(2 + \frac{3}{5}\beta^2\right) \epsilon_0. \quad (2.88)$$

This formula is identical to the analytical expression given by Mie theory (see formula (2.54)). In conclusion, as far as the spherical nanoparticle is concerned, our integral equation technique agrees with the classical Mie theory.

## 2.3 Numerical analysis of plasmon resonances in nanoparticles

### 2.3.1 Numerical technique for solution of integral equation

From the discussion in Section 2.1, it is clear that the key step of numerical analysis of plasmon resonances in nanoparticles is to solve integral equation (2.21). Now we proceed to the discussion of an efficient numerical technique for the solutions of this integral equation. To this end, let us partition  $S$  into  $N$  small pieces  $\Delta S_j$  and rewrite integral equation (2.21) as follows:

$$\sigma(Q) = \frac{\lambda}{2\pi} \sum_{j=1}^N \int_{\Delta S_j} \sigma(M) \frac{\mathbf{r}_{MQ} \cdot \mathbf{n}_Q}{r_{MQ}^3} dS_M. \quad (2.89)$$

Now, we integrate (2.89) over  $\Delta S_i$ :

$$\int_{\Delta S_i} \sigma(Q) dS_Q = \frac{\lambda}{2\pi} \sum_{j=1}^N \int_{\Delta S_j} \sigma(M) \left[ \int_{\Delta S_i} \frac{\mathbf{r}_{MQ} \cdot \mathbf{n}_Q}{r_{MQ}^3} dS_Q \right] dS_M, \quad (i = 1, 2, \dots, N). \quad (2.90)$$

By introducing the notation

$$\omega_i(M) = \int_{\Delta S_i} \frac{\mathbf{r}_{MQ} \cdot \mathbf{n}_Q}{r_{MQ}^3} dS_Q, \quad (2.91)$$

the last formula can be presented as follows:

$$\int_{\Delta S_i} \sigma(Q) dS_Q = \frac{\lambda}{2\pi} \sum_{j=1}^N \int_{\Delta S_j} \sigma(M) \omega_i(M) dS_M. \quad (2.92)$$

It is apparent that  $\omega_i(M)$  is the solid angle which  $\Delta S_i$  subtends at point  $M$ . By introducing new variables

$$X_i = \int_{\Delta S_i} \sigma(Q) dS_Q, \quad (2.93)$$

integrals in the right-hand side of (2.92) can be approximated as follows:

$$\int_{\Delta S_j} \sigma(M) \omega_i(M) dS_M \approx \omega_i(M_j) X_j = \omega_{ij} X_j, \quad (2.94)$$

where  $M_j$  is some middle point of partition  $\Delta S_j$ . It is apparent (on intuitive grounds) that approximation (2.94) is more accurate than direct discretization of integral in (2.21), because solid angles  $\omega_i(M)$  are smooth functions of  $M$ , while the kernel of integral equation (2.21) is (weakly) singular. By substituting formulas (2.93) and (2.94) into equation (2.92), we obtain:

$$X_i = \frac{\lambda}{2\pi} \sum_{j=1}^N \omega_{ij} X_j. \quad (2.95)$$

Another advantage of discretization (2.95) is that the evaluation of singular integrals in calculations of  $\omega_{ii}$  can be completely avoided. Indeed, according to formulas (2.29) and (2.91), we find:

$$\omega_{ii} \approx 2\pi - \sum_{i=1, i \neq j}^N \omega_{ij}. \quad (2.96)$$

The numerical technique based on discretization (2.95) has been software implemented and extensively tested by the author. It has proved to be remarkably accurate, even for calculation of large eigenvalues.

### 2.3.2 Numerical results

The algorithm described above has been first tested for spherical nanoparticles where exact analytical solutions are available (Mie theory[39]). The results of numerical computations are presented in Table 2.1. It is apparent from this table that numerical results are quite accurate even for appreciably high mode orders. The surface charge distribution (eigenfunction) for the first 10 eigenmodes are plotted in Figure 2.5. Next, the described algorithm has been tested for ellipsoidal nanoparticles. The computational results are presented in Table 2.2 for the case of ellipsoid of revolution with the main axis ratios 1:1:1.55. It is evident from this Table that the computed eigenvalues compare quite well with the exact (theoretical) eigenvalues  $\lambda_i = \frac{1}{1-2N_i}$  for spatially uniform modes. It is also apparent that for those modes  $\sum_i \frac{1}{\lambda_i}$  is very close to 1 as it must be. The surface charge distribution (eigenfunction) for the first 10 eigenmodes are plotted in Figure 2.6

Fig. 2.8 presents the computational results for the resonant free-space wavelength as a function of separation distance between two gold spherical nanoparticles located on a dielectric substrate with  $\epsilon = 2.25\epsilon_0$  for different values of radius ratio (see Fig. 2.7). It is clear from Fig. 2.8 that the separation between two spheres can be effectively used for tuning of plasmon resonances to desirable frequencies.

Fig. 2.8 is an example of our numerous computations performed for two and several nanospheres of various radii and separation distances. We have computed the resonance wavelength for two short gold cylinders of ellipsoidal cross-sections placed on a dielectric substrate (see Fig. 2.9). Fig. 2.10 presents the computational results for the resonance wavelength as the function of separation between cylinders for different values of the axis ratio.

Table 2.3 presents the computational results for gold nano-rings placed on a dielectric substrate. In this table, the computational results for resonance wavelengths are compared with those found experimentally (see reference [72]). We have also compared our numerical results with available experimental data for the following two cases: a) a short gold cylinder of ellipsoidal cross-section (with long axis 130nm, short axis 84nm, height 30nm) placed on a dielectric substrate and b) a gold triangular nano-prism (with edge length 48nm, height 14nm). Table 2.4 presents the comparison between our computational results and experimental data published in references [42, 73], respectively. The electrical field intensity of the first two plasmon resonance modes for gold triangle prism is shown in Fig.2.11.

Figure 2.12 presents the comparison of computational and experimental results [74] for the gold nanocube. For the case of the nanocube in water (Fig. 2.12(A)), the two resonance peaks are observed in experiments at 432nm and 500nm, while our computational results reveal resonances at 420nm and 478nm, respectively. For the case of the nanocube on substrate ( $\epsilon = 2.25\epsilon_0$ ) (Fig. 2.12(B)), experiments result in the two resonance peaks at 395nm and 457nm, while our computations suggest resonances at 410nm and 443nm, respectively.

In all these computations, the experimentally measured dispersion relation for gold [68] has been used. The meshes used in calculations are shown in Figure 2.13. It is thus demonstrated that our computational results compare quite well with known theoretical results and are in a reasonably good agreement with the available experimental data.

Table 2.1: Eigenvalues for a single nanosphere.

Mode number	Computed eigenvalues	Mie theory	Mode number	Computed eigenvalues	Mie theory
1	2.999191	3	21	9.038890	9
2	2.999193	3	22	9.049236	9
3	2.999194	3	23	9.049301	9
4	4.980130	5	24	9.049312	9
5	4.980130	5	25	10.86267	11
6	4.980148	5	26	10.86268	11
7	5.022817	5	27	10.86291	11
8	5.022828	5	28	10.94108	11
9	6.927911	7	29	10.94200	11
10	6.981790	7	30	11.03838	11
11	6.981884	7	31	11.03839	11
12	6.981885	7	32	11.03846	11
13	7.027287	7	33	11.06465	11
14	7.027289	7	34	11.06497	11
15	7.027393	7	35	11.06500	11
16	8.915480	9	36	12.75603	13
17	8.915606	9	37	12.84736	13
18	8.915633	9	38	12.84819	13
19	8.979679	9	39	12.84824	13
20	8.979774	9	40	12.93150	13

Table 2.2: Eigenvalues for a single nanoellipsoid with aspect ratio 1:1:1.55.

Mode number	Computed eigenvalues	Theoretical values	Mode number	Computed eigenvalues
1	1.976541	1.9723	6	4.590262
2	3.335450		7	4.829570
3	4.080630	4.0507	8	5.645674
4	4.080692	4.0570	9	5.645746
5	4.590155		10	6.314742

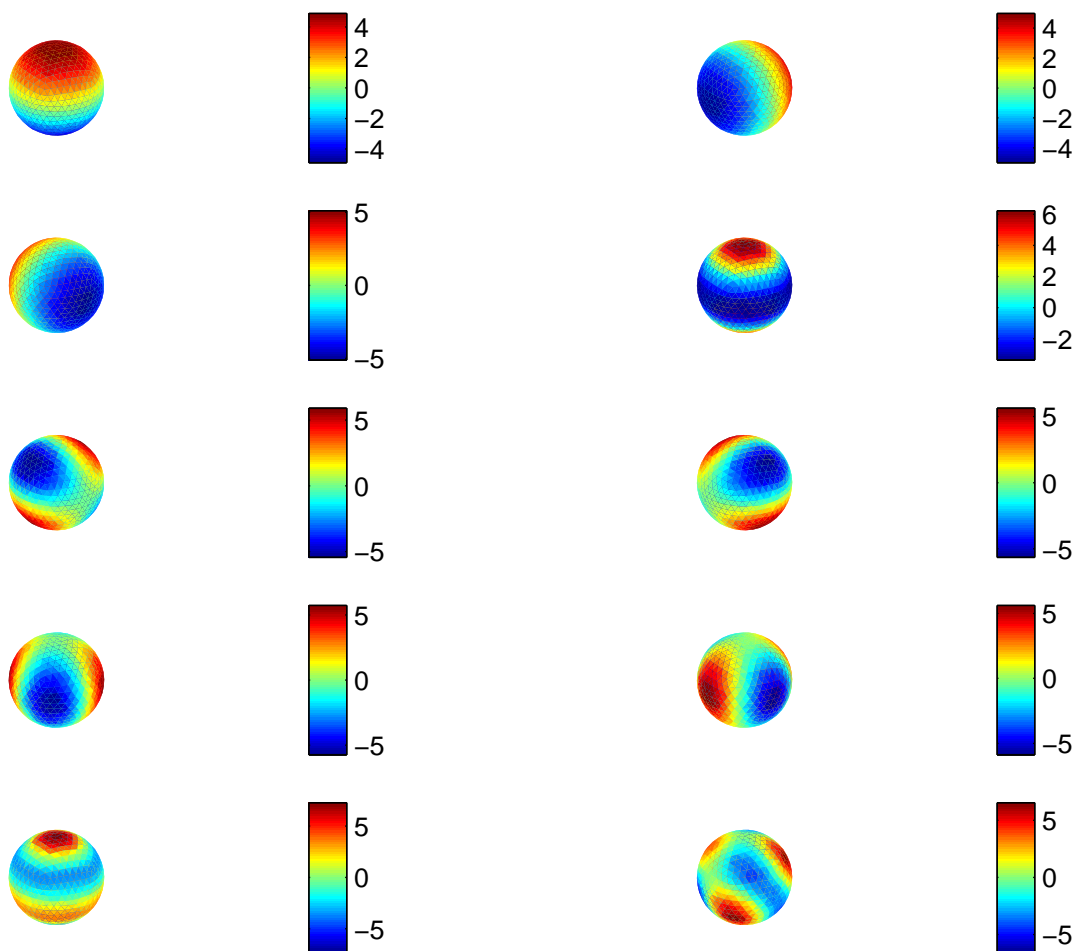


Figure 2.5: Surface charge distribution (eigenfunction) for the first 10 eigenmodes of single nanosphere.

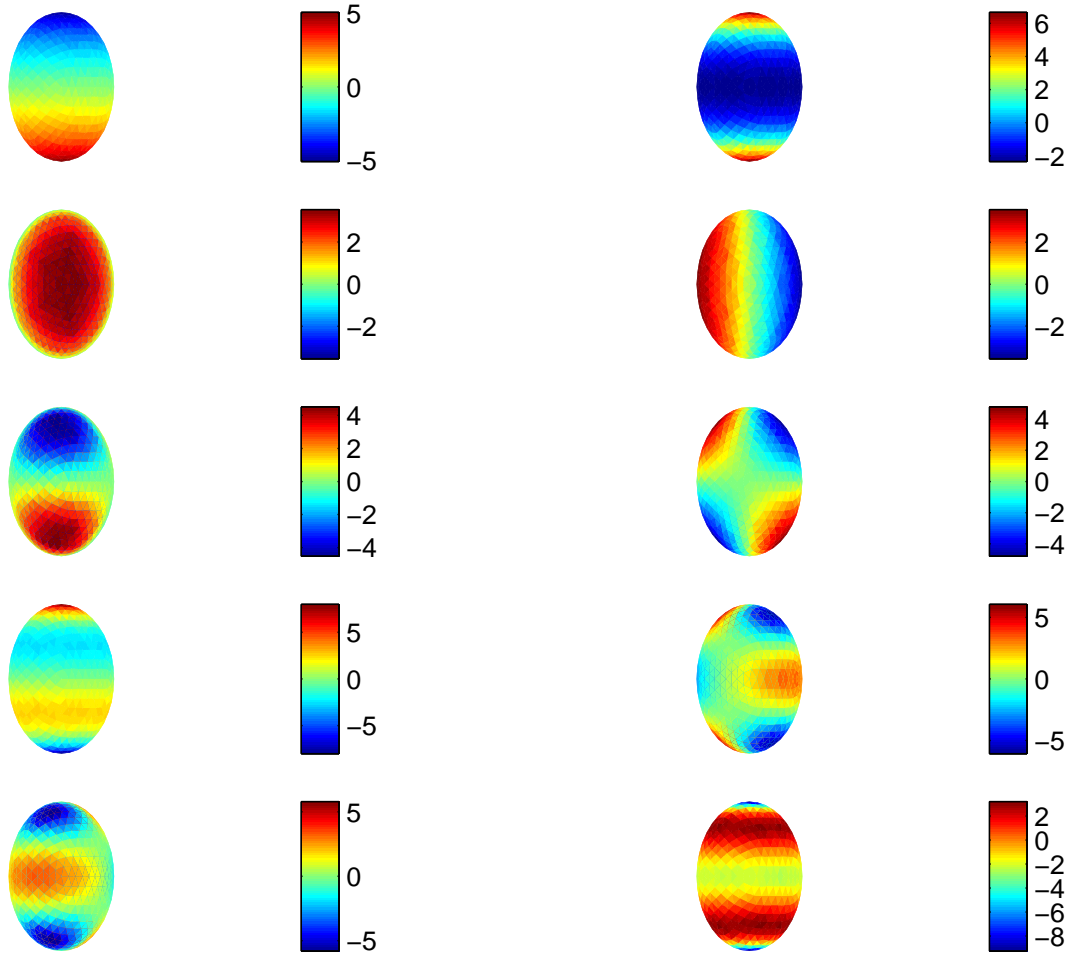


Figure 2.6: Surface charge distribution (eigenfunction) for the first 10 eigenmodes of single nano-ellipsoidal.

Table 2.3: Comparison with experimental results [72] for gold nanoring.

	Ring1	Ring2	Ring3
Outer radius of the ring (nm)	60	60	60
Height of the ring (nm)	40	40	40
Thickness of ring wall (nm)	14(2)	10(2)	9(2)
Experimental resonance (nm)	1000	1180	1350
Computational resonance (nm)	940	1102	1214

Table 2.4: Comparison with experimental results [42, 73] for gold ellipsoidal cylinder and triangular prism.

Resonance	cylinder	prism
wavelength	(nm)	(nm)
Computational results	622	653
Experimental results	645	690



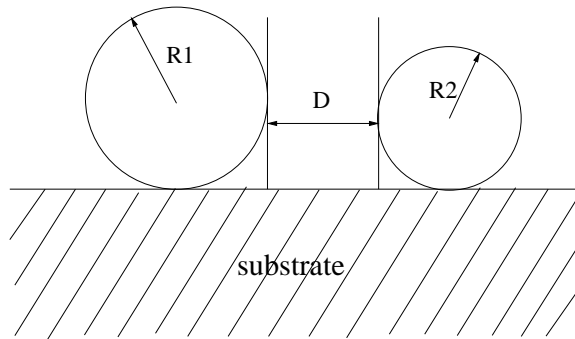


Figure 2.7: Two nanospheres on substrate.

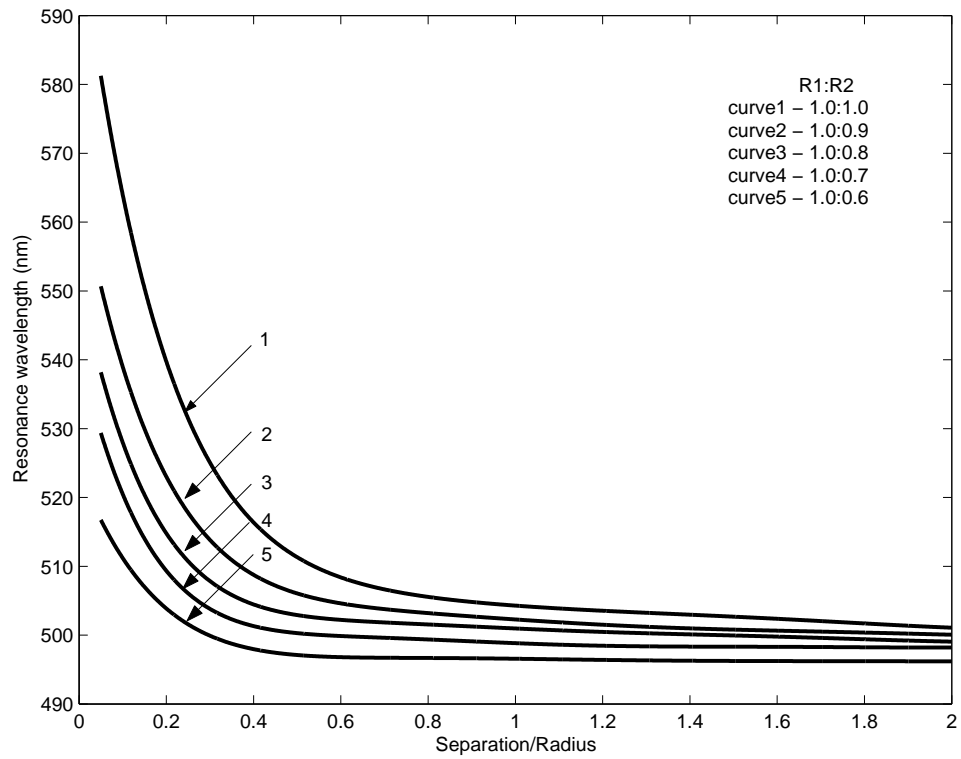


Figure 2.8: Resonance wavelength for two nanospheres on substrate.

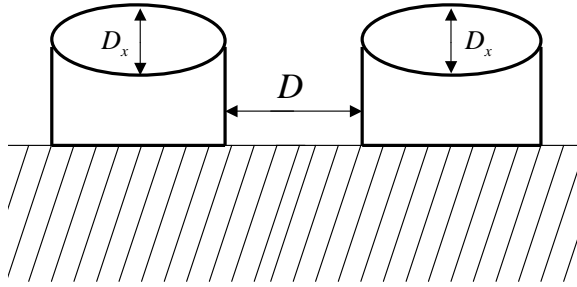


Figure 2.9: Two ellipsoidal cylinders on substrate.

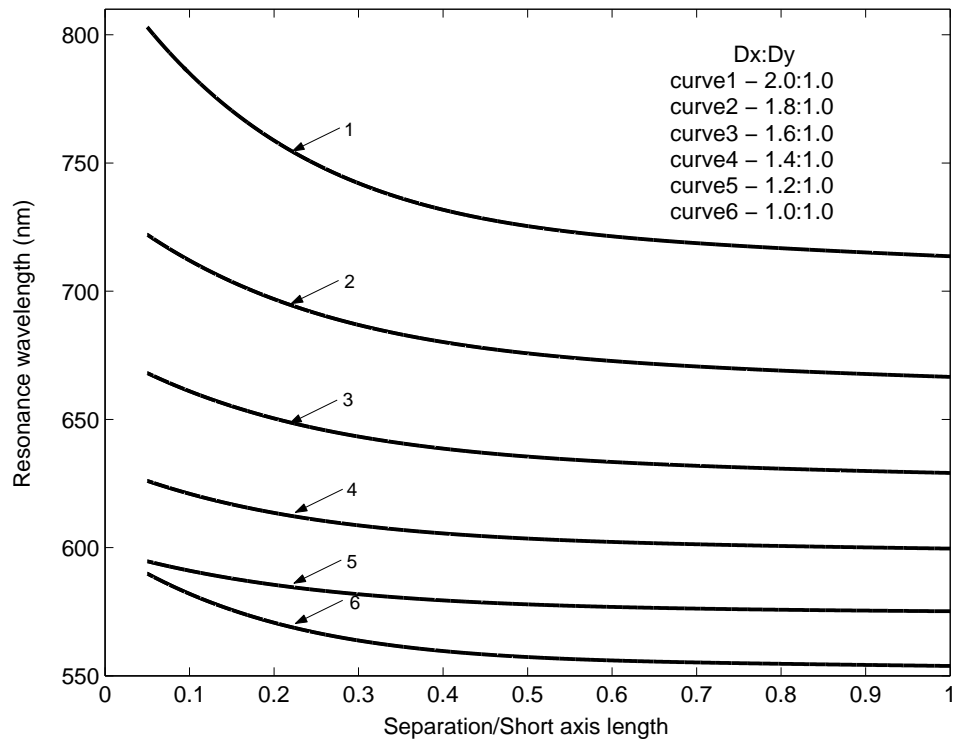


Figure 2.10: Resonance wavelength for two ellipsoidal cylinders on substrate.

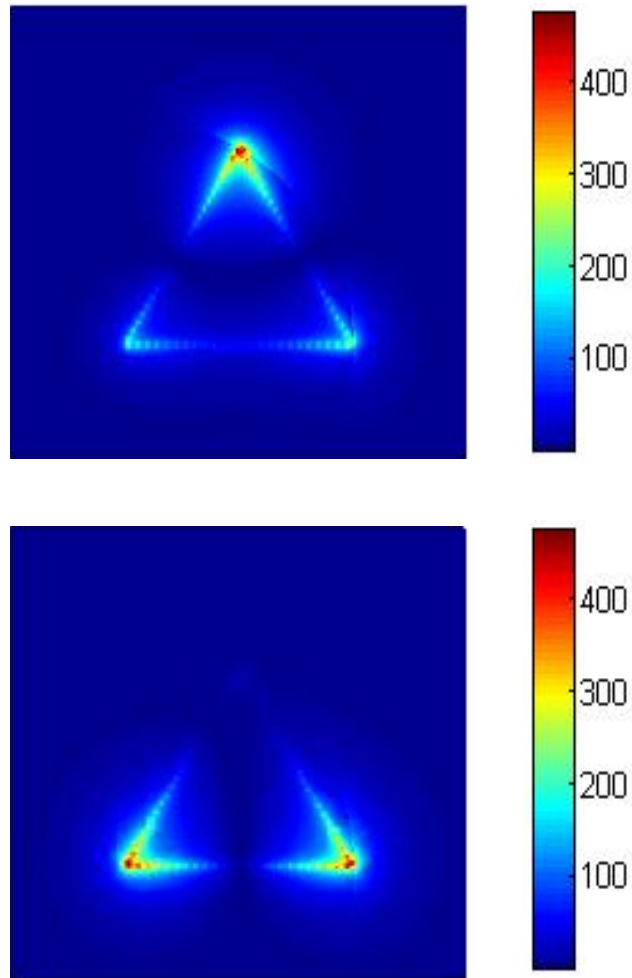


Figure 2.11: The plasmon mode light intensity of first two resonance modes for triangular nanoprism, colorbars indicate the ratio of optical near field intensity normalized to incident fields.

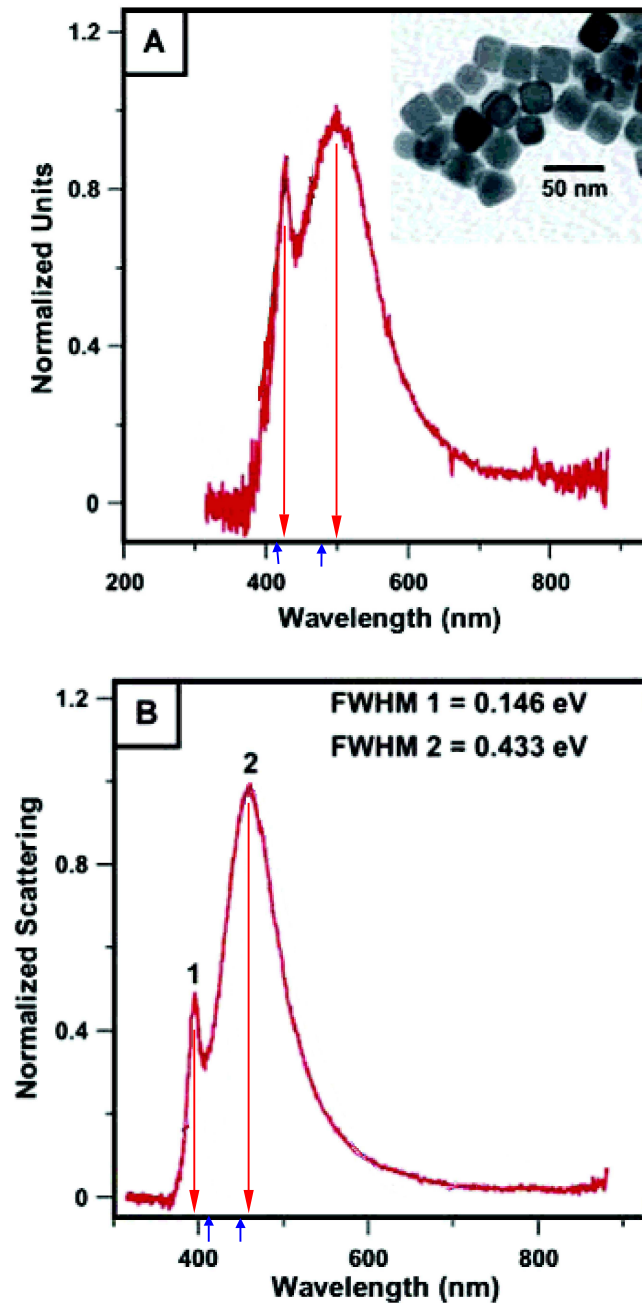
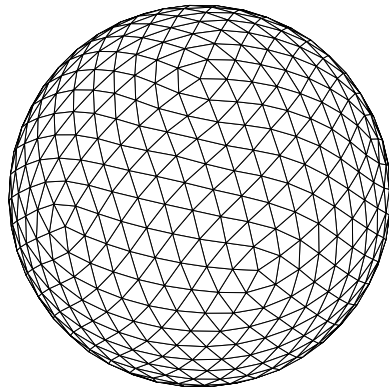
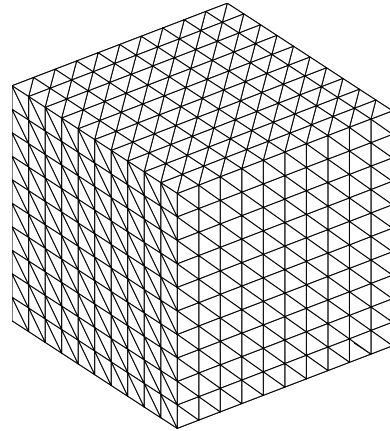


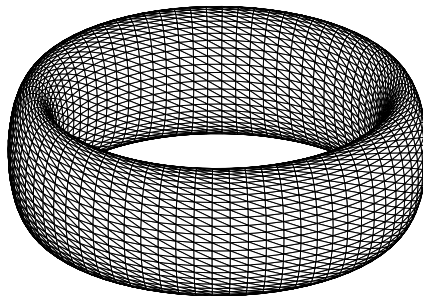
Figure 2.12: Comparison of the plasmon resonance wavelength of (A) nanocube ensemble in water and (B) single nanocube on a glass substrate. The down arrows indicate the experimental results (432 nm and 452 nm in (A), 395 nm and 457 nm for (B)) while the up arrows show the computational results (420 nm and 478 nm in (A), 410 nm and 443 nm in (B)).



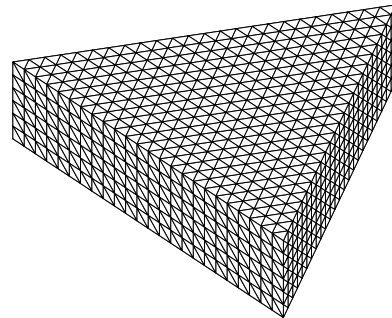
(a) sphere



(b) cube



(c) ring



(d) triprism

Figure 2.13: Examples of surface mesh used in computations for different geometry of three dimensional nanoparticles.

## 2.4 Plasmon resonances in shell structures

The tunability of plasmon resonant frequencies in nanoparticles is important for many applications such as nanophotonics and biosensors. In section 2.3, we have seen that the plasmon resonant frequencies can be tuned by using a two-sphere system and adjusting the coupling between the two particles. The tunable frequency range of this configuration is limited, however, and it usually experiences more losses than single nanoparticle. The wide range tunability of plasmon resonant frequencies of single nanoparticle is clearly desired. It has been observed [27, 28] that this feature can be achieved by using metallic nanoshells and controlling the resonances frequencies via the shell thickness. In this section, the boundary integral equation technique for direct calculations of resonance frequencies of metallic nanoshells is presented. This technique is a modification of the method developed in previous sections for solid nanoparticles. The wide range tunability of plasmon resonant frequencies is illustrated by numerical examples. In addition, analytical studies are performed for spherical and ellipsoidal shells, and a phenomenon of twin spectrum is discussed.

### 2.4.1 A generalized eigenvalue problem

To start the discussion, consider a metallic nanoshell with dielectric core shown in Figure 2.14(a). The plasmon resonances in metallic nanoshell structures can be formulated as the following boundary value problem: find such values of  $\epsilon_+$  for which

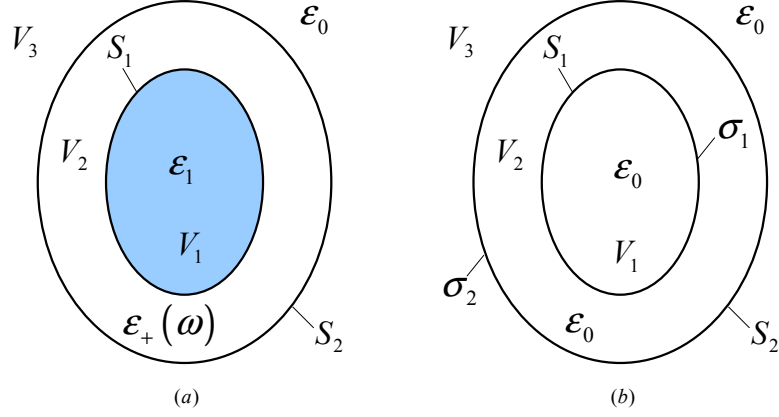


Figure 2.14: (a) Schematic of a nanoshell with dielectric core; (b) the equivalent problem for plasmon resonance in nanoshells.

there exist non-zero solutions to the differential equations:

$$\nabla^2 \varphi_1 = 0 \quad \text{in } V_1, \quad (2.97)$$

$$\nabla^2 \varphi_2 = 0 \quad \text{in } V_2, \quad (2.98)$$

$$\nabla^2 \varphi_3 = 0 \quad \text{in } V_3, \quad (2.99)$$

subject to the boundary conditions:

$$\epsilon_1 \frac{\partial \varphi_1^+}{\partial n} = \epsilon_+ \frac{\partial \varphi_2^+}{\partial n}, \quad \varphi^+ = \varphi^-, \quad \text{on } S_1, \quad (2.100)$$

$$\epsilon_+ \frac{\partial \varphi_2^+}{\partial n} = \epsilon_0 \frac{\partial \varphi_3^+}{\partial n}, \quad \varphi^+ = \varphi^-, \quad \text{on } S_2, \quad (2.101)$$

$$\varphi_3(\infty) = 0. \quad (2.102)$$

Here:  $\epsilon_1$  and  $\epsilon_+(\omega)$  are dielectric permittivities for the core and metallic nanoshell, respectively.

The electric potential of this sourceless field can be represented as an electric potential of single layers of electric charges  $\sigma_1$  and  $\sigma_2$  distributed over  $S_1$  and  $S_2$ ,

respectively:

$$\varphi(Q) = \frac{1}{4\pi\epsilon_0} \left[ \oint_{S_1} \frac{\sigma_1(M)}{r_{MQ}} dS_M + \oint_{S_2} \frac{\sigma_2(M)}{r_{MQ}} dS_M \right]. \quad (2.103)$$

In other words, single layers of electric charges  $\sigma_1$ (on  $S_1$ ) and  $\sigma_2$ (on  $S_2$ ) may create the same electric field in homogeneous space with  $\epsilon_0$  as the resonant source-free electric field that may exist in the presence of the nanoshell and dielectric core (see Figure 2.14(b)). It is apparent that the potential given by the formula (2.103) satisfies the Laplace equations (2.97)-(2.99) and continuity conditions on  $S_1$  and  $S_2$ . By using formula (2.20), it can be concluded that the boundary conditions (2.100)-(2.101) for normal derivatives will be satisfied if  $\sigma_1$  and  $\sigma_2$  are solutions of the following coupled homogeneous boundary integral equations:

$$\begin{aligned} & \epsilon_1 \left[ 2\pi\sigma_1(Q) + \oint_{S_1} \sigma_1(M) \frac{\mathbf{r}_{MQ} \cdot \mathbf{n}_Q}{r_{MQ}^3} dS_M + \oint_{S_2} \sigma_2(M) \frac{\mathbf{r}_{MQ} \cdot \mathbf{n}_Q}{r_{MQ}^3} dS_M \right] \\ = & \epsilon_+ \left[ -2\pi\sigma_1(Q) + \oint_{S_1} \sigma_1(M) \frac{\mathbf{r}_{MQ} \cdot \mathbf{n}_Q}{r_{MQ}^3} dS_M + \oint_{S_2} \sigma_2(M) \frac{\mathbf{r}_{MQ} \cdot \mathbf{n}_Q}{r_{MQ}^3} dS_M \right], \end{aligned} \quad (2.104)$$

$$\begin{aligned} & \epsilon_0 \left[ -2\pi\sigma_2(Q) + \oint_{S_1} \sigma_1(M) \frac{\mathbf{r}_{MQ} \cdot \mathbf{n}_Q}{r_{MQ}^3} dS_M + \oint_{S_2} \sigma_2(M) \frac{\mathbf{r}_{MQ} \cdot \mathbf{n}_Q}{r_{MQ}^3} dS_M \right] \\ = & \epsilon_+ \left[ 2\pi\sigma_2(Q) + \oint_{S_1} \sigma_1(M) \frac{\mathbf{r}_{MQ} \cdot \mathbf{n}_Q}{r_{MQ}^3} dS_M + \oint_{S_2} \sigma_2(M) \frac{\mathbf{r}_{MQ} \cdot \mathbf{n}_Q}{r_{MQ}^3} dS_M \right]. \end{aligned} \quad (2.105)$$

Thus, source-free electric fields may exist only for such negative values of permittivity  $\epsilon_+(\omega)$  that the coupled homogeneous integral equations (2.104)-(2.105) have non-zero solutions. By discretizing integral operators in the above integral equations, we arrive at the following generalized eigenvalue problem for  $\epsilon_+$ :

$$\begin{bmatrix} \epsilon_1(K_{11} + 2\pi I) & \epsilon_1 K_{12} \\ \epsilon_1 K_{12} & \epsilon_0(K_{22} - 2\pi I) \end{bmatrix} \begin{bmatrix} \vec{X}_1 \\ \vec{X}_2 \end{bmatrix} = \epsilon_+ \begin{bmatrix} K_{12} - 2\pi I & K_{12} \\ K_{12} & K_{22} + 2\pi I \end{bmatrix} \begin{bmatrix} \vec{X}_1 \\ \vec{X}_2 \end{bmatrix}, \quad (2.106)$$



where matrices  $K_{ij}$  are discretized versions of the corresponding integral operators in (2.104)-(2.105),  $\vec{X}_2$  and  $\vec{X}_2$  are discretized versions of  $\sigma_1(M)$  and  $\sigma_2(M)$ , respectively, while  $I$  is the identity matrix. The solution of the generalized eigenvalue problem yields the resonance values of  $\epsilon_+$ , and then the appropriate dispersion relation  $\epsilon_+(\omega)$  can be employed to find the resonance frequencies for metallic nanoshells. Since the integral operators in (2.104) and (2.105) are compact, the spectrum is discrete. Furthermore it can be shown that all the eigenvalues associated with the generalized eigenvalue problem (2.97)-(2.101) are real and negative.

It can be observed that the mathematical structure of boundary integral equation (2.104)-(2.105) is invariant with respect to the simultaneous and identical scaling of  $S_1$  and  $S_2$ , i.e., the scaling of the dimensions of the shell. This results in the unique property of plasmon resonances: *resonance frequencies depend on shell shapes but they are scale invariant with respect to shell dimensions, provided that these dimensions are appreciably smaller than the free-space wavelength.*

Table 2.5: Comparison of the resonance wavelengths for Au spherical nanoshells with silicon cores.

	Shell1	Shell2
Inner/outer radius	60/80 nm	55/75nm
Experimental results [27]	752 nm	717 nm
Computational results	795 nm	764 nm

The above integral equation based generalized eigenvalue problem has been solved by using the discretization technique described in Section 2.3. Table 2.5 presents the results for the plasmon resonances of gold spherical nanoshells with

silicon cores computed by using our technique and experimentally measured in [27]. The dispersion relation for gold published in [68] has been used in calculations. This table reveals a fairly good agreement between the experimental and computational results.

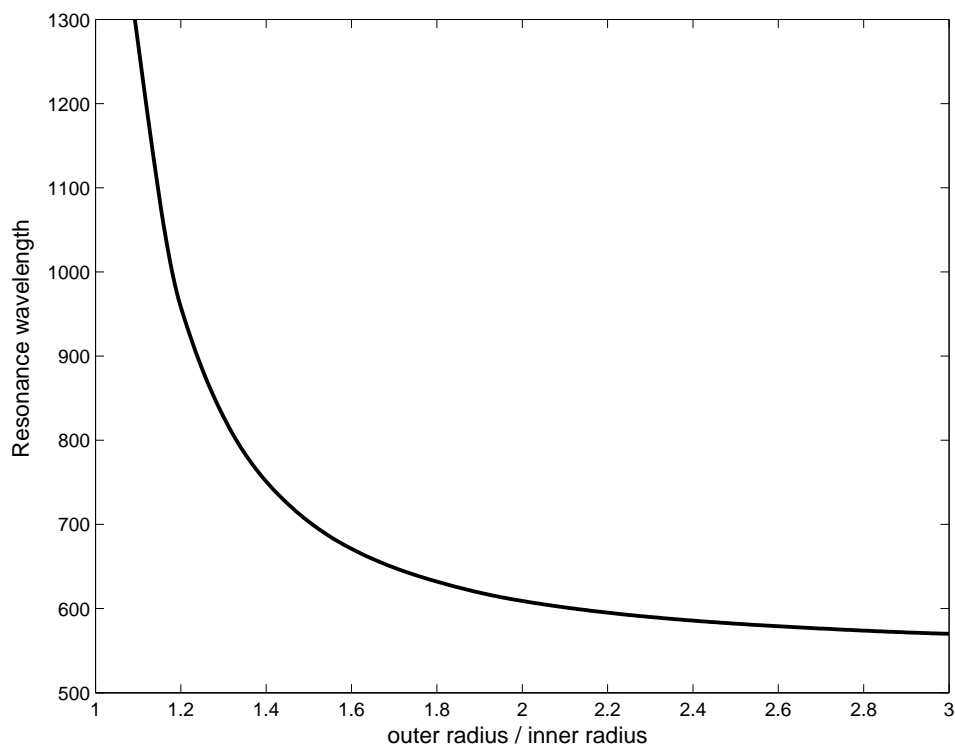


Figure 2.15: Plasmon resonant wavelengths for Au spherical nanoshells with different shell thickness. The core of these shells is silicon.

The resonance wavelength of gold spherical nanoshells (with silicon core) has been also computed for various ratios of inner and outer radius. The numerical results are illustrated in Figure 2.15. This figure clearly reveals that the resonance wavelength of nanoshell structures can be tuned within a wide range (from visible to near infrared) by adjusting the thickness of the shell.

## 2.4.2 Analytical results for spherical and ellipsoidal shells

For some simple geometries, it is possible to pursue analytical solutions for the boundary value problem (2.97)-(2.101). In the following, we demonstrate these solutions for spherical and ellipsoidal nanoshells and discuss the “twin” spectra phenomena associated with these shell structures. We also compare these analytical results with numerical computations of the generalized eigenvalue problem.

For spherical shells, the solution of the boundary value problem (2.97)-(2.101) can be represented in terms of the spherical harmonics:

$$\varphi_1(r, \theta, \phi) = Ar^l Y_{lm}(\theta, \phi), \quad (2.107)$$

$$\varphi_2(r, \theta, \phi) = [Br^l + Cr^{-(l+1)}]Y_{lm}(\theta, \phi), \quad (2.108)$$

$$\varphi_3(r, \theta, \phi) = Dr^{-(l+1)}Y_{lm}(\theta, \phi), \quad (2.109)$$

where  $A, B, C$  and  $D$  are unknown coefficients. By substituting (2.107)-(2.109) into boundary conditions (2.100)-(2.101), the linear homogeneous equations for the four unknown coefficients are obtained. The occurrence of plasmon resonances implies the existence of non-zero solutions to these equations. The existence of non-zero solution, in turn, requires that the determinant of the above homogeneous equations is equal to zero. In this way, the following quadratic equation for  $\epsilon_+$  can be derived:

$$\epsilon_{+l}^2 + \frac{(\epsilon_1 + \epsilon_0)l(l+1) + \epsilon_1 l^2 (r_2/r_1)^3 + \epsilon_0 (l+1)^2 (r_2/r_1)^3}{l(l+1)[(r_2/r_1)^3 - 1]} \epsilon_{+l} + \epsilon_1 \epsilon_0 = 0, \quad (2.110)$$

where  $r_1$  and  $r_2$  are the inner radius and outer radius of the spherical nanoshell, respectively. It turns out that for the spherical nanoshell structure an interesting phenomenon of twin spectra occurs. The essence of this phenomenon is that for any

Table 2.6: Comparison of the resonance values of  $\epsilon_+$  for spherical nanoshells,  $\epsilon_1 = 5\epsilon_0$ .

	Shell1	Shell2
$r_2/r_1$	1.5:1	20:1
$l = 1$ (Theoretical)	-8.32,-0.60	-2.50,-1.99
$l = 1$ (Computational)	-8.35,-0.60	-2.51,-1.99
$l = 2$ (Theoretical)	-8.79,-0.58	-3.32,-1.51
$l = 2$ (Computational)	-8.83,-0.57	-3.34,-1.50
$l = 3$ (Theoretical)	-9.15,-0.56	-3.71,-1.34
$l = 3$ (Computational)	-9.21,-0.55	-3.75,-1.33

resonant mode associated with index  $l$  there are two resonant values  $\epsilon_{+l}^{(1)}$  and  $\epsilon_{+l}^{(2)}$  related by the formula:

$$\epsilon_{+l}^{(1)} = \frac{\epsilon_1 \epsilon_0}{\epsilon_{+l}^{(2)}}. \quad (2.111)$$

Indeed, formula (2.111) is the immediate consequence of equation (2.110). Table 2.6 presents the results for plasmon resonances in spherical nanoshells computed by using the integral equation based numerical technique and the analytical formula (2.110). This table illustrates an excellent agreement between the theoretical and computational results. It is clear that the twin values of  $\epsilon_{+l}$  satisfy (2.111).

In the case of ellipsoidal nanoshells, spatially uniform resonance modes can be easily found analytically. For these modes the relation between the polarization  $\mathbf{P}$  of the shell and applied uniform field  $\mathbf{E}_0$  can be expressed in the form:

$$\begin{bmatrix} \alpha_x^+ & 0 & 0 \\ 0 & \alpha_y^+ & 0 \\ 0 & 0 & \alpha_y^+ \end{bmatrix} \mathbf{P} = \mathbf{E}_0. \quad (2.112)$$

By using ellipsoidal coordinates [39], the following formulas for  $\alpha_x^+$ ,  $\alpha_y^+$  and  $\alpha_z^+$  can be derived:

$$\alpha_i^+ = \frac{[\epsilon_+ + (\epsilon_1 - \epsilon_+) (N_i^{(1)} - fN_1^{(2)})] [\epsilon_0 + (\epsilon_+ - \epsilon_0)N_i^{(2)}] + fN_i^{(2)}\epsilon_+(\epsilon_1 - \epsilon_+)}{\nu \{(\epsilon_+ - \epsilon_0) [\epsilon_+ + (\epsilon_1 - \epsilon_+) (N_i^{(1)} - fN_1^{(2)})] + f\epsilon_+(\epsilon_1 - \epsilon_+)\}}, \quad (2.113)$$

where  $i = x, y, z$ ,

$$\nu = \frac{4\pi}{3}a_2b_2c_2, \quad f = \frac{a_1b_1c_1}{a_2b_2c_2}, \quad (2.114)$$

$a_1, b_1, c_1$  are semi-axes of the inner ellipsoid,  $a_2, b_2, c_2$  are semi-axes of the outer ellipsoid, while depolarization factors  $N_i$  are given by the formulas:

$$N_x = \frac{abc}{2} \int_0^\infty \frac{d\lambda}{(\lambda + a^2)\sqrt{(\lambda + a^2)(\lambda + b^2)(\lambda + c^2)}}, \quad (2.115)$$

$$N_y = \frac{abc}{2} \int_0^\infty \frac{d\lambda}{(\lambda + b^2)\sqrt{(\lambda + a^2)(\lambda + b^2)(\lambda + c^2)}}, \quad (2.116)$$

$$N_z = \frac{abc}{2} \int_0^\infty \frac{d\lambda}{(\lambda + c^2)\sqrt{(\lambda + a^2)(\lambda + b^2)(\lambda + c^2)}}, \quad (2.117)$$

and  $N_x + N_y + N_z = 1$ . In the case of axially symmetric ellipsoids ( $b = c$ ), the above formulas are reduced to:

$$N_x = \frac{1 - \beta^2}{e^2} \left[ \frac{1}{2\beta} \ln \left( \frac{1 + \beta}{1 - \beta} \right) - 1 \right], \quad N_y = N_z = \frac{1 - N_x}{2}, \quad (2.118)$$

$$\beta^2 = 1 - \frac{b^2}{a^2}. \quad (2.119)$$

The existence of resonances implies that the matrix in (2.112) is singular. According to (2.113), this means that the resonance values of  $\epsilon_+(\omega)$  can be computed by solving the following quadratic equation:

$$\begin{aligned} & (1 - f - N_i^{(1)} + fN_i^{(2)}) N_i^{(2)} \epsilon_+^2 + (N_i^{(1)} - fN_i^{(2)}) (1 - N_i^{(2)} \epsilon_1 \epsilon_0) \\ & + [(1 - N_i^{(1)} + fN_i^{(2)}) (1 - N_i^{(2)}) + (f + N_i^{(1)} - fN_i^{(2)}) N_i^{(2)} \epsilon_1] \epsilon_+ = 0. \end{aligned} \quad (2.120)$$

If the shell has self-similar boundaries  $S_1$  and  $S_2$ , the inner ellipsoid and the outer ellipsoid have the same depolarization factors. Then, formula (2.120) is reduced to:

$$\epsilon_+^2 + \frac{[(1 - N_i + fN_i)(1 - N_i)\epsilon_0 + (f + N_i - fN_i)N_i\epsilon_1]}{(1 - f)(1 - N_i)N_i}\epsilon_+ + \epsilon_1\epsilon_0 = 0. \quad (2.121)$$

Equation (2.121) has the same structure as formula (2.110). This suggests that the phenomenon of twin spectra occurs for ellipsoidal shells as well, albeit only for uniform modes. The two resonant values  $\epsilon_+^{(1)}$  and  $\epsilon_+^{(2)}$  are related by the formula:

$$\epsilon_+^{(1)} = \frac{\epsilon_1\epsilon_0}{\epsilon_+^{(2)}}. \quad (2.122)$$

Table 2.7 presents the results for plasmon resonances in ellipsoidal nanoshells computed by using the integral equation based numerical technique and the analytical formula (2.121). This table illustrates a very good agreement between the theoretical and computational results.

Table 2.7: Comparison of the resonance values of  $\epsilon_+$  for ellipsoidal nanoshells,  $\epsilon_1 = 15.2\epsilon_0$ .

	Shell1	Shell2
$a : b : c$	1.414:1:1	1.414:1:1
Shell ratio	4:3	7:5
$\epsilon_+$ (Theoretical)	-25.00,-0.61	-21.04,-0.71
$\epsilon_+$ (Computational)	-25.83,-0.59	-22.08,-0.69

In conclusion, the analysis of plasmon resonances in metallic nanoshells with dielectric cores can be reduced to an generalized eigenvalue problem. For spherical and ellipsoidal nanoshells, simple analytical expressions are obtained for the direct calculation of plasmon resonant frequencies. The wide range tunability of plasmon

resonant frequencies via adjusting the thickness of shells has been illustrated by numerical examples. Furthermore, it can be seen from formulas (2.106), (2.110) and (2.120), the dielectric permittivity of the core also plays a role in the determination of the plasmon resonant frequencies, which adds additional capability to tune the resonant frequency.

## Chapter 3

### **Fast Multipole Method for the Solution of Eigenvalue**

#### **Problem**

In this chapter, the fast multipole method (FMM) is introduced for the solution of large scale eigenvalue problem. The applicability of FMM and its implementation in the iterative algorithm are presented in detail. Numerical results which illustrate the efficiency of FMM compared with traditional method for the numerical analysis of plasmon resonances are presented. In addition, a semi-analytical method based on multipole expansions is developed for the analysis of plasmon resonances in spherical nanoparticles.



### 3.1 Why fast multipole method is needed?

In Chapter 2, we have demonstrated that the plasmon resonance frequencies can be directly obtained by solving the following homogeneous boundary integral equations

$$\sigma(Q) = \frac{\lambda}{2\pi} \oint_S \sigma(M) \frac{\mathbf{r}_{MQ} \cdot \mathbf{n}_Q}{r_{MQ}^3} dS_M, \quad (3.1)$$

where  $\lambda$  is given by (2.22). By using the discretization technique described in section 2.3, this eigenvalue problem can be written in the matrix form as

$$X_i = \frac{\lambda}{2\pi} \sum_{j=1}^N \omega_{ij} X_j, \quad (3.2)$$

where  $X_i$  and  $\omega_{ij}$  are defined in (2.89) and (2.91), respectively. The solutions of the eigenvalue problem (3.2) is usually obtained by using iterative techniques, which require matrix-vector product  $B \leftarrow Av^k$  computations. It is apparent that when matrix  $A$  is fully populated, the multiplication  $Av^k$  is accomplished in  $O(N^2)$  operations. For large  $N$ , the computation cost can be prohibitive. In order to solve this problem, we have to seek a more advanced algorithm. It turns out that fast multipole method (FMM) is ideally suitable for this situation and can appreciably save the cost of CPU time and memory.

The fast multipole method is regarded as one of the greatest algorithms of the 20th century [65, 75, 76]. This algorithm allows the product of particular dense matrices with a vector to be evaluated approximately (to a specified precision) in  $O(N \log N)$  operations, when direct multiplication requires  $O(N^2)$  operations (when  $N$  is large, the save is considerable). The FMM is originally proposed by Rokhlin [77] as a fast scheme for accelerating the numerical solution of the Laplace equation

in two dimensions. It was further improved by Greengard and Rokhlin [64, 79] when it was applied to particle simulations. Since then, FMM has wide applications in astrophysics, molecular dynamics, computational fluid dynamics and radar scattering, etc. For example, Mayergoyz et al applied FMM in the nonlinear magnetostatic calculations [78] recently. Furthermore, Gumerov and Duraiswami published a monograph [65] in 2005 which reveals the most recent advances in FMM. Its central strategy is the hierarchical decomposition of the data-space in the form of a quadtree (or octtree for the 3-dimensional case). This hierarchical decomposition is used to cluster particles in the computational domain at various spatial lengths and compute interactions with other clusters that are sufficiently far away by means of series expansions (see Figures 3.1 and 3.2).

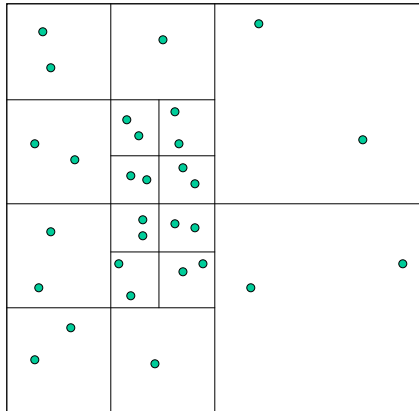


Figure 3.1: Space partitioning.

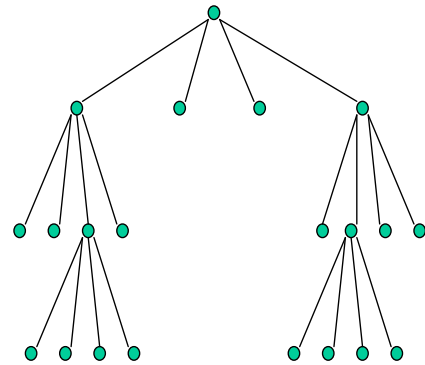


Figure 3.2: Data structure.

FMM does not work for any matrix-vector multiplication, instead, it only works for cases that satisfy the following conditions: (1) two sets of points (for example, source points and evaluation points) are involved in a vector space; (2) the

dense matrix is generated by potential (kernel) functions; (3) these functions can be factorized and have local and multipole expansions; (4) the local expansion coefficients can be  $R|R$ -translated (i.e., local-to-local translation) and the multipole expansion coefficients can be  $S|S$ -translated (i.e., multipole-to-multipole translation); (5) The multipole expansion coefficients can be  $S|R$ -translated (i.e., multipole-to-local translation). Since the matrix elements of (3.2) are derived from a  $1/r$ -type kernel, it can be shown that all the above conditions above are met.

## 3.2 Factorization and translations of the kernel function

In this section, we examine the applicability of FMM to our  $1/r$ -type kernel function from the mathematic point of view. The key components such as factorization, expansion and translation are described below [65, 80].

### 3.2.1 Factorization of the kernel function

The kernel function of integral equation (3.1) is:

$$\omega_{ij} = \int_{\Delta S_i} \frac{\mathbf{r}_{M_j Q_i} \cdot \mathbf{n}_{Q_i}}{r_{M_j Q_i}^3} dS_i. \quad (3.3)$$

If the patch is small enough, we can assume the distribution of the physical quantity is uniform on the patch, the integral in the last equation becomes a multiplication

$$\omega_{ij} = \frac{\mathbf{r}_{M_j Q_i} \cdot \mathbf{n}_{Q_i}}{r_{M_j Q_i}^3} \Delta S_i, \quad (3.4)$$

and it is indeed the gradient of  $1/r_{MQ}$ :

$$\omega_{ij} = \nabla \left( \frac{1}{r_{M_j Q_i}} \right) \cdot \mathbf{n}_{Q_i} \Delta S_i, \quad (3.5)$$

where

$$(3.6)$$

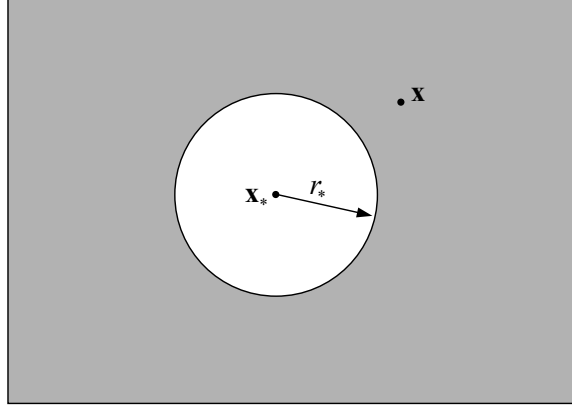


Figure 3.3: Multipole expansion.

Now we start from the factorization of kernel  $\frac{1}{r}$ . The expansion in the three-dimensional case can be obtained according to the additional theorem of spherical harmonics:

$$\frac{1}{|\mathbf{x} - \mathbf{x}'|} = \sum_{l=1}^{\infty} \sum_{m=-l}^l \frac{4\pi}{2l+1} \frac{r_{<}^l}{r_{>}^{l+1}} Y_{lm}^*(\theta', \phi') Y_{lm}(\theta, \phi), \quad (3.7)$$

where

$$Y_{lm}^*(\theta, \phi) = (-1)^m Y_{l,-m}(\theta, \phi), \quad (3.8)$$

the  $\mathbf{x}'(r', \theta', \phi')$  and  $\mathbf{x}(r, \theta, \phi)$  indicate the source point and evaluation point respectively. Supposing we select the expansion center at  $\mathbf{x}_*(r_1, \theta_1, \phi_1)$ , we can introduce the multipole expansion (S-expansion) and local expansion (R-expansion). Let  $\mathbf{x}$  be the evaluation point and  $\mathbf{x}'$  be the source point. If  $|\mathbf{x} - \mathbf{x}_*| > |\mathbf{x}' - \mathbf{x}_*|$ , the multipole expansion is defined as the following (see Figure 3.3):

$$\frac{1}{|(\mathbf{x} - \mathbf{x}_*) - (\mathbf{x}' - \mathbf{x}_*)|} = \sum_{l=1}^{\infty} \sum_{m=-l}^l C_{lm}(\mathbf{x}' - \mathbf{x}_*) S_{lm}(\mathbf{x} - \mathbf{x}_*), \quad (3.9)$$

where  $C_{lm}(\mathbf{x}' -$

$$\frac{n(\mathbf{x} - \mathbf{x}_*)}{|\mathbf{x} - \mathbf{x}_*|^{l+1}}.$$

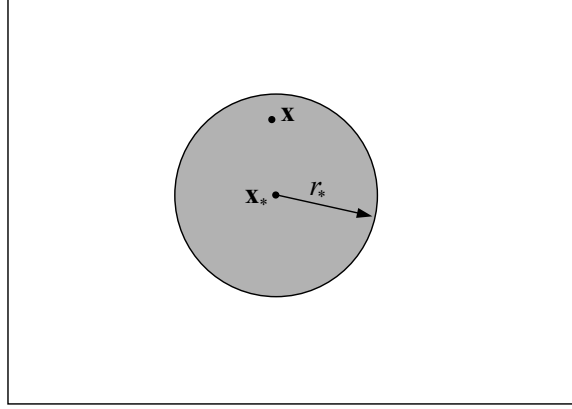


Figure 3.4: Local expansion.

For the case  $|\mathbf{x}' - \mathbf{x}_*| > |\mathbf{x} - \mathbf{x}_*|$ , the R-expansion is defined as following:

$$\frac{1}{|(\mathbf{x} - \mathbf{x}_*) - (\mathbf{x}' - \mathbf{x}_*)|} = \sum_{l=1}^{\infty} \sum_{m=-l}^l B_{lm}(\mathbf{x}' - \mathbf{x}_*) R_{lm}(\mathbf{x} - \mathbf{x}_*), \quad (3.10)$$

where  $B_{lm}(\mathbf{x}' - \mathbf{x}_*) = \frac{4\pi}{2l+1} \frac{Y_{lm}^*(\mathbf{x}' - \mathbf{x}_*)}{|\mathbf{x}' - \mathbf{x}_*|^{l+1}}$ ,  $R_{lm}(\mathbf{x} - \mathbf{x}_*) = |\mathbf{x} - \mathbf{x}_*|^l Y_{lm}(\mathbf{x} - \mathbf{x}_*)$ .

### 3.2.2 Translation in 3D

In FMM algorithm, the multipole (S-) expansion and local (R-) expansion of a potential need to be translated to the same type of expansion at different expansion centers or a different type of expansion at different expansion centers. In the following, we discuss three types of translation: the “multipole-to-multipole” translation, the “local-to-local” translation and the “multipole-to-local” translation.

**“Multipole-to-multipole” translation.** Consider the multipole expansion in formula (3.9) with expansion center  $\mathbf{x}_*(r_1, \theta_1, \phi_1)$ , this expansion can be

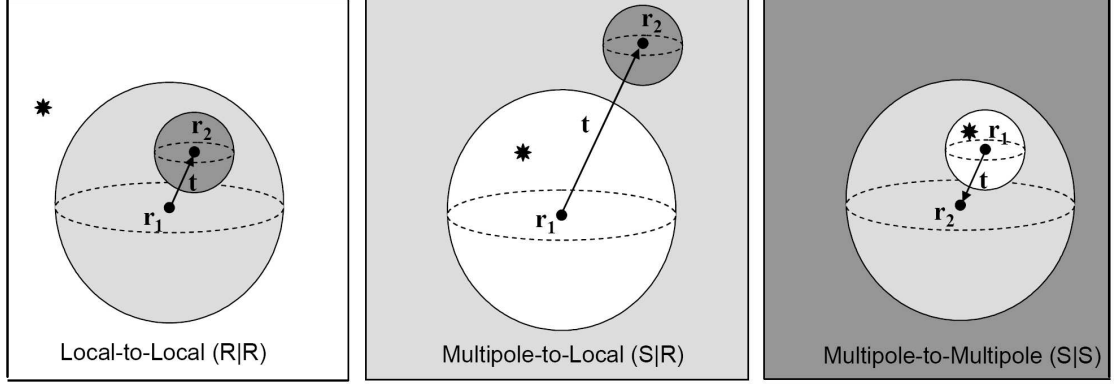


Figure 3.5: Illustration of local-to-local ( $R|R$ ), multipole-to-local ( $S|R$ ), and multipole-to-multipole ( $S|S$ ) translations from expansion center  $\mathbf{r}_1$  to expansion center  $\mathbf{r}_2$  (translation vector  $\mathbf{t} = \mathbf{r}_2 - \mathbf{r}_1$ ). The star shows location of a source. Expansion about center  $\mathbf{r}_1$  is valid inside the lighter and darker gray area, while expansion about center  $\mathbf{r}_2$  is valid only in the darker gray area.

re-expanded with the center at  $\mathbf{x}'_*(r_2, \theta_2, \phi_2)$  and expressed as:

$$\frac{1}{|\mathbf{x} - \mathbf{x}'|} = \sum_{j=0}^{\infty} \sum_{k=-j}^j M_{jk}(\mathbf{x}' - \mathbf{x}'_*) S_{jk}(\mathbf{x} - \mathbf{x}'_*), \quad (3.11)$$

where

$$M_{jk} = \sum_{n=0}^{\infty} \sum_{m=-n}^n \frac{O_{j-n}^{k-m} J_m^{k-m} A_n^m A_{j-n}^{k-m}}{A_j^k} |\mathbf{x}' - \mathbf{x}'_*|^n Y_n^{-m}(\mathbf{x}' - \mathbf{x}'_*), \quad (3.12)$$

$$A_n^m = \frac{(-1)^n}{\sqrt{(n-m)!(n+m)!}}, \quad (3.13)$$

$$J_m^{m'} = \begin{cases} (-1)^{\min(|m'|, |m|)}, & m \cdot m' < 0, \\ 1, & \text{otherwise.} \end{cases} \quad (3.14)$$

**“Local-to-local” translation.** Consider the local expansion in formula (3.10) with

expansion center  $\mathbf{x}_*(r_1, \theta_1, \phi_1)$ , this expansion can be re-expanded with the center at  $\mathbf{x}'_*(r_2, \theta_2, \phi_2)$  and expressed as:

$$\frac{1}{|\mathbf{x} - \mathbf{x}'|} = \sum_{j=0}^{\infty} \sum_{k=-j}^j L_{jk}(\mathbf{x}' - \mathbf{x}'_*) R_{jk}(\mathbf{x}' - \mathbf{x}'_*), \quad (3.15)$$

where

$$L_{jk} = \sum_{n=0}^{\infty} \sum_{m=-n}^n \frac{O_n^m J_{n-j, m-k}^m A_j^k A_{n-j}^{m-k}}{A_n^m} |\mathbf{x}' - \mathbf{x}'_*|^{n-j} Y_{n-j}^{m-k}(\mathbf{x}' - \mathbf{x}'_*), \quad (3.16)$$

$$J_{n,m}^{m'} = \begin{cases} (-1)^n (-1)^m, & m \cdot m' < 0, \\ (-1)^n (-1)^{m'-m}, & m \cdot m' < 0 \text{ and } |m'| < |m|, \\ (-1)^n, & \text{otherwise,} \end{cases} \quad (3.17)$$

and  $A_n^m$  defined in (3.13).

**“Multipole-to-local” translation.** Consider the multipole expansion in formula (3.9) with expansion center  $\mathbf{x}_*(r_1, \theta_1, \phi_1)$ , this expansion can be re-expanded to a local expansion with the center at  $\mathbf{x}'_*(r_2, \theta_2, \phi_2)$  and expressed as:

$$\frac{1}{|\mathbf{x} - \mathbf{x}'|} = \sum_{j=0}^p \sum_{k=-j}^j L_{jk}(\mathbf{x}' - \mathbf{x}'_*) R_{jk}(\mathbf{x}' - \mathbf{x}'_*), \quad (3.18)$$

where

$$L_{jk} = \sum_{n=0}^p \sum_{m=-n}^n \frac{O_n^m (-1)^{n+k} A_n^m A_j^k}{A_{n+j}^{m-k}} |\mathbf{x}' - \mathbf{x}'_*|^{-(n+j+1)} Y_{n+j}^{m-k}(\mathbf{x}' - \mathbf{x}'_*), \quad (3.19)$$

with  $A_n^m$  defined in (3.16).

The translations presented above are infinite in dimension and the translations are exact operations. However, in the actual FMM algorithm, a truncated matrix of size  $p^2 \times p^2$  (for 3D case) is used instead of the actual transformation matrix,

thus introducing an error in the computation. This truncation is desirable because it reduces the computational complexity, and it can be shown that [64, 65], for convergent series, the error introduced in this step is bounded and can be reduced to an arbitrarily small number by increasing the truncation number  $p$ . It is also possible to determine what truncation number  $p$  to use in order to achieve a desired level of accuracy [65, 80].

### 3.2.3 Differentiation of the $\frac{1}{r}$ kernel in 3D

Now we consider the gradient of kernel  $1/r_{MQ}$  since the real computation relies on it. After factorization, the gradient is carried out on each item of the series. So we need to know how to calculate the gradient of the spherical harmonics. Since the data structure and the space discretization requires the Cartesian coordinates, we also need to convert the differentiation of spherical harmonics from spherical coordinates to the Cartesian coordinates. At the same time, we will employ the recursive relation of Legendre functions to get the expression. The derivation is straightforward but somewhat lengthy, in the following, we will only give the results [65].

In spherical coordinates, the gradient is defined as

$$\nabla_x \left( \frac{1}{|\mathbf{y}_j - \mathbf{x}_i|} \right) = \left[ \mathbf{a}_r \frac{\partial}{\partial r_x} + \mathbf{a}_\theta \frac{\partial}{r_x \partial \theta} + \mathbf{a}_\phi \frac{\partial}{r_x \sin \theta_x \phi} \right], \quad (3.20)$$

$$\sum_{n=0}^{\infty} \sum_{m=-n}^n \frac{4\pi}{2n+1} \frac{r_{\leq}^n}{r_{>}^{n+1}} Y_{nm}^*(\theta_{x_i}, \phi_{x_i}) Y_{nm}(\theta_{y_j}, \phi_{y_j}). \quad (3.21)$$

The conversions between two coordinate systems are given by

$$x = r \sin \theta \cos \phi, \quad y = r \sin \theta \sin \phi, \quad z = r \cos \theta, \quad (3.22)$$



$$\mu = \cos \theta, \quad (3.23)$$

$$D_x = \frac{1}{2} (D_{xy} + \overline{D_{xy}}) \quad (3.24)$$

$$D_y = \frac{i}{2} (D_{xy} - \overline{D_{xy}}), \quad (3.25)$$

$$D_z = \frac{\partial}{\partial z} = \mu \frac{\partial}{\partial r} + \frac{1 - \mu^2}{r} \frac{\partial}{\partial \mu}, \quad (3.26)$$

where

$$D_{xy} = \frac{\partial}{\partial x} + i \frac{\partial}{\partial y} = \frac{e^{i\phi}}{r\sqrt{1-\mu^2}} \left[ (1-\mu^2) \left( r \frac{\partial}{\partial r} - \mu \frac{\partial}{\partial \mu} \right) + i \frac{\partial}{\partial \phi} \right], \quad (3.27)$$

$$\overline{D_{xy}} = \frac{\partial}{\partial x} - i \frac{\partial}{\partial y} = \frac{e^{-i\phi}}{r\sqrt{1-\mu^2}} \left[ (1-\mu^2) \left( r \frac{\partial}{\partial r} - \mu \frac{\partial}{\partial \mu} \right) - i \frac{\partial}{\partial \phi} \right]. \quad (3.28)$$

The recursive relations of the associated Legendre functions are

$$\mu P_n^m = \frac{1}{2n+1} \left[ (n+m) P_{n-1}^m + (n-m+1) P_{n+1}^m \right], \quad (3.29)$$

$$(1-\mu^2) \frac{d}{d\mu} P_n^m = \frac{1}{2n+1} \left[ (n+1)(n+m) P_{n-1}^m - n(n-m+1) P_{n+1}^m \right]. \quad (3.30)$$

Finally, we can get:

$$D_z (R_n^m) = a_n^m R_{n-1}^m, \quad (3.31)$$

$$D_z (S_n^m) = -a_{n+1}^m S_{n+1}^m, \quad (3.32)$$

where:

$$a_n^m = \sqrt{\frac{2n+1}{2n-1} (n^2 - m^2)}, \quad (3.33)$$

$$R_n^m = r^n Y_n^m(\theta, \phi), \quad (3.34)$$

$$S_n^m = r^{-n-1} Y_n^m(\theta, \phi), \quad (3.35)$$

$$Y_n^m(\theta, \phi) = (-1)^m \sqrt{\frac{2n+1}{4\pi} \frac{(n-|m|)!}{(n+|m|)!}} P_n^{|m|}(\mu) e^{im\phi}, \quad (3.36)$$

$$D_{xy}(R_n^m) = b_n^m R_{n-1}^{m+1}, \quad (3.37)$$

$$D_{xy}(S_n^m) = c_{n+1}^{-m-1} S_{n+1}^{m+1}, \quad (3.38)$$

$$\overline{D_{xy}}(R_n^m) = b_n^{-m} R_{n-1}^{m-1}, \quad (3.39)$$

$$\overline{D_{xy}}(S_n^m) = c_{n+1}^{m-1} S_{n+1}^{m-1}, \quad (3.40)$$

where

$$b_n^m = \begin{cases} -\sqrt{\frac{(2n+1)(n-m-1)(n-m)}{(2n-1)}}, & 0 \leq m \leq n, \\ \sqrt{\frac{(2n+1)(n-m-1)(n-m)}{(2n-1)}}, & -n \leq m \leq 0, \\ 0, & |m| > n \end{cases} \quad (3.41)$$

$$c_n^m = \begin{cases} \sqrt{\frac{(2n-1)(n-m-1)(n-m)}{(2n+1)}}, & 0 \leq m \leq n, \\ -\sqrt{\frac{(2n-1)(n-m-1)(n-m)}{(2n+1)}}, & -n \leq m \leq 0, \\ 0, & |m| > n. \end{cases} \quad (3.42)$$

$$D_x(R_n^m) = \frac{1}{2}[b_n^m R_{n-1}^{m+1} + b_n^{-m} R_{n-1}^{m-1}], \quad (3.43)$$

$$D_x(S_n^m) = \frac{1}{2}[c_{n+1}^{-m-1} S_{n+1}^{m+1} + c_{n+1}^{m-1} S_{n+1}^{m-1}], \quad (3.44)$$

$$D_x(R_n^m) = \frac{i}{2}[b_n^m R_{n-1}^{m+1} - b_n^{-m} R_{n-1}^{m-1}], \quad (3.45)$$

$$D_x(S_n^m) = \frac{i}{2}[c_{n+1}^{-m-1} S_{n+1}^{m+1} - c_{n+1}^{m-1} S_{n+1}^{m-1}]. \quad (3.46)$$

So, the basic conclusion is that those multipole or local expansion coefficients can be expressed through recursive relations. This is very helpful for software implementation.

### 3.3 FMM algorithm and implementation

#### 3.3.1 FMM algorithm

Although the detailed description of FMM algorithm can be found in many references [65, 67, 79], in order to make this dissertation self-complete, the FMM algorithm is stated here in a short format. Before starting, we introduce some notation.  $\Phi_{l,i}$  is the  $p$ -term multipole expansion about the center of the box  $i$  at level  $l$ , describing the potential field outside box  $i$ 's neighbors due to all particles contained inside the box  $i$ .  $\Psi_{l,i}$  is the  $p$ -term local expansion about the center of the box  $i$  at level  $l$ , describing the potential field induced by all particles outside box  $i$ 's neighbors.  $\tilde{\Psi}_{l,i}$  is the  $p$ -term local expansion about the center of the box  $i$  at level  $l$ , describing the potential field induced by all particles outside the neighbor's of box  $i$ 's parent.

**Initialization.** Choose precision to be desired  $\epsilon$  and the number of levels  $n$  for the hierarchy data structure. Set up the hierarchical data structure and sort all points into the boxes at the finest level.

#### **Upward pass**

##### Step 1

For each box  $i$  at the finest level  $n$ , form the  $p$ -term multipole expansion  $\Phi_{n,i}$ , representing the potential field induced by all particles in the box. record the coefficients of each expansion for all boxes.

##### Step 2

For levels  $l = n - 1, n - 2, \dots, 2$ , for each box  $i$  at level  $l$ , use multipole-to-

multipole translation to shift the centers of the multipole expansions of its children boxes to the center of box  $j$  and merge them to form  $\Phi_{l,j}$  which represents the potential field induced by all particles in box  $j$ , or all particles in its children boxes. See Fig.3.6.

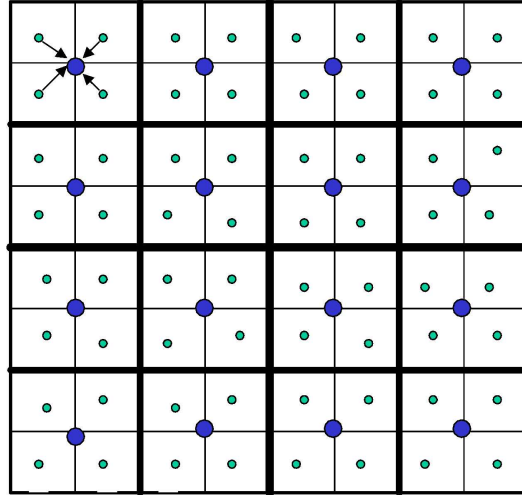


Figure 3.6: Step 2 of FMM algorithm: Multipole to multipole translation.

### Downward pass

#### Step 3

For levels  $n = 2, 3, \dots, n$ , for each box  $j$  at level  $l$ , use local-to-local translation (See Fig.3.7). to shift the center of local expansion  $\Psi_{l-1}$  of  $j$ 's parent box to the center of box  $j$  to form  $\tilde{\Psi}_{l,i}$ . Use multipole-to-local translation (See Figs. 3.8 and 3.9) to convert the multipole expansion of all boxes that is in the interaction list of box  $j$  to a local expansion about the center of box  $j$ , and add all these to  $\tilde{\Psi}_{l,i}$  to form  $\Psi_{l,i}$ , which represents the potential field induced by all particles outside box

$j$ 's neighbors.

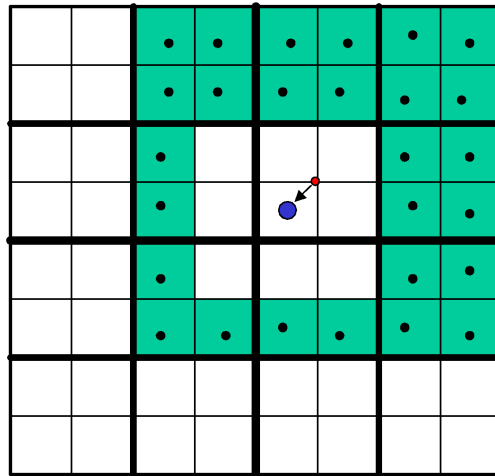


Figure 3.7: Step 3 of FMM algorithm: Local to Local translation.

Step 4

For all the boxes  $j$  at the finest level, for each particles at box  $j$ , evaluate  $\Phi_{n,j}$  at the particles position.

Step 5

For all the boxes  $j$  at the finest level, for each particles at box  $j$ , evaluate the interactions with particles in  $j$ 's neighbor boxes directly. The flowchart of above described FMM algorithm can be seen in Figure 3.10.

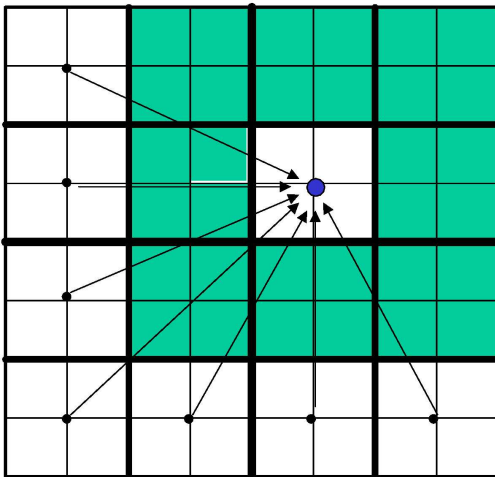


Figure 3.8: Step 3 of FMM algorithm: Multipole to local translation.

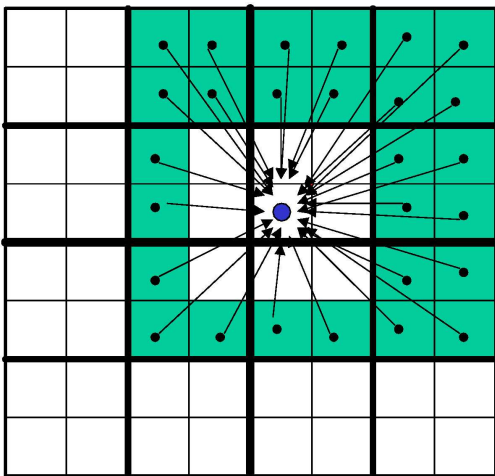


Figure 3.9: Step 3 of FMM algorithm: Multipole to local translation.

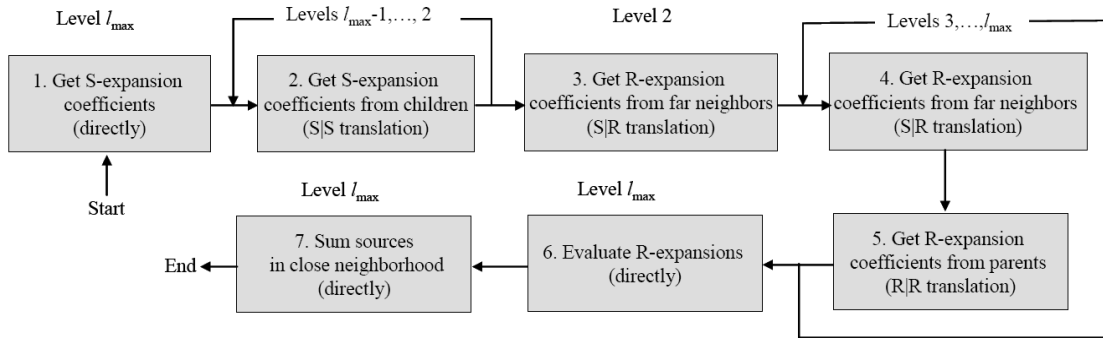


Figure 3.10: A flow chart of the standard FMM.

### 3.3.2 Data structure for FMM implementation

A key issue in the implementation of fast multipole methods is to establish a well-organized data structure. In order to exploit the observation that the effect of a cluster of particles at a certain distance may be approximated by a finite sum of series expansions using the equations described in previous sections, we need to organize the particles in a hierarchy of clusters. This hierarchy of clusters allows one to efficiently determine when the approximation is valid and therefore correlates to the overall performance of the FMM algorithm.

Since the regions of expansion validity are specified in terms of Euclidean distance, subdivision of space into  $d$ -dimensional cubes is convenient for range evaluation between points, which is usually called  $2^d$ -tree data structure. In the 3D case, the hierarchy tree structure can be seen in Figure 3.11. The main technique for working with 2d-trees (and k-d trees) is the bit-interleaving technique [81, 82]. This technique enables  $O(1)$ , or constant, algorithms for parent and sibling search and  $O(\log N)$  algorithms for neighbor and children search.

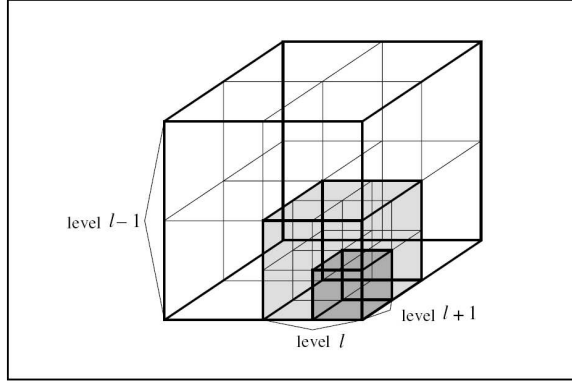


Figure 3.11: Hierarchical cells at three levels in three dimensions.

To efficiently determine the “Parent” box and “Children” box, we can index the boxes in the following way. Each box in the tree can be identified by assigning it a unique index among the  $2^d$  children of its parent box, and by knowing the index of its parent in the set of its grandparent’s children. Then the index of a box can be written as the string

$$\text{String}(n, l) = (N_1, N_2, \dots, N_l), \quad N_j = 0, \dots, 2^d - 1, \quad j = 1, \dots, l, \quad (3.47)$$

where  $l$  is the level at which the indexed box is located and  $N_j$  is the index of a box at level  $j$  containing that box. Now the indexing string can be converted to a single number as follows:

$$n = (2^d)^{l-1} \cdot N_1 + (2^d)^{l-2} \cdot N_2 + 2^d \cdot N_{l-1} + N_l. \quad (3.48)$$

Note that this index depends on the level  $l$  at which the box is considered and unless this information is included, different boxes could be described by the same index. The unique index of any box can be represented by the pair:

$$\text{UniversalIndex} = (n, l). \quad (3.49)$$



If the indexing at each level is performed in a consistent way, then we call such a indexing scheme “hierarchical”. A consistent hierarchical scheme has the following desirable properties.

1. *Determining the Parent:* Consider a box at level  $l$  of the  $2^d$ -tree, whose index is given by equation (3.48). It can be shown that the parent of this box is

$$\text{Parent}(n, l) = (\text{Parent}(n), l - 1). \quad (3.50)$$

2. *Determining the Children:* For the universal numbering system 3.49, to get the indices of all  $2^d$  children of a box represented by the string 3.47, the operation of finding the children is simply the calculation of the children numbers and assigning their level to  $l + 1$ :

$$\text{ChildrenAll}(n, l) = (\text{ChildrenAll}(n), l + 1). \quad (3.51)$$

The use of  $2d$ -trees makes obtaining parent and children indices very convenient. Indeed, the above operations are nothing but shift operations in the bit representation of  $n$ . Performing a right bit-shift operation on  $n$  by  $d$ -bits one can obtain the index of the parent. One can list all indices of the children boxes of  $n$  by a left bit-shift operation on  $n$  by  $d$ -bits and adding all possible combinations of  $d$ -bits.

In addition to find the “parent” and “children” for a box, the FMM also needs a way to determine neighbors and the box center for a given index  $(n, l)$  and the box index to which a given spatial point  $\mathbf{x}$  belongs. To do this, a spatial ordering in  $d$ -dimensional space should be introduced. Below, such an ordering and  $O(1)$  algorithms for these operations are introduced.

We first scale the computation domain (the largest box) to the unit cube. Any point  $\mathbf{x}$  in the original three-dimensional space now can be found given  $\bar{\mathbf{x}} \in [0, 1] \times [0, 1] \times [0, 1]$ . Since all the boxes are already ordered by their indices at a given level  $l$  from 0 to  $2^{l-1}$ , there is a straightforward correspondence between box indices and coordinates of points. For this reason, we have the following convenient operations.

3. *Finding the index of the box containing a given point.* Consider the relation between the coordinate of a point and the index of the box where the point is located. We note that the size of a box at each level is 1 placed at the position equal to the level number after the decimal in its binary record, and it can be shown that the operation is simply done by:

$$(n, l) = [2^{3l} \cdot \bar{x}]. \quad (3.52)$$

where  $[]$  means integral part.

4. *Finding the center of a given box.* This operation can be done through

$$\bar{x}_m(n, l) = 2^{-l} \cdot (n_l + 2^{-1}), \quad m = 1, 2, 3. \quad (3.53)$$

5. *Finding neighbors.* This operation to the  $k$ -neighbor can be done through

$$\text{Neighbor}_m = \begin{cases} n_m^-, n_m, n_m^+, & n_m \neq 0, 2^l - 1, \\ n_m, n_m^+, & n_m = 0, \\ n_m^-, n_m, & n_m = 2^l - 1. \end{cases} \quad (3.54)$$

where  $n_m^+ = n_m + k$ ,  $n_m^- = n_m - k$ ,  $m = 1, 2, 3$ .

The data structure and the indexing and ordering technique described above

have been implemented in code and it is proven to be very efficient and useful for FMM algorithm.

### 3.4 Numerical results

The algorithm outlined above has been implemented and extensively tested. We have used LAPACK for solving the eigenvalue problem, where the reverse communication function is ideally suitable for the inclusion of FMM codes for matrix-vector products. Figure 3.12 compares the speed of FMM algorithm and the direct summation scheme. It can be seen that the matching point is about  $N = 3000$  where FMM starts to be faster than direct summation. Figure 3.13 illustrates the error versus the truncation number  $p$ . Smaller  $p$  provides faster speed but compromises the accuracy. So it is always a tradeoff in this situation. In our computations,  $p = 5$  is used in most of the cases. The number of levels or the number of the sources in the finest box is also a parameter which needs to be optimized to achieve higher speed in FMM computation. Figure 3.14 tells us that the relation between CPU time and group parameters  $s$  is nonlinear.

Table 3.1 presents the comparison between the results computed by the using outlined technique and reported in [13] for the three silver spherical nanoparticle system (see Figure 3.15). The experimentally measured dispersion relation for silver published in [68] has been used in calculations. This table reveals a very good agreement between our results and experimental results reported in [83].

The testing of the method has been performed for the more complicated sys-

tem of 20nm gold nanospheres shown in Figure 3.16. The separation between the central sphere and surrounding spheres is 7nm. This structure is used to model the aggregation of gold nanospheres due to DNA hybridization [84]. The low density DNA solution is treated in computations as water. The calculations show that the resonance wavelength for a single nanosphere is 516nm, while the resonance wavelength for the group of 7 nanospheres shifts to 554nm. These results agree with the experimental results reported in [84] where it is reported that for single gold nanospheres the resonances occur at 525nm, while the resonances for the aggregation of gold nanospheres due to DNA hybridization occur at 560 nm. The above computations have been performed on a 3.0GHz Dell-workstation.

Table 3.2 presents the comparison between FMM and conventional direct calculations for the particle configuration shown in Figure 3.16. Table II clearly reveals the efficiency of the fast multipole method, which is the method of choice for the large size problems.

Table 3.1: Comparison of the resonance wavelengths for three silver spherical nanoparticle system.

	Case 1	Case 2
Configuration	$r_{i,i+1}/r_i = 1/3,$	$r_{i,i+1}/r_i = 1/3$
	$r_{i,i+1}/r_i = 0.3,$	$r_{i,i+1}/r_i = 0.6$
Resonance wavelength [13]	369 nm	382 nm
Resonance wavelength (Computational)	372 nm	387 nm

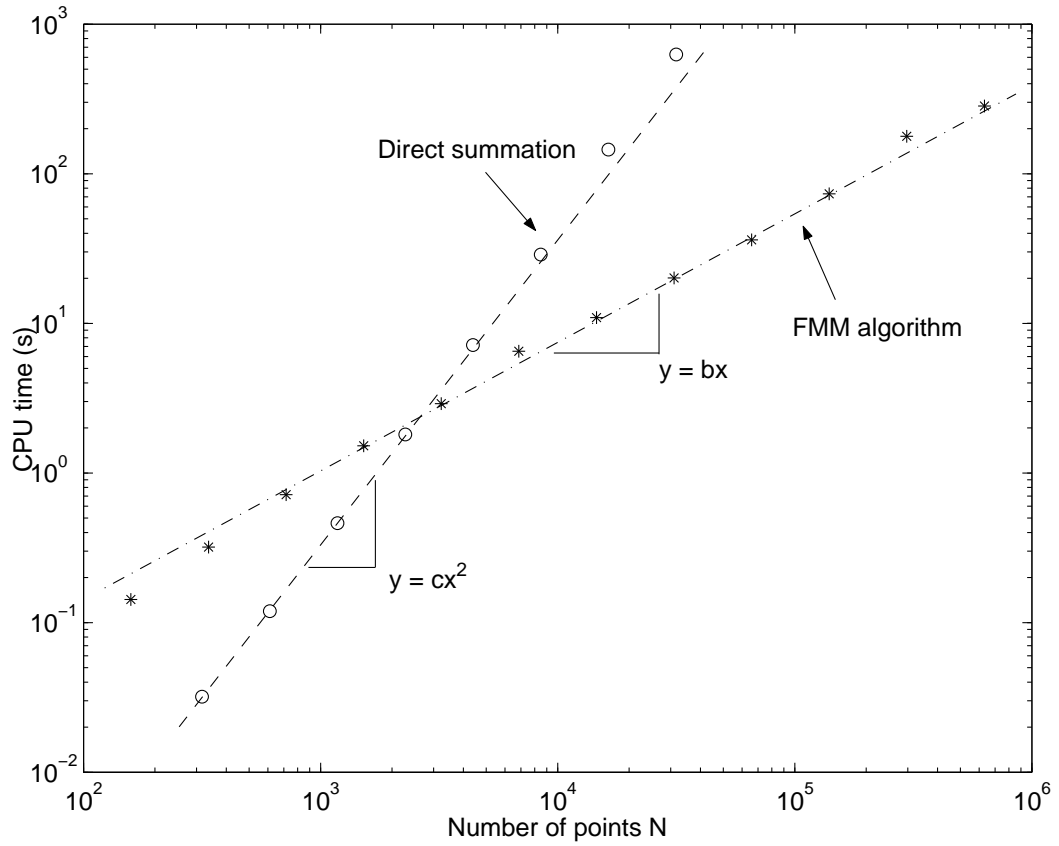


Figure 3.12: The CPU time in seconds required for computation of problems of size  $N$  using direct method and FMM. FMM computations using truncation number  $p = 5$ . Computation is performed on Dell workstation with Pentium 3.0 GHz processor, 4.0 GB RAM.

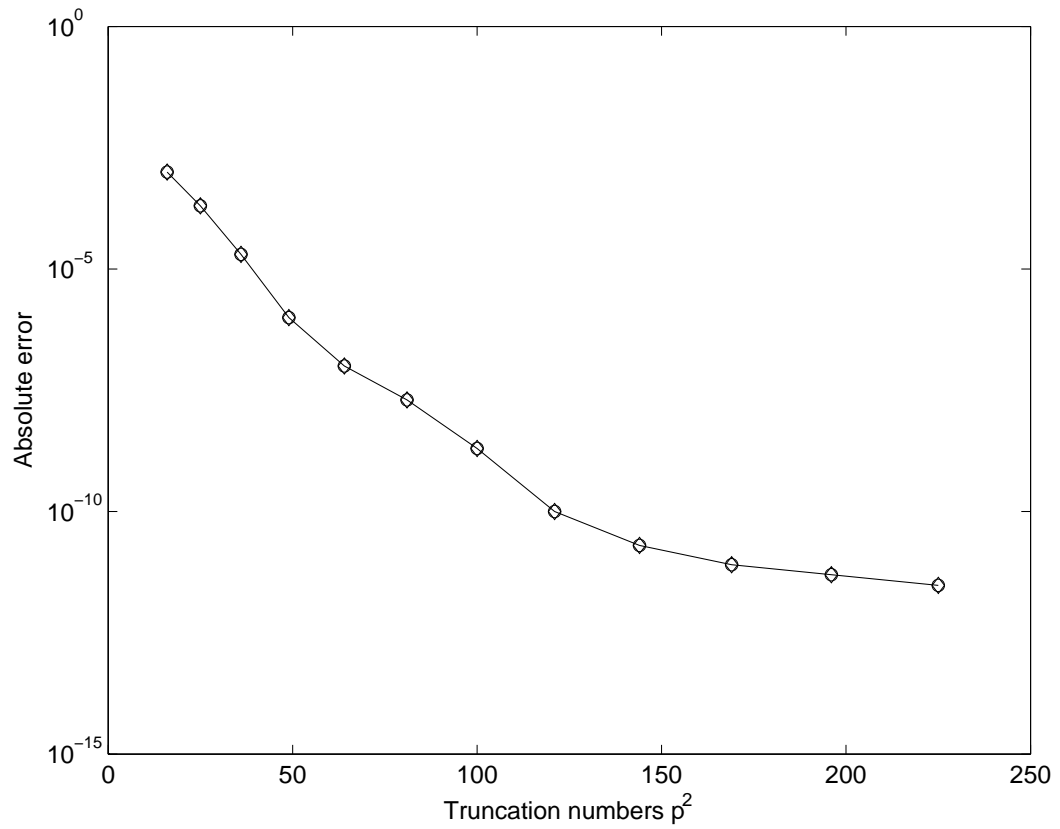


Figure 3.13: Absolute error vs truncation numbers  $p^2$  for the case  $N = 14496$ . Computation is performed on Dell workstation with Pentium 3.0 GHz processor, 4.0 GB RAM.

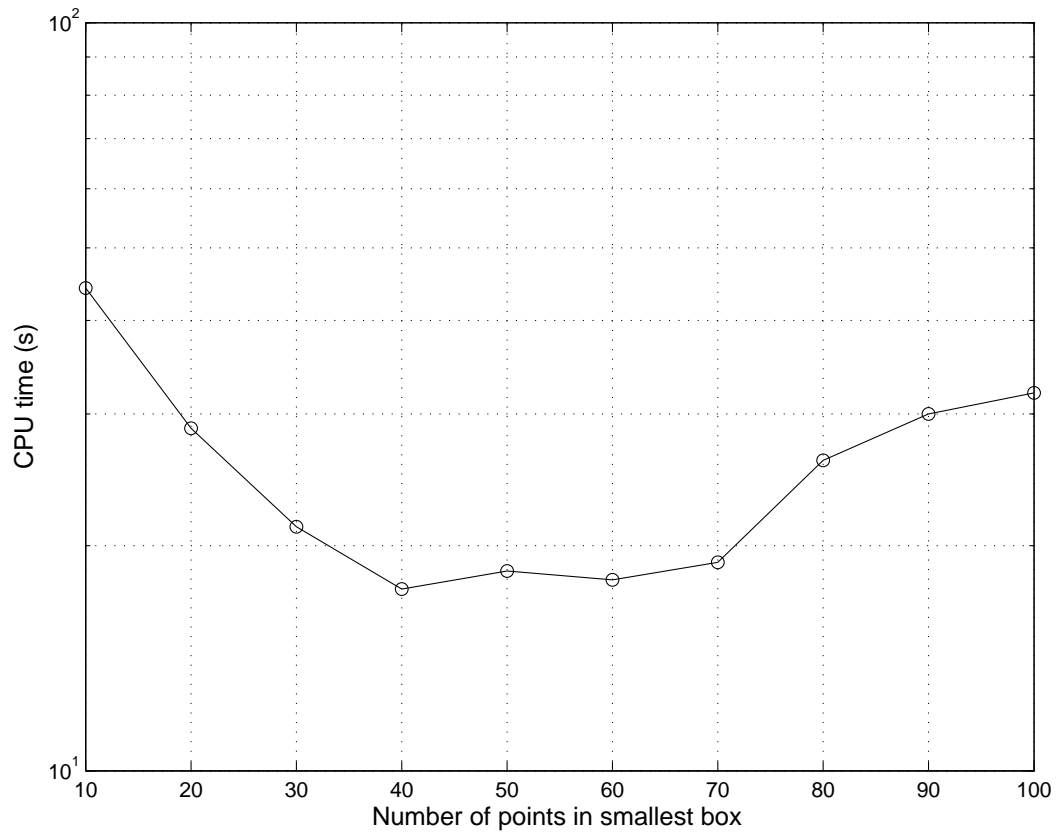


Figure 3.14: CPU times vs group parameters  $s$  (number of points in the smallest box) for  $N = 14496$ . Computation is performed on Dell workstation with Pentium 3.0 GHz processor, 4.0 GB RAM.

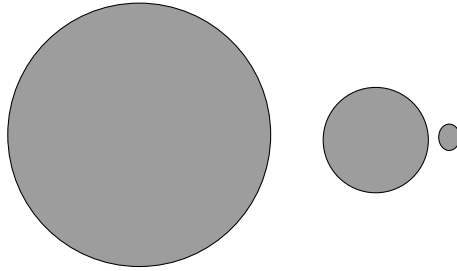


Figure 3.15: Three-sphere system for the nano-lens proposed in [83].

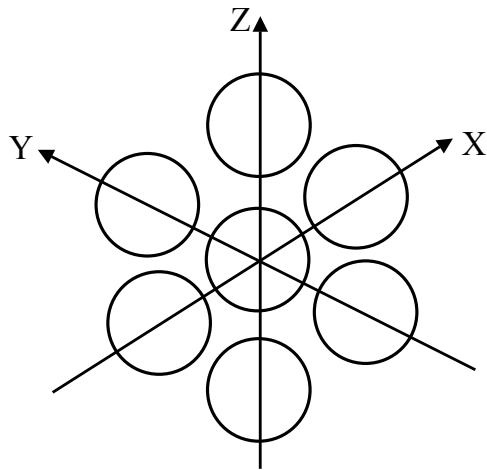


Figure 3.16: The schematic of a 7-sphere cluster.



Table 3.2: Computation times in seconds.

Method/mesh	8690	33600	134400
FMM	26	118	680
Direct summation	315	14819	237920*

\*This computation time is estimated by extrapolation.

### 3.5 Multipole expansion method for spherical nanoparticles

In this section, a meshless method for the analysis of plasmon resonances in multiple spherical nanoparticles is presented. It is shown that for spherical nanoparticles, the eigenvalue problem defined by (2.23) can be analytically simplified. For the case of coaxial spheres, the problem is appreciably simplified due to its symmetry. Numerical results and computational efficiency are presented and compared with boundary element techniques.

#### 3.5.1 The dual formulation for multiple spheres

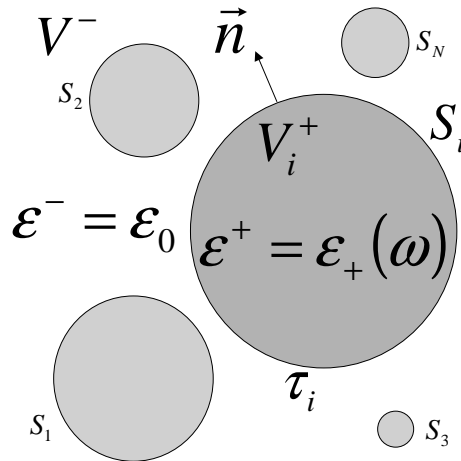


Figure 3.17: Multiple spherical nanoparticles located in proximity.

Consider  $N$  spherical nanoparticles located in proximity to one another with the same permittivity  $\epsilon_+(\omega)$  (Fig. 3.17). The source-free electric displacement  $\mathbf{D}$  satisfies everywhere

$$\nabla \times \mathbf{D} = 0, \quad (3.55)$$

$$\nabla \cdot \mathbf{D} = 0, \quad (3.56)$$

Then a scalar potential  $\Phi$  can be introduced

$$\mathbf{D} = -\nabla\Phi, \quad (3.57)$$

such that  $\Phi$  is a solution to the Laplace equation

$$\nabla^2\Phi = 0, \quad (3.58)$$

inside ( $V^+ = V_1^+ \cup \dots \cup V_N^+$ ) and outside ( $V^-$ ) of the union of the nanoparticles subject to the following interface boundary conditions on  $S$ , where  $S = S_1 \cup \dots \cup S_N$ :

$$\frac{\Phi^+}{\epsilon^+(\omega)} = \frac{\Phi^-}{\epsilon_0}, \quad (3.59)$$

$$\frac{\partial\Phi^+}{\partial n} = \frac{\partial\Phi^-}{\partial n}, \quad (3.60)$$

as well as the condition at infinity

$$\Phi(\infty) = 0. \quad (3.61)$$

The potential of this sourceless field can be represented as a potential of double layer of electric charges  $\tau(\mathbf{x})$  distributed over  $S$ :

$$\Phi(\mathbf{y}) = \frac{1}{4\pi\epsilon_0} \sum_{j=1}^N \oint_S \frac{\tau(\mathbf{x})}{|\mathbf{x} - \mathbf{y}|} dS_x, \quad (3.62)$$

where  $\mathbf{y}$  and  $\mathbf{x}$  are points on surface  $S$ . In other words, a double layer of electric charges  $\tau(\mathbf{x})$  distributed on  $S$  may create the same electric displacement in the free space as the resonant source-free electric displacement that may exist in the presence of the nanoparticles. This will be the case if the potential (3.62) satisfies all the conditions of boundary value problem (3.58)–(3.61). It is apparent that the potential (3.62) of the surface charges  $\tau(\mathbf{x})$  satisfies the Laplace equation in  $V^+$  and  $V^-$ , decays to zero at infinity and is continuous across  $S$ . To satisfy the boundary condition (3.60), we recall that the normal derivatives of a single layer potential are given by the formulas[70, 71]:

$$\frac{\partial\Phi^\pm}{\partial n}(\mathbf{y}) = \pm\frac{\tau(\mathbf{y})}{2\epsilon_0} + \frac{1}{4\pi\epsilon_0} \oint_S \tau(\mathbf{x}) \frac{(\mathbf{x} - \mathbf{y}) \cdot \mathbf{n}_x}{|\mathbf{x} - \mathbf{y}|^3} dS_x. \quad (3.63)$$

where  $\mathbf{n}_x$  is the outward normal at point  $\mathbf{x}$ . By substituting (3.9) into the boundary condition (3.60), we arrive at the homogeneous boundary integral equation:

$$\tau^{(i)}(\mathbf{y}) = \frac{\lambda}{2\pi} \sum_{j=1}^N \oint_{S_j} \tau^{(j)}(\mathbf{x}) \frac{(\mathbf{y} - \mathbf{x}) \cdot \mathbf{n}_x}{|\mathbf{y} - \mathbf{x}|^3} dS_x, \quad (3.64)$$

where

$$\lambda = \frac{\epsilon_+(\omega) - \epsilon_0}{\epsilon_+(\omega) + \epsilon_0}. \quad (3.65)$$

### 3.5.2 Multipole expansion method

It is natural to apply the standard boundary element method to solve the integral equation (3.64). For multiple spherical nanoparticles, however, a semi-analytical method can be developed to simplify the problem which provides much less complexity and computational costs in comparison with BEM. The main idea

of the approach can be stated as follows. Since the unknown functions  $\tau$  in equation (3.64) are defined on the surfaces of the spheres, they can be represented by spherical harmonics expansions. On the other hand, the kernel of the integral equation is  $1/r$ -type, so it can be also expanded in terms of spherical harmonics via addition theorem. Then by applying the orthogonality relations for spherical harmonics the integrals can be evaluated analytically. If the “integration” point  $\mathbf{x}$  and “evaluation” point  $\mathbf{y}$  are located on the same sphere, the spherical harmonics expansions possess the same basis and the corresponding integrals can be evaluated directly. If the “integration” point  $\mathbf{x}$  and “evaluation” point  $\mathbf{y}$  are located on different spheres, the translation formulas for spherical harmonics have to be applied to move the expansion center of “integration” sphere to the “evaluation” sphere such that they have the same basis function. Finally, the linear equation for expansion coefficients can be obtained.

We assume that the total dimension of the system is appreciably less than light wavelength (i.e., in quasi-static regime). The unknown surface function  $\tau(\mathbf{z})$  can be expanded into spherical harmonics

$$\tau^{(i)}(\mathbf{z}) = \sum_{l=0}^{\infty} \sum_{m=-l}^l \alpha_{lm}^{(i)} Y_{lm}(\widehat{\mathbf{z} - \mathbf{c}_i}), \quad (3.66)$$

where  $\alpha_{lm}^{(i)}$  are the expansion coefficients,  $l = 0, 1, 2, \dots, m = -l, \dots, l$ ,  $\mathbf{z}$  is an arbitrary point on the surface  $S_i$ ,  $\mathbf{c}_i$  is the center of  $S_i$ , and  $\widehat{\mathbf{z} - \mathbf{c}_i}$  is a unit vector defined as  $\frac{\mathbf{z} - \mathbf{c}_i}{|\mathbf{z} - \mathbf{c}_i|}$ .

If the “evaluation” point  $\mathbf{y}$  and “integration” point  $\mathbf{x}$  are located on the same sphere  $S_i$  which is the case for the  $i$ th term of the right hand side of integral equation

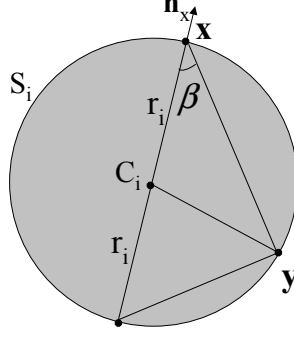


Figure 3.18: Points  $\mathbf{x}$  and  $\mathbf{y}$  are located at same sphere.

(3.64), the integral can be simplified as follows. From Fig. 3.18, it is easy to see that:

$$\frac{(\mathbf{x} - \mathbf{y}) \cdot \mathbf{n}_x}{|\mathbf{x} - \mathbf{y}|^2} = \frac{\cos \beta}{|\mathbf{x} - \mathbf{y}|} = \frac{1}{2r_i}, \quad (3.67)$$

Using formulas (3.66) and (3.67), The  $i$ th term mentioned above can be written as:

$$\oint_{S_i} \tau^{(i)}(\mathbf{x}) \frac{(\mathbf{y} - \mathbf{x}) \cdot \mathbf{n}_x}{|\mathbf{y} - \mathbf{x}|^3} dS_x = \frac{1}{2r_i} \sum_{l=0}^{\infty} \sum_{m=-l}^l \alpha_{lm}^{(i)} \oint_{S_i} \frac{Y_{lm}(\widehat{\mathbf{x} - \mathbf{c}_i})}{|\mathbf{y} - \mathbf{x}|} dS_x, \quad (3.68)$$

By applying the addition theorem, the term  $\frac{1}{|\mathbf{y} - \mathbf{x}|}$  can be expanded into spherical harmonics with center  $\mathbf{c}_i$ ,

$$\oint_{S_i} \frac{Y_{lm}(\widehat{\mathbf{x} - \mathbf{c}_i})}{|\mathbf{y} - \mathbf{x}|} dS_x = \sum_{l'=0}^{\infty} \sum_{m'=-l'}^{l'} \frac{4\pi}{2l' + 1} \oint_{S_i} Y_{lm}(\widehat{\mathbf{x} - \mathbf{c}_i}) Y_{l'm'}^*(\widehat{\mathbf{x} - \mathbf{c}_i}) \frac{Y_{lm}(\widehat{\mathbf{y} - \mathbf{c}_i})}{r_i} r_i^2 \sin \theta d\theta d\phi. \quad (3.69)$$

According to the orthogonality relations for spherical harmonics,

$$\int_0^{2\pi} d\phi \int_0^{\pi} \sin \theta d\theta Y_{l'm'}^*(\theta, \varphi) Y_{lm}(\theta, \varphi) = \delta_{l'l} \delta_{m'm}, \quad (3.70)$$

and obtain the final result for the  $i$ th term:

$$\oint_{S_i} \tau^{(i)}(\mathbf{x}) \frac{(\mathbf{y} - \mathbf{x}) \cdot \mathbf{n}_x}{|\mathbf{y} - \mathbf{x}|^3} dS_x = 2\pi \sum_{l=0}^{\infty} \sum_{m=-l}^l \alpha_{lm}^{(i)} \frac{Y_{lm}(\widehat{\mathbf{y} - \mathbf{c}_i})}{2l + 1}, \quad (3.71)$$

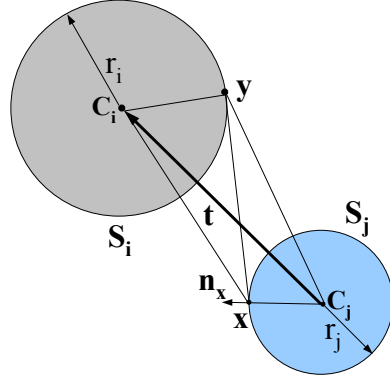


Figure 3.19: Points  $\mathbf{x}$  and  $\mathbf{y}$  are located at different spheres.

If the “evaluation” point  $\mathbf{y}$  and “integration” point  $\mathbf{x}$  are located on the different sphere  $S_i$  and  $S_j$ , the integral can be simplified as follows. Recall  $(\nabla\psi) \cdot \mathbf{n} = \frac{\partial\psi}{\partial n}$  and use formula (3.66), The  $j$ th term of the right hand side of integral equation (3.64) becomes

$$\oint_{s_j} \tau^{(j)}(\mathbf{x}) \frac{(\mathbf{y} - \mathbf{x}) \cdot \mathbf{n}_x}{|\mathbf{y} - \mathbf{x}|^3} dS_x = - \oint_{s_i} \left[ \sum_{l=0}^{\infty} \sum_{m=-l}^l \alpha_{lm}^{(j)} Y_{lm}(\widehat{\mathbf{x} - \mathbf{c}_j}) \right] \frac{\partial}{\partial n_x} \left( \frac{1}{|\mathbf{y} - \mathbf{x}|} \right) dS_x, \quad (3.72)$$

By using the addition theorem and  $\frac{\partial}{\partial n_x} = \frac{\partial}{\partial r_j}$ , we get

$$\begin{aligned} \frac{\partial}{\partial n_x} \left( \frac{1}{|\mathbf{y} - \mathbf{x}|} \right) &= \sum_{l'=0}^{\infty} \sum_{m'=-l'}^{l'} \frac{4\pi}{2l'+1} \frac{\partial}{\partial r_j} \left( \frac{|\mathbf{x} - \mathbf{c}_j|^{l'}}{|\mathbf{y} - \mathbf{c}_j|^{l'+1}} \right) Y_{l'm'}^*(\widehat{\mathbf{x} - \mathbf{c}_j}) Y_{l'm'}(\widehat{\mathbf{y} - \mathbf{c}_j}) \\ &= \sum_{l'=0}^{\infty} \sum_{m'=-l'}^{l'} \frac{4\pi l' r_j^{l'-1}}{2l'+1} \frac{Y_{l'm'}(\widehat{\mathbf{y} - \mathbf{c}_j})}{|\mathbf{y} - \mathbf{c}_j|^{l'+1}} Y_{l'm'}^*(\widehat{\mathbf{x} - \mathbf{c}_j}), \end{aligned} \quad (3.73)$$

Then according to the orthogonality relations for spherical harmonics, the integral

in (3.19) can be evaluated as

$$\oint_{S_j} \tau^{(j)}(\mathbf{x}) \frac{(\mathbf{y} - \mathbf{x}) \cdot \mathbf{n}_x}{|\mathbf{y} - \mathbf{x}|^3} dS_x = -4\pi \sum_{l=0}^{\infty} \sum_{m=-l}^l \alpha_{lm}^{(j)} \frac{lr_j^{l+1}}{2l+1} \left( \frac{Y_{lm}(\widehat{\mathbf{y} - \mathbf{c}_j})}{|\mathbf{y} - \mathbf{c}_j|^{l+1}} \right). \quad (3.74)$$

In order to have the same basis functions on both sides of equation (3.64), we translate the expansions from the center of “integration” sphere  $S_j$  to the center of “observation” sphere  $S_i$ . The re-expansion coefficients  $\gamma_{l'm'}^{(j)}$  can be related to the original expansion coefficients  $\alpha_{lm}^{(j)}$  by using the “multipole-to-local” translation operator and expressed in the following form

$$\gamma_{l'm'}^j = \sum_{l=0}^{\infty} \sum_{m=-l}^l \frac{i^{|m'-m|-|m'|-|m|} A_l^m A_{l'}^{m'} Y_{l'+l}^{m-m'}(\widehat{\mathbf{t}}) lr_j^{l+1} r_i^l}{(-1)^l A_{l'+l}^{m-m'}} \frac{lr_j^{l+1} r_i^l}{|\mathbf{t}|^{l'+l+1}} \frac{1}{2l+1} \alpha_{lm}^{(j)}, \quad (3.75)$$

where vector  $\mathbf{t}$  is defined in Fig. 3.19 and  $A_l^m$  is given by (3.16). To keep things simpler, denote

$$\gamma_{l'm'}^j = K_{l'm',lm}^{(j)} \alpha_{lm}^{(j)}, \quad (3.76)$$

where  $K_{l'm',lm}^{(j)}$  is the operator to perform the translation in equation (3.75). By using this translation operator, equation (3.74) becomes:

$$\oint_{S_j} \tau_j(\mathbf{x}) \frac{(\mathbf{y} - \mathbf{x}) \cdot \mathbf{n}_x}{|\mathbf{y} - \mathbf{x}|^3} dS_x = -4\pi \sum_{l'=0}^{\infty} \sum_{m'=-l'}^{l'} K_{l'm',lm}^{(j)} \alpha_{lm}^{(j)} Y_{lm}(\widehat{\mathbf{y} - \mathbf{c}_i}). \quad (3.77)$$

By Substituting formulas (3.71) and (3.77) into (3.64) and equating the coefficients for same terms, we get

$$\left( \frac{1}{\lambda} - \frac{1}{2l+1} \right) \alpha_{lm}^{(i)} - \sum_{j=i, j \neq i}^N \alpha_{lm}^{(j)} K_{l'm',lm}^{(j)} = 0. \quad (3.78)$$

We can write above equation for each sphere, then we get the simplified eigenvalue problem:

$$AX = \beta X, \quad (3.79)$$

where

$$X = [\alpha_{lm}^{(1)}, \dots, \alpha_{lm}^{(i)}, \dots, \alpha_{lm}^{(N)}]^T, \quad (3.80)$$

$$\beta = \frac{1}{\lambda}, \quad (3.81)$$

$$A_{ji} = \begin{cases} \left[ \frac{1}{2l+1} \right], & j = i, \\ K_{l'm',lm}^{(j)}, & j \neq i, \end{cases} \quad (3.82)$$

where  $i, j = 1, 2, \dots, N$ . It should be noted that  $A_{ji}$  is a submatrix for  $A$ . When  $j = i$ , it is a diagonal matrix, and when  $j \neq i$ , it is a dense matrix determined by the translation operator.

In numerical simulations, the infinite series of spherical harmonic has to be truncated. If the truncation number is  $p$ , the total length of the series is  $p^2$ . For N-sphere system, the dimension for matrix  $A$  is  $Np^2$ , and

$$\tau_i(\mathbf{z}) \approx \sum_{l=0}^{p-1} \sum_{m=-1}^l \alpha_{lm}^{(i)} Y_{lm}(\mathbf{z} - \mathbf{c}_i). \quad (3.83)$$

The truncation number  $p$  is not only a function of the error but also affected by the geometric configuration. Smaller distances between spheres require a larger truncation number to keep the accuracy. This phenomenon is shown in Fig.5. In our simulation, we truncate as  $p \leq p_{max} = 5r_{max}/d_{min}$ , where  $r_{max}$  is the radius of the largest sphere in the system,  $d_{min}$  is the smallest gap between spheres. We have checked that the numerical error associated with such a truncation is negligible.

If all the centers of spheres stay along a line, this is the coaxial case. Due to the axial symmetry, the multipole to local translation operator can be decomposed



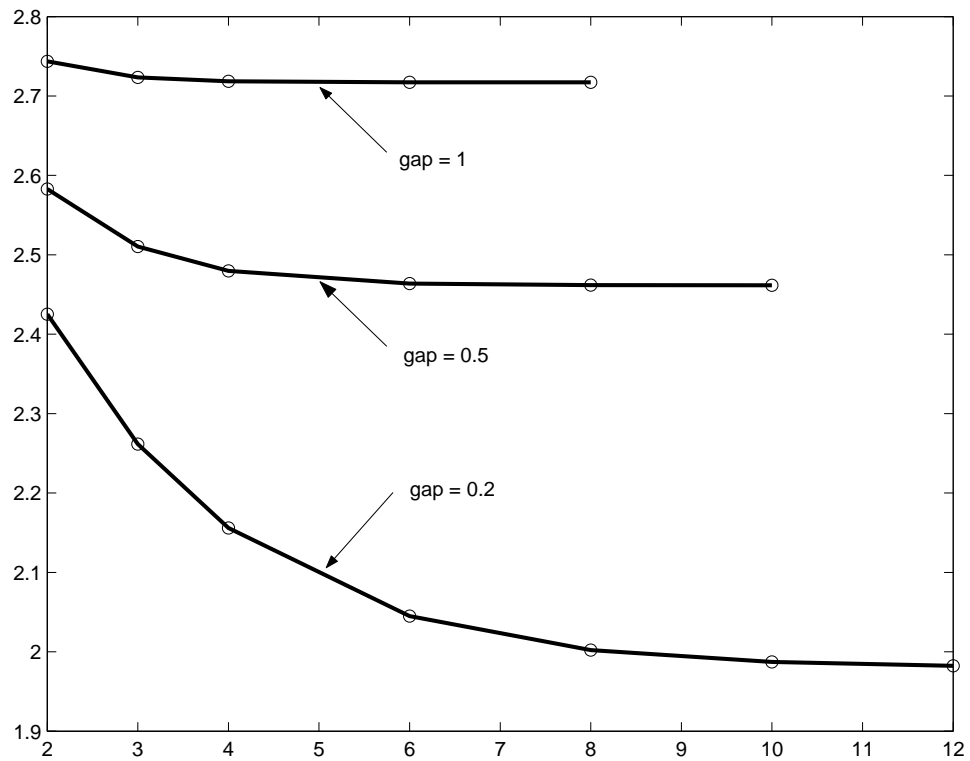


Figure 3.20: Truncation number as a function of the gap between two spheres.

Table 3.3: Computed eigenvalue for two spheres with truncation number  $p = 10$ .

Mode	Eigenvalue	Mode	Eigenvalue	Mode	Eigenvalue	Mode	Eigenvalue
1	2.6190	11	5.0276	21	6.9635	31	8.9070
2	2.8049	12	5.0742	22	7.0376	32	8.9330
3	2.8049	13	5.1823	23	7.1145	33	8.9330
4	3.2189	14	5.3208	24	7.1146	34	8.9845
5	3.2189	15	5.3209	25	7.1314	35	9.0198
6	3.4245	16	5.6506	26	7.1315	36	9.0199
7	4.7415	17	6.8485	27	7.1635	37	9.0391
8	4.7435	18	6.8837	28	7.3933	38	9.0594
9	4.7435	19	6.8837	29	7.3933	39	9.1431
10	4.9275	20	6.8931	30	7.6609	40	9.1433

and therefore the final matrix can be simplified. The operator can be expressed as following:

$$\left(\overline{S|R}\right)(\mathbf{t}) = T(m, n, l, k) \frac{P_{l+n}^{m-k}(\cos\alpha)e^{im\beta}}{\rho^{l+n+1}} \quad (3.84)$$

where  $m, n, l, k$  are indexes, and  $T$  is a known function of indexes.  $(\rho, \alpha, \beta)$  represents the translation vector  $\mathbf{t}$  in spherical coordinate. In the coaxial case, because  $\beta = 0$ , the elements for different  $m$  are decoupled, and the matrix of can be decomposed according to index  $m$ . For example, with truncation number  $p = 10$ , the size of the translation matrix is 100. If we solve the problem for the two-sphere system, the total size is 200. This matrix could be decomposed according to different  $m$  and solved separately where the size of largest submatrix is 20. The results are shown in Table 3.3 and Table 3.4.

Table 3.4: Computed eigenvalue for two spheres with truncation number  $p = 10$  using submatrix.

m=0	2.6190	3.4245	4.7415	5.6506	7.1145	7.6609	...
m=-1	2.8049	3.2189	4.7435	5.3208	7.0376	7.3933	...
m=1	2.8049	3.2189	4.7435	5.3209	6.9635	7.3933	...
m=-2			4.9275	5.0742	6.8931	7.1635	...
m=2			5.0274	5.1823	6.8837	7.1315	...
m=-3					6.8837	7.1314	...
m=3					6.8485	7.1145	...
...	...	...	...	...	...	...	...

### 3.5.3 Numerical results

The multipole expansion method has been numerically implemented and extensively tested. It has proved to be accurate and efficient. The results are illustrated by the examples presented below.

For single sphere, the results have been shown to be analytical and agree with classical Mie theory. For two-sphere system, it always coaxial and therefore can be further decomposed according to  $m$ . We computed the case with geometric parameters: radius of spheres  $r_1 = 1, r_2 = 0.5$ , the distance between the surfaces of the spheres  $d = 0.5$ . For the three-sphere system, we tested two different cases: one is coaxial with parameters:  $r_1 = 1, r_2 = 0.5, r_3 = 1, d_{12} = d_{21} = 0.5$ ; the other one, the three spheres are equal and form an equilateral triangle with  $r_1 = r_2 = r_3 = 1, d_{12} = d_{23} = d_{34} = 1$ . The results as well as the computation costs are compared with BEM results and shown in Table 3.5 and Table 3.6. The results of the two methods agree with each other very well and the multipole expansion method is obviously more efficient. In fact, this semi-analytical method also has

Table 3.5: Comparison of numerical results of BEM and MEM for two-nanosphere and three-nanosphere configurations.

two-sphere			three-sphere		
Mode	BEM	MEM	Mode	BEM	MEM
1	2.4959	2.5161	1	2.2659	2.3453
2	2.7378	2.7290	2	2.6681	2.6594
3	2.7379	2.7290	3	2.6681	2.6594
4	3.2600	3.3391	4	2.9028	2.9427
5	3.2603	3.3391	5	2.9028	2.9427
6	3.4666	3.5652	6	3.1300	3.1262

Table 3.6: Comparison of computation costs of BEM and MEM for two-nanosphere and three-nanosphere configurations.

Method	Number of sphere	matrix size	CPU time(s)
MEM	2	200	0.1
BEM	2	2560	3.8 (with ARPACK)
MEM	3	300	0.25
BEM	3	3840	8.7 (with ARPACK)

the advantage for assembly of the matrix, because it only requires to build up the translation matrix. Each non-diagonal submatrix has the same structure; it repeats only with different translation vectors.

## Chapter 4

### **Extinction Cross Sections of Nanoparticles**

In this chapter, the boundary integral equation technique (developed in chapter 2) is extended to the calculation of extinction cross sections (ECS) of nanoparticles. ECS is an important measure of optical properties of nanoparticles which reveals the strength and the sharpness of the plasmon resonance modes. The concept of ECS and the optical theorem are briefly reviewed in section 4.1. The computation algorithm of ECS as well as the numerical results are presented in sections 4.2 and 4.3. It is shown that the scattered field can be derived through the solution of an inhomogeneous integral equation, and the extinction cross section is then obtained by employing the optical theorem. Finally, the outline technique is modified to take into account the phase shift between adjacent nanoparticles for the analysis of nanoparticle-structured plasmonic waveguides of light in section 4.4.

## 4.1 What is the extinction cross section ?

### 4.1.1 Concept of extinction cross section

The extinction cross section (ECS) of a nanoparticle represents the total power loss from the incident wave due to the scattering and absorption by the nanoparticle. The ECS curve clearly reveals the plasmon resonances by peaks around resonance frequencies and it provides important information such as the strength and sharpness of the resonance. The mathematical definition of ECS can be briefly demonstrated as follows [85, 86].

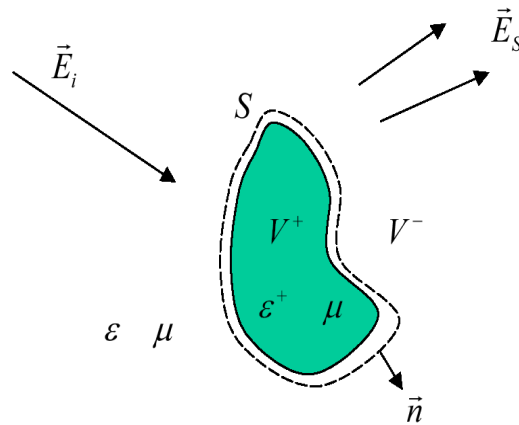


Figure 4.1: Scattering diagram of a nanoparticle.

Consider the scattering geometry in Figure 4.1, a plane wave incident on a scatterer with arbitrary shape. The field ( $\mathbf{E}^-$ ) at any point in the lossless medium with permittivity  $\epsilon$  and permeability  $\mu$  surrounding the scatterer may be represented

as the sum of the incident field ( $\mathbf{E}_i$ ) and scattered field ( $\mathbf{E}_s$ ).

$$\mathbf{E}^- = \mathbf{E}_i + \mathbf{E}_s, \quad (4.1)$$

$$\mathbf{H}^- = \mathbf{H}_i + \mathbf{H}_s. \quad (4.2)$$

Let the permittivity of the scatterer (nanoparticle) be complex valued with real and imaginary parts

$$\epsilon_+(\omega) = \epsilon'_+(\omega) + i\epsilon''_+(\omega). \quad (4.3)$$

The electromagnetic fields inside the particle ( $V^+$ ) obey the equations:

$$\nabla \times \mathbf{E}^+ = j\omega\mu\mathbf{H}^+, \quad (4.4)$$

$$\nabla \times \mathbf{H}^+ = -j\omega\epsilon^+\mathbf{E}^+, \quad (4.5)$$

and are subject to the following boundary conditions:

$$\mathbf{n} \times \mathbf{E}^+ = \mathbf{n} \times (\mathbf{E}_i + \mathbf{E}_s), \quad (4.6)$$

$$\mathbf{n} \times \mathbf{H}^+ = \mathbf{n} \times (\mathbf{H}_i + \mathbf{H}_s). \quad (4.7)$$

The time-averaged power absorbed by the nanoparticle is

$$W_a = \frac{1}{2} \int_{V^+} \omega\epsilon''_+ |\mathbf{E}^+|^2 dV. \quad (4.8)$$

It is easy to show that:

$$\nabla \cdot (\mathbf{E}^+ \times \mathbf{H}^{+*}) = \mathbf{H}^{+*} \cdot \nabla \times \mathbf{E}^+ - \mathbf{E}^+ \cdot \nabla \times \mathbf{H}^{+*} = j\omega\mu |\mathbf{H}^+|^2 - j\omega\epsilon_+^* |\mathbf{E}^+|^2, \quad (4.9)$$

and taking the real part of (4.9) gives:

$$\nabla \cdot [\mathbf{Re}(\mathbf{E}^+ \times \mathbf{H}^{+*})] = -\omega\epsilon''_+ |\mathbf{E}^+|^2. \quad (4.10)$$

Therefore the absorbed power by the nanoparticle can be expressed as:

$$W_a = -\frac{1}{2} \int_{V^+} \nabla \cdot [\mathbf{Re}(\mathbf{E}^+ \times \mathbf{H}^{+*})] dV = -\frac{1}{2} \int_S \mathbf{n} \cdot \mathbf{Re}(\mathbf{E}^+ \times \mathbf{H}^{+*}) dS. \quad (4.11)$$

Substitute boundary conditions (4.6) and (4.7) into formula (4.11), it is easy to see that:

$$W_a = -\frac{1}{2} \int_S \mathbf{n} \cdot \mathbf{Re}[(\mathbf{E}_i + \mathbf{E}_s) \times (\mathbf{H}_i^* + \mathbf{H}_s^*)] dS = -\int_S \mathbf{n} \cdot (\mathbf{S}_i + \mathbf{S}' + \mathbf{S}_s) dS, \quad (4.12)$$

where  $\mathbf{S}_i, \mathbf{S}', \mathbf{S}_s$  are defined as:

$$\mathbf{S}_i = \frac{1}{2} Re(\mathbf{E}_i \times \mathbf{H}_i^*), \quad (4.13)$$

$$\mathbf{S}' = \frac{1}{2} Re[(\mathbf{E}_i \times \mathbf{H}_s^*) + (\mathbf{E}_s \times \mathbf{H}_i^*)], \quad (4.14)$$

$$\mathbf{S}_s = \frac{1}{2} Re(\mathbf{E}_s \times \mathbf{H}_s^*). \quad (4.15)$$

Since  $\nabla \cdot \mathbf{S}_i = 0$  is true everywhere in  $V^+$  and  $V^-$ , the incident power  $S_i$  should satisfy

$$\int_S \mathbf{n} \cdot \mathbf{S}_i dS = 0, \quad (4.16)$$

and because there is no source between boundary  $S$  and infinity, the scattered power can be evaluated as an integral over  $S$ :

$$W_s = \int_S \mathbf{n} \cdot \mathbf{S}_s dS. \quad (4.17)$$

Then the absorbed power now can be written in the following form:

$$W_a = -\int_S \mathbf{n} \cdot \mathbf{S}' dS - W_s, \quad (4.18)$$

and the total power loss due to the scatterer (scattering and absorption) is:

$$W_{ext} = W_a + W_s = -\int_S \mathbf{n} \cdot \mathbf{S}' dS. \quad (4.19)$$



Thus the extinction cross section (ECS) is defined as the ratio of total power  $W_{ext}$  to the incident power per unit area:

$$\sigma_{ext} = \frac{W_{ext}}{I_i}, \quad (4.20)$$

where  $I_i$  is the incident radiation. Similarly, we can define the scattering cross section (SCS) and the absorption cross section (ACS):

$$\sigma_{sca} = \frac{W_s}{I_i}, \quad (4.21)$$

$$\sigma_{abs} = \frac{W_a}{I_i}, \quad (4.22)$$

and it is apparent:

$$\sigma_{ext} = \sigma_{sca} + \sigma_{abs}. \quad (4.23)$$

It is instrumental to point out that for small metallic particles, the losses of incident radiation is dominated by absorption, so the above express can be written as:

$$\sigma_{ext} \approx \sigma_{abs}. \quad (4.24)$$

### 4.1.2 The optical theorem

The above definition can be used to compute the ECS of a nanoparticle. Another convenient way, however, is to employ the so-called *optical theorem*. The optical theorem expresses a very curious fact: *the extinction depends only on the scattering amplitude in the forward direction*. The proof of this theorem can be found in [39, 87] and will be omitted here. In the following, only those key formulas are summarized for the calculation of ECS by using the optical theorem.

Let the incident wave be linearly polarized with polarization vector  $\hat{\mathbf{e}}_i$ :

$$\mathbf{E}_i = \hat{\mathbf{e}}_i E_0 e^{i\mathbf{k}_i \cdot \mathbf{r}}, \quad (4.25)$$

$$\mathbf{H}_i = (\hat{\mathbf{k}}_i \times \hat{\mathbf{e}}_i) \frac{E_0}{\eta} e^{i\mathbf{k}_i \cdot \mathbf{r}}, \quad (4.26)$$

$$\mathbf{B}_i = \frac{1}{ck} \hat{\mathbf{k}}_i \times \mathbf{E}_i. \quad (4.27)$$

The far field can be related to the scattering amplitude  $\mathbf{F}(\hat{\mathbf{k}}_s, \hat{\mathbf{k}}_i)$  as:

$$\mathbf{F}(\hat{\mathbf{k}}_s, \hat{\mathbf{k}}_i) = \lim_{r \rightarrow \infty} \left( \frac{e^{ikr}}{r} \right)^{-1} \mathbf{E}_s(\mathbf{r}), \quad (4.28)$$

where  $\mathbf{k}_i$  is the incident wave vector,  $\mathbf{k}_s$  is the scattering wave vector in the direction of observation,  $\mathbf{E}_s$  is the scattered field in far-field zone. Then the optical theorem tells us:

$$\sigma_{ext} = \frac{4\pi}{k} \text{Im} \left[ \hat{\mathbf{e}}_i^* \cdot \mathbf{f}(\hat{\mathbf{k}}_i, \hat{\mathbf{k}}_i) \right], \quad (4.29)$$

where  $k$  is the wave number,  $\mathbf{f}(\hat{\mathbf{k}}_s, \hat{\mathbf{k}}_i)$  is the normalized forward direction scattering amplitude and the normalized scattering amplitude is defined as:

$$\mathbf{f}(\hat{\mathbf{k}}_s, \hat{\mathbf{k}}_i) = \frac{\mathbf{F}(\hat{\mathbf{k}}_s, \hat{\mathbf{k}}_i)}{E_0}. \quad (4.30)$$

According to (4.28)–(4.30), the entire problem of the computation of ECS is reduced to the evaluation of the forward scattering amplitude  $\mathbf{F}$ , which is related to the scattered far field  $\mathbf{E}_s$ .

### 4.1.3 Measurement of ECS

In practice, the ECS can be directly measured (see Fig.2) in terms of the following expression [39]:

$$U = I_i [A(D) - \sigma_{ext}], \quad (4.31)$$

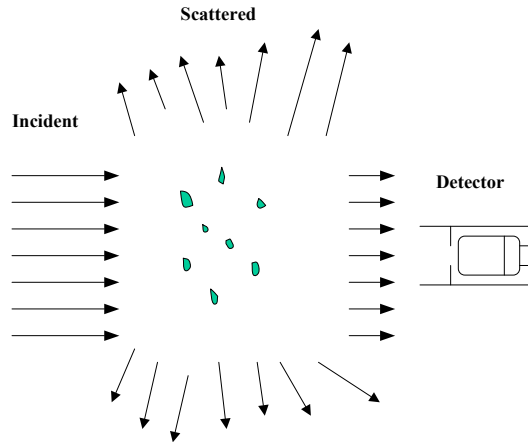


Figure 4.2: Schematic illustration for the measurement of extinction cross sections.

where  $I_i$  is the incident radiation,  $A(D)$  is the area of the detector and  $U$  is the power incident on the detector. We measure  $U$  with and without the particle interposed between source and detector. Because  $\sigma_{ext}$  is inherently positive, the effect of the particle is to reduce the detector area by  $\sigma_{ext}$ . This method of measurement illustrates the interpretation of  $\sigma_{ext}$  as an area.

## 4.2 Computation of ECS

### 4.2.1 Near field computation

Consider an incident plane wave scattered by nanoparticle of arbitrary shape with permittivity  $\epsilon_+(\omega)$  (Fig. 4.1). We shall start with Maxwell's equations written in the mathematical form that explicitly reflects the smallness of particle dimensions in comparison with the free-space wavelength. For this reason, we introduce the

scaled vectors of scattered and incident fields

$$\mathbf{e} = \epsilon_0^{\frac{1}{2}} \mathbf{E}, \quad \mathbf{h} = \mu_0^{\frac{1}{2}} \mathbf{H}, \quad \mathbf{e}_{in} = \epsilon_0^{\frac{1}{2}} \mathbf{E}_{in} \quad (4.32)$$

as well as spatial coordinate scaled by the diameter  $d$  of the object. This leads to the following boundary value problem for scattered fields  $\mathbf{e}^\pm$  and  $\mathbf{h}^\pm$ :

$$\nabla \times \mathbf{e}^+ = -j\beta \mathbf{h}^+, \quad \nabla \times \mathbf{h}^+ = j\beta \frac{\epsilon_+}{\epsilon_0} \mathbf{e}^+ + j\beta \left( \frac{\epsilon_+}{\epsilon_0} - 1 \right) \mathbf{e}_{in}^+, \quad (4.33)$$

$$\nabla \cdot \mathbf{e}^+ = 0, \quad \nabla \cdot \mathbf{h}^+ = 0, \quad (4.34)$$

$$\nabla \times \mathbf{e}^- = -j\beta \mathbf{h}^-, \quad \nabla \times \mathbf{h}^- = j\beta \mathbf{e}^-, \quad (4.35)$$

$$\nabla \cdot \mathbf{e}^- = 0, \quad \nabla \cdot \mathbf{h}^- = 0 \quad (4.36)$$

$$\mathbf{n} \times (\mathbf{e}^+ - \mathbf{e}^-) = 0, \quad \mathbf{n} \times (\mathbf{h}^+ - \mathbf{h}^-) = 0, \quad (4.37)$$

$$\mathbf{n} \cdot (\epsilon_+ \mathbf{e}^+ - \epsilon_0 \mathbf{e}^-) = (\epsilon_0 - \epsilon_+) \mathbf{n} \cdot \mathbf{e}_{in}^+, \quad \mathbf{n} \cdot (\mathbf{h}^+ - \mathbf{h}^-) = 0, \quad (4.38)$$

where superscripts “+” and “-” are used for physical quantities inside ( $V^+$ ) and outside ( $V^-$ ) the dielectric object, respectively,  $\mathbf{n}$  is a outward unit normal to  $S$ , while

$$\beta = \omega \sqrt{\mu_0 \epsilon_0} d. \quad (4.39)$$

In the case when the free-space wavelength is large in comparison with nanoparticle dimension,  $\beta$  can be treated as a small parameter and solution of the boundary value problem (4.33)-(4.38) can be expanded in terms of  $\beta$

$$\mathbf{e}^\pm = \mathbf{e}_0^\pm + \beta \mathbf{e}_1^\pm + \beta^2 \mathbf{e}_2^\pm + \dots, \quad (4.40)$$

$$\mathbf{h}^\pm = \mathbf{h}_0^\pm + \beta \mathbf{h}_1^\pm + \beta^2 \mathbf{h}_2^\pm + \dots. \quad (4.41)$$

An incident field is usually treated as independent of the characteristic dimension of the system under consideration. For this reason, it can be regarded as independent of  $\beta$ . By substituting formulas (4.40)–(4.41) into equations (4.33)–(4.36) as well as boundary conditions (4.37)–(4.38) and equating terms of equal powers of  $\beta$ , we obtain the boundary value problems for  $\mathbf{e}_k^\pm$  and  $\mathbf{h}_k^\pm$  ( $k = 0, 1, 2, \dots$ ).

For zero-order terms, these boundary value problems can be written in terms of  $\mathbf{E}_0^\pm = \epsilon_0^{-\frac{1}{2}} \mathbf{e}_0^\pm$  and  $\mathbf{H}_0^\pm = \mu_0^{-\frac{1}{2}} \mathbf{h}_0^\pm$  as follows:

$$\nabla \times \mathbf{E}_0^\pm = 0, \quad \nabla \cdot \mathbf{E}_0^\pm = 0, \quad (4.42)$$

$$\mathbf{n} \times (\mathbf{E}_0^+ - \mathbf{E}_0^-) = 0, \quad \mathbf{n} \cdot (\epsilon_+ \mathbf{E}_0^+ - \epsilon_0 \mathbf{E}_0^-) = (\epsilon_0 - \epsilon_+) \mathbf{n} \cdot \mathbf{E}_{in}^+, \quad (4.43)$$

and

$$\nabla \times \mathbf{H}_0^\pm = 0, \quad \nabla \cdot \mathbf{H}_0^\pm = 0, \quad (4.44)$$

$$\mathbf{n} \times (\mathbf{H}_0^+ - \mathbf{H}_0^-) = 0, \quad \mathbf{n} \cdot (\mathbf{H}_0^+ - \mathbf{H}_0^-) = 0. \quad (4.45)$$

From (4.44)–(4.45), it is apparent that

$$\mathbf{h}_0^\pm = 0. \quad (4.46)$$

The electric potential  $\varphi$  can be introduced for the electric field  $\mathbf{E}_0$  and this potential can be represented as an electric potential of a single layer of electric charge  $\sigma$  distributed over the boundary  $S$  of the particle. It is clear that the electric field of surface charges is curl and divergence free in  $V^+$  and  $V^-$  and satisfies the first boundary condition in (4.43). Next we recall the properties of single layer potential (2.20). By substituting (2.20) into the second boundary condition in (4.43), after

simple transformation we arrive at the following inhomogeneous boundary integral equation:

$$\sigma_0(Q) - \frac{\lambda}{2\pi} \oint_S \sigma_0(M) \frac{\mathbf{n}_Q \cdot \mathbf{r}_{MQ}}{r_{MQ}^3} dS_M = 2\epsilon_0 \lambda \mathbf{n}_Q \cdot \mathbf{e}_{in}^+(Q), \quad (4.47)$$

where

$$\lambda = \frac{\epsilon_+(\omega) - \epsilon_0}{\epsilon_+(\omega) + \epsilon_0}. \quad (4.48)$$

Thus, the scattered electric fields can be computed (in zero-order) as follows:

$$\mathbf{e}_0^\pm = -\nabla \varphi_0 = -\nabla \left[ \frac{1}{4\pi\epsilon_0} \oint_S \frac{\sigma_0(M)}{r_{MQ}} dS_M \right]. \quad (4.49)$$

The inhomogeneous boundary integral equation (4.47) for the calculations of electrostatic and scattering problem with negative  $\epsilon$  was extensively studied in publications of Mayergoyz [54, 55] and introduced for the analysis of plasmon resonance in [20]. From equations (4.33)–(4.38), (4.40)–(4.41) and (4.46), the boundary value problem for the first-order corrections can be derived and appears as the following:

$$\nabla \times \mathbf{e}_1^\pm = 0, \quad \nabla \cdot \mathbf{e}_1^\pm = 0, \quad (4.50)$$

$$\mathbf{n} \times (\mathbf{e}_1^+ - \mathbf{e}_1^-) = 0, \quad \mathbf{n} \cdot (\epsilon_+ \mathbf{e}_1^+ - \epsilon_0 \mathbf{e}_1^-) = 0, \quad (4.51)$$

$$\nabla \times \mathbf{h}_1^+ = j \frac{\epsilon^+}{\epsilon_0} \mathbf{e}_0^+ + j \left( \frac{\epsilon_+}{\epsilon_0} - 1 \right) \mathbf{e}_{in}^+, \quad \nabla \times \mathbf{h}_1^- = j \mathbf{e}_0^-, \quad \nabla \cdot \mathbf{h}_1^\pm = 0, \quad (4.52)$$

$$\mathbf{n} \times (\mathbf{h}_1^+ - \mathbf{h}_1^-) = 0, \quad \mathbf{n} \cdot (\mathbf{h}_1^+ - \mathbf{h}_1^-) = 0. \quad (4.53)$$

From equations (4.50)–(4.51), it is clear that

$$\mathbf{e}_1^\pm = 0. \quad (4.54)$$

Next, we proceed to the solution of boundary value problem (4.52)–(4.53). Terms  $j \frac{\epsilon^+}{\epsilon_0} \mathbf{e}_0^+ + j \left( \frac{\epsilon_+}{\epsilon_0} - 1 \right) \mathbf{e}_{in}^+$  and  $j \mathbf{e}_0^-$  in the first two equation of (4.52) can be interpreted

as current sources and the solution of boundary value problem (4.52)-(4.53) can be written in the integral form

$$\begin{aligned} \mathbf{h}_1^\pm(Q) &= \frac{j \frac{\epsilon^\pm}{\epsilon_0}}{4\pi} \int_{V^+} \frac{\mathbf{r}_{MQ}}{r_{MQ}^3} \times \mathbf{e}_0^+(M) dV_M + \frac{j}{4\pi} \int_{V^-} \frac{\mathbf{r}_{MQ}}{r_{MQ}^3} \times \mathbf{e}_0^-(M) dV_M \\ &+ \frac{j \left( \frac{\epsilon^\pm}{\epsilon_0} - 1 \right)}{4\pi} \int_{V^+} \frac{\mathbf{r}_{MQ}}{r_{MQ}^3} \times \mathbf{e}_{in}^+(M) dV_M. \end{aligned} \quad (4.55)$$

The last expression can be appreciably simplified and reduced to an integral over boundary  $S$ . Indeed, by using the fact that  $\nabla \times \mathbf{e}_0^\pm = 0$  and by employing the following formulas for vector analysis:

$$\nabla \times (g\mathbf{F}) = (\nabla g) \times \mathbf{F} + g(\nabla \times \mathbf{F}), \quad (4.56)$$

$$\int_V dV (\nabla \times \mathbf{A}) = \oint_S d\mathbf{S} \times \mathbf{A}, \quad (4.57)$$

after simple transformations we arrive at

$$\mathbf{h}_1^\pm(Q) = -\frac{j \left( \frac{\epsilon^\pm}{\epsilon_0} - 1 \right)}{4\pi} \left\{ \oint_S \frac{\mathbf{n}_M \times [\mathbf{e}_0^+(M) + \mathbf{e}_{in}^+(M)]}{r_{MQ}} dS_M \right\}. \quad (4.58)$$

Now we proceed to the discussion of second order terms in expansions of  $\mathbf{e}^+$  and  $\mathbf{h}^+$ . From equations (4.33)-(4.38), (4.40)-(4.41) and (4.54)-(4.55), the boundary value problem for the second-order terms  $\mathbf{e}_2^+$  and  $\mathbf{h}_2^+$  can be derived, respectively:

$$\nabla \times \mathbf{e}_2^\pm = -j\mathbf{h}_1^\pm, \quad \nabla \cdot \mathbf{e}_2^\pm = 0, \quad (4.59)$$

$$\mathbf{n} \cdot (\epsilon^+ \mathbf{e}_2^+ - \epsilon_0 \mathbf{e}_2^-) = 0, \quad \mathbf{n} \times (\mathbf{e}_2^+ - \mathbf{e}_2^-) = 0, \quad (4.60)$$

and

$$\nabla \times \mathbf{h}_2^\pm = 0, \quad \nabla \cdot \mathbf{h}_2^\pm = 0, \quad (4.61)$$

$$\mathbf{n} \cdot (\mathbf{h}_2^+ - \mathbf{h}_2^-) = 0, \quad \mathbf{n} \times (\mathbf{h}_2^+ - \mathbf{h}_2^-) = 0. \quad (4.62)$$

From formulas (4.61)–(4.62), it is apparent that

$$\mathbf{h}_2^\pm = 0. \quad (4.63)$$

In order to solve the boundary value problem (4.59)–(4.60), we shall split the electric field  $\mathbf{e}_2^\pm$  into two distinct components

$$\mathbf{e}_2^\pm = \tilde{\mathbf{e}}_2^\pm + \tilde{\tilde{\mathbf{e}}}_2^\pm, \quad (4.64)$$

that satisfy the following boundary value problems, respectively:

$$\nabla \times \tilde{\mathbf{e}}_2^\pm = -j\mathbf{h}_1^\pm, \quad \nabla \cdot \tilde{\mathbf{e}}_2^\pm = 0, \quad (4.65)$$

$$\mathbf{n} \cdot (\tilde{\mathbf{e}}_2^+ - \tilde{\mathbf{e}}_2^-) = 0, \quad \mathbf{n} \times (\tilde{\mathbf{e}}_2^+ - \tilde{\mathbf{e}}_2^-) = 0, \quad (4.66)$$

and

$$\nabla \times \tilde{\tilde{\mathbf{e}}}_2^\pm = 0, \quad \nabla \cdot \tilde{\tilde{\mathbf{e}}}_2^\pm = 0, \quad (4.67)$$

$$\mathbf{n} \cdot (\epsilon_+ \tilde{\tilde{\mathbf{e}}}_2^+ - \epsilon_0 \tilde{\tilde{\mathbf{e}}}_2^-) = (\epsilon_+ - \epsilon_0) \mathbf{n} \cdot \tilde{\mathbf{e}}_2^+, \quad \mathbf{n} \times (\tilde{\tilde{\mathbf{e}}}_2^+ - \tilde{\tilde{\mathbf{e}}}_2^-) = 0. \quad (4.68)$$

By using the same line of reasoning as in section 2.2, it can be shown that the solution of the boundary value problem (4.65)–(4.66) can be written as follows

$$\tilde{\mathbf{e}}_2^\pm = -\frac{(\epsilon_\pm - 1)}{8\pi} \oint_S \frac{\mathbf{n}_M \times [\mathbf{e}_0^+(M) + \mathbf{e}_{in}^+(M)] \times \mathbf{r}_{MQ}}{r_{MQ}} dS_M. \quad (4.69)$$

Next, we proceed to the solution of the boundary value problem (4.67)–(4.68).

Again, the single layer charge distribution can be introduced to construct the electric field  $\tilde{\tilde{\mathbf{e}}}_2^\pm$ . Then by using the same line of reasoning in the derivation of equation

(2.51), we obtain the following inhomogeneous integral equation for  $\sigma_2(M)$ :

$$\begin{aligned} \sigma_2(Q) & - \frac{\lambda}{2\pi} \oint_S \sigma_2(M) \frac{\mathbf{n}_Q \cdot \mathbf{r}_{MQ}}{r_{MQ}^3} dS_M \\ & = 2\epsilon_0\epsilon_+\lambda \frac{(\epsilon_\pm - 1)}{8\pi} \times \oint_S \frac{\mathbf{n}_Q \cdot [\mathbf{e}_0^+(M) + \mathbf{e}_{in}^+(M)] \times \mathbf{r}_{MQ}}{r_{MQ}} dS_M. \end{aligned} \quad (4.70)$$



Thus, the second-order term for scattered electric field  $\mathbf{e}_2^+$  can be written as:

$$\mathbf{e}_2^\pm = -\nabla \left[ \frac{1}{4\pi\epsilon_0} \oint \frac{\sigma_2(M)}{r_{MQ}} dS_M \right] - \frac{\left(\frac{\epsilon^+}{\epsilon_0} - 1\right)}{8\pi} \oint_S \frac{\mathbf{n}_M \times [\mathbf{e}_0^+(M) + \mathbf{e}_{in}^+(M)] \times \mathbf{r}_{MQ}}{r_{MQ}} dS_M. \quad (4.71)$$

Finally, the scattered near field is given by the formula

$$\mathbf{E}^+ \approx \epsilon_0^{-\frac{1}{2}} (\mathbf{e}_0^+ + \beta^2 \mathbf{e}_2^+). \quad (4.72)$$

## 4.2.2 Far field computation

As discussed in section 4.1, the key step to obtain ECS is the computation of scattered far fields. In the following, we demonstrate the technique to compute this quantity according to the obtained scattered near field. The far field is the solution of the following boundary value problem:

$$\nabla \times \mathbf{E}^\pm = -j\omega\mu_0 \mathbf{H}^\pm, \quad (4.73)$$

$$\nabla \times \mathbf{H}^+ = j\omega\epsilon_0 \mathbf{E}^+ + j\omega(\epsilon - \epsilon_0) (\mathbf{E}^+ + \mathbf{E}_{in}^+), \quad (4.74)$$

$$\nabla \times \mathbf{H}^- = j\omega\epsilon_0 \mathbf{E}^-, \quad (4.75)$$

$$\mathbf{n} \times (\mathbf{E}^+ - \mathbf{E}^-) = 0, \quad \mathbf{n} \times (\mathbf{H}^+ - \mathbf{H}^-) = 0, \quad (4.76)$$

where  $\mathbf{E}^\pm = \epsilon_0^{-\frac{1}{2}} \mathbf{e}^\pm$ ,  $\mathbf{H}^\pm = \mu_0^{-\frac{1}{2}} \mathbf{h}^\pm$ . In this case, the near field can be interpreted as the induced polarization current in  $V^+$ ; in other words, the fictitious polarization current can be determined by the known near field. Then, the far field can be computed as the fields created by the polarization current in free-space. The polarization current is defined as

$$\mathbf{i}_P = \frac{\partial \mathbf{P}}{\partial t}, \quad (4.77)$$

where  $\mathbf{P}$  is the polarization

$$\mathbf{P} = (\epsilon_+ - \epsilon_0) \mathbf{E}_{total}^+. \quad (4.78)$$

For time-harmonic fields, it is easy to see:

$$\mathbf{i}_P = j\omega (\epsilon_+ - \epsilon_0) (\mathbf{E}^+ + \mathbf{E}_{in}^+). \quad (4.79)$$

On the other hand, the scattered far field can be expressed in terms of localized polarization current as

$$\mathbf{h}(Q) = \nabla \times \mathbf{A}(Q), \quad (4.80)$$

and

$$\mathbf{A}(Q) = \frac{\mu_0}{4\pi} \left[ \int_{V^+} \mathbf{i}_P(M) dV_M \right] \left( \frac{e^{-ikr_{MQ}}}{r_{MQ}} \right). \quad (4.81)$$

By using formula (4.56), from (4.80)-(4.81) we get

$$\mathbf{h}^-(Q) = \frac{1}{4\pi} \int_{V^+} \mathbf{i}_P(M) \times \nabla_Q \left( \frac{e^{-ikr_{MQ}}}{r_{MQ}} \right) dV_M. \quad (4.82)$$

Note that

$$\nabla_Q \left( \frac{e^{-ikr}}{r} \right) = -\mathbf{r}_{MQ} \left( ik + \frac{1}{r} \right) \frac{e^{-ikr}}{r}, \quad (4.83)$$

and for the scattered field in the far field zone, we can drop the  $1/r$  term; therefore, equation (4.82) is reduced to

$$\mathbf{H}^-(Q) \simeq \frac{ik}{4\pi} \int_{V^+} [\hat{\mathbf{r}}_{MQ} \times \mathbf{i}_P(M)] \frac{e^{-ikr_{MQ}}}{r_{MQ}} dV_M. \quad (4.84)$$

The last expression can be further simplified since the term  $\hat{\mathbf{r}}_{MQ} \frac{e^{-ikr_{MQ}}}{r_{MQ}}$  does not depend on point  $M$  explicitly when the observation is made from the far field

$$\mathbf{H}_s^-(Q) \approx \frac{ck^2}{4\pi} \frac{e^{-ikr_{MQ}}}{r_{MQ}} \hat{\mathbf{r}}_{MQ} \times \left[ \int_{V^+} \mathbf{P}(M) dV_M \right]. \quad (4.85)$$

Since the electromagnetic fields in the far field zone can be always considered as plane waves, the electric field and magnetic field has the following simple relation

$$\mathbf{E}_s^-(Q) = Z_0 \mathbf{H}_s^-(Q) \times \mathbf{k}, \quad (4.86)$$

where  $Z_0$  is the intrinsic impedance of free-space. So we get the final expression for electrical far field:

$$\mathbf{E}_s^-(Q) = \frac{ck^2 Z_0}{4\pi} \frac{e^{-ikr_{MQ}}}{r_{MQ}} \hat{\mathbf{r}}_{MQ} \times \left[ \int_{V^+} \mathbf{P}(M) dV_M \right] \times \hat{\mathbf{r}}_{MQ}. \quad (4.87)$$

If we assume the polarization is along the x-axis, and propagation is along the z-axis, according to (4.28), the forward scattering amplitude is

$$\mathbf{F}(\mathbf{z}, \hat{\mathbf{z}}) = \frac{ck^2 Z_0}{4\pi} \hat{\mathbf{z}} \times \left[ \int_{V^+} \mathbf{P}(M) dV_M \right] \times \hat{\mathbf{z}}. \quad (4.88)$$

Finally, by taking (4.88) into (4.29) we arrive following expression for the ECS:

$$\sigma_{ext} = ckZ_0 \text{Im} \left[ \hat{\mathbf{e}}_i \cdot \frac{(\hat{\mathbf{z}} \times \int_{V^+} \mathbf{P}(M) dV_M) \times \hat{\mathbf{z}}}{E_0} \right]. \quad (4.89)$$

### 4.3 Numerical techniques to compute ECS

#### 4.3.1 Discretization of the inhomogeneous integral equation

Let us partition  $S$  into  $N$  small pieces  $\Delta S_j$  and rewrite integral equation (4.47) as follows:

$$\sigma(Q_i) - \frac{\lambda}{2\pi} \sum_{j=1}^{Ne} \int_{\Delta S_j} \sigma(M_j) \frac{\mathbf{r}_{M_j Q_i} \cdot \mathbf{n}_{Q_i}}{r_{M_j Q_i}^3} dS_j = 2\epsilon_0 \lambda \mathbf{n}_{Q_i} \cdot \mathbf{e}_{in}^+. \quad (4.90)$$

Now we integrate (4.90) over  $\Delta S_i$  and exchange the order of the integral

$$\int_{\Delta S_i} \sigma(Q_i) dS_i - \frac{\lambda}{2\pi} \sum_{j=1}^{Ne} \int_{\Delta S_j} \sigma(M_j) \left[ \int_{\Delta S_i} \frac{\mathbf{r}_{M_j Q_i} \cdot \mathbf{n}_{Q_i}}{r_{M_j Q_i}^3} dS_i \right] dS_j = 2\epsilon_+ \epsilon_0 \lambda \int_{\Delta S_i} \mathbf{n}_{Q_i} \cdot \mathbf{e}_{in}^+ dS_i. \quad (4.91)$$

By introducing the notation

$$\omega_{ij} = \begin{cases} \frac{\mathbf{r}_{M_j Q_i} \cdot \mathbf{n}_{Q_i}}{r_{M_j Q_i}^3} \Delta S_i & \text{if } i \neq j, \\ 2\pi - \sum_{-j=1, j \neq i}^{Ne} \frac{\mathbf{r}_{M_j Q_i} \cdot \mathbf{n}_{Q_i}}{r_{M_j Q_i}^3} \Delta S_i & \text{if } i = j, \end{cases} \quad (4.92)$$

the last formula can be presented as follows:

$$\sum_{j=1}^{Ne} \omega_{ij} \int_{\Delta S_j} \sigma_0(M_j) dS_j - \frac{2\pi}{\lambda} \int_{\Delta S_i} \sigma(Q_i) dS_i = -4\pi\epsilon_0 \int_{\Delta S_i} \mathbf{n}_{Q_i} \cdot \mathbf{e}_{in}^+(Q_i) dS_i. \quad (4.93)$$

Define:

$$X_i = \int_{\Delta S_i} \sigma_0(Q_i) dS_i, \quad (4.94)$$

$$I_i = \int_{\Delta S_i} \mathbf{n}_{Q_i} \cdot \mathbf{e}_{in}^+(Q_i) dS_i, \quad (4.95)$$

we get the following linear system for surface charges:

$$\sum_{j=1}^{Ne} \omega_{ij} X_j - \frac{2\pi}{\lambda} X_i = -4\pi\epsilon_0 I_i. \quad (4.96)$$

### 4.3.2 Far field and dipole moment

Once the surface charge distribution is known, the far field can be computed by using the algorithm introduced in previous section. However, there is a more efficient way for which the computation of far field can be reduced to the calculation of dipole moment. In the following, we demonstrate how this can be done. According to equation (4.85), the central problem is to compute the following integral:

$$\mathbf{I}_P = \int_{V^+} \mathbf{P}(M) dV_M = (\epsilon_+ - \epsilon_0) \int_{V^+} (\mathbf{E}_{sc}^+ + \mathbf{E}_{in}^+) dV_M. \quad (4.97)$$

Since the incident field is practically constant within the volume (because the free-space wavelength is much larger than object dimension and we observe from far field

point), we have:

$$\mathbf{I}_{Pin} = (\epsilon_+ - \epsilon_0) \mathbf{E}_{in}^+(M_0)V. \quad (4.98)$$

This reduces the problem to how to calculate the polarization current due to scattered fields:

$$\mathbf{I}_{Psc} = (\epsilon_+ - \epsilon_0) \epsilon_0^{-\frac{1}{2}} \int_{V^+} \mathbf{e}_0^+ dV_M. \quad (4.99)$$

To this end, let us introduce the vector  $\mathbf{d}$  and its scalar components as following:

$$\mathbf{d} = \oint \sigma(M) \mathbf{r}_{MQ} dS_M, \quad (4.100)$$

$$d_x = \oint \sigma(M) x_M dS_M, \quad d_y = \oint \sigma(M) y_M dS_M, \quad d_z = \oint \sigma(M) z_M dS_M. \quad (4.101)$$

On the other hand, according to formula (2.20), we have

$$\sigma = \epsilon_0 \mathbf{n} \cdot (\mathbf{E}^- - \mathbf{E}^+). \quad (4.102)$$

By taking (4.102) into the first boundary condition in (4.38), after simple transformation, we arrive at

$$\sigma = (\epsilon_+ - \epsilon_0) (\mathbf{n} \cdot \mathbf{E}^+ + \mathbf{n} \cdot \mathbf{E}_{in}). \quad (4.103)$$

Then the x-component of vector  $\mathbf{d}$  can be computed as:

$$d_x = (\epsilon_+ - \epsilon_0) \oint (\mathbf{n} \cdot \mathbf{E}^+ + \mathbf{n} \cdot \mathbf{E}_{in}) x_M dS_M = (\epsilon_+ - \epsilon_0) \int_V (E_x^+ + E_{inx}) dV_M. \quad (4.104)$$

Therefore, we have

$$\mathbf{d} = \alpha \int_V (\mathbf{E}^+ + \mathbf{E}_{in}) dV_M = \mathbf{I}_P. \quad (4.105)$$

Then for the plane wave defined in (4.24)-(4.26), according to (4.88) the ECS can be represented in terms of  $\mathbf{d}$ .

$$\sigma_{ext} = ckZ_0 Im \left[ \hat{\mathbf{x}} \cdot \frac{(\hat{\mathbf{z}} \times \mathbf{d}) \times \hat{\mathbf{z}}}{E_0} \right]. \quad (4.106)$$

This expression greatly simplifies the computation of ECS since the dipole moment  $\mathbf{d}$  is very easy to compute once the surface charge is known.

### 4.3.3 Numerical results

The numerical technique discussed above has been software implemented and tested. The algorithm described above has been first tested for spherical particles where exact analytical solutions are available (Mie theory).

$$\sigma_{ext} = \pi a^2 4x \mathbf{Im} \left( \frac{\epsilon_p - \epsilon_m}{\epsilon_p + 2\epsilon_m} \right), \quad (4.107)$$

$$x = \frac{2\pi}{\lambda} a N, \quad (4.108)$$

where  $a$  is the radius of the sphere and  $N$  is the refractive index for surrounding medium. We have computed the extinction cross section of nanospheres for different materials. Fig. 4.3 and Fig. 4.4. are the results for Au and Ag, respectively. It is apparent that the numerical results are very accurate. The computational results of ECS for Au ellipsoidal nanoparticles with different aspect ratios are presented in Figure 4.5. It can be seen that adjusting the aspect ratio of the ellipsoidal nanoparticle is an effective way to tune the plasmon resonances. Figure 4.6 demonstrates the computational results for gold nano-rings placed on a dielectric substrate, illustrating that we have reasonable agreement with the experiment results. Finally, the computation for semiconductor materials is also performed. The results for InSb sphere are shown in Fig. 4.7.

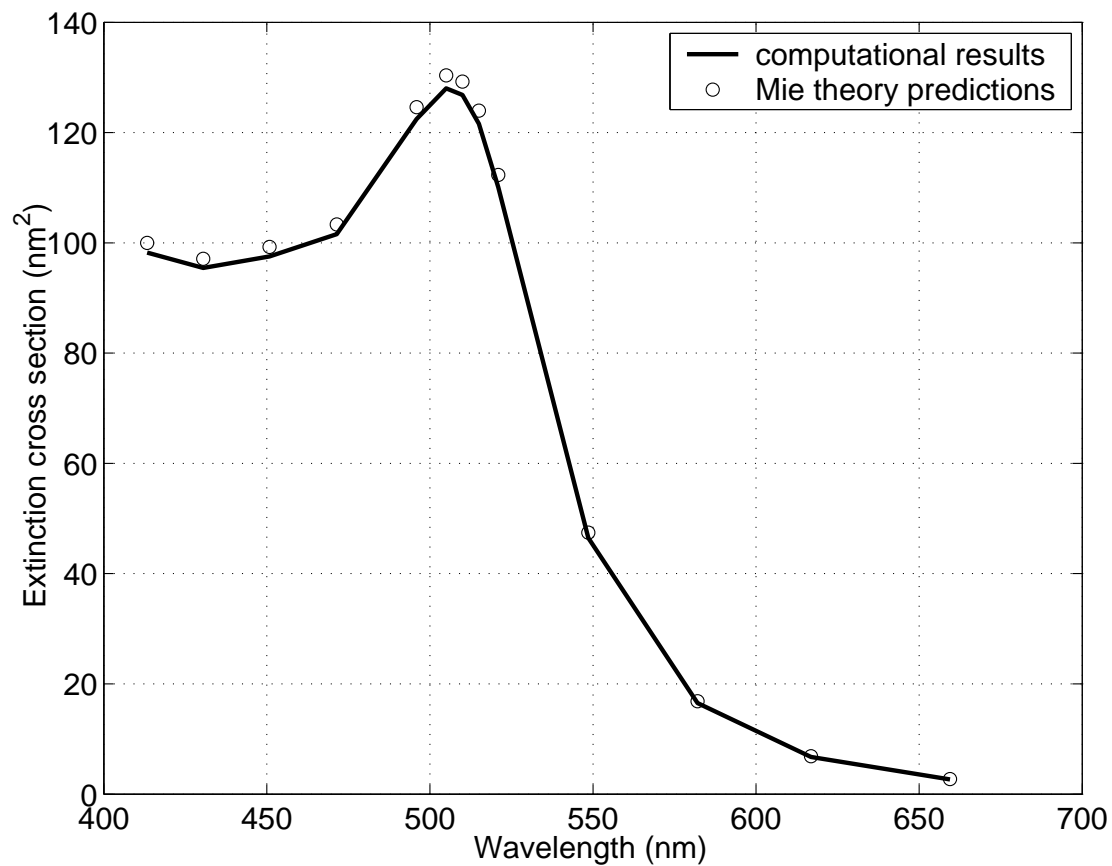


Figure 4.3: Computational results compared with the Mie theory predictions for the extinction cross section of a single Au nanoparticle (diameter = 10 nm).

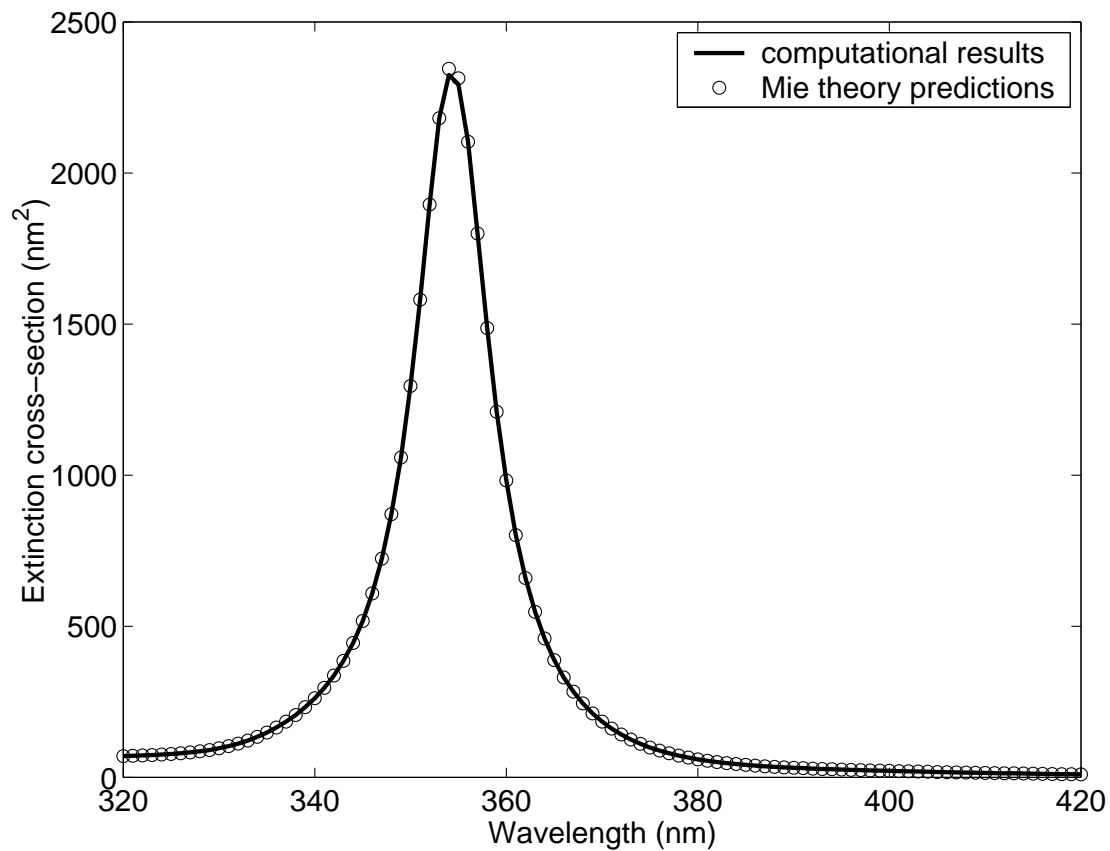


Figure 4.4: Computational results compared with the Mie theory predictions for the extinction cross section of a single Ag nanosphere (diameter = 20 nm).



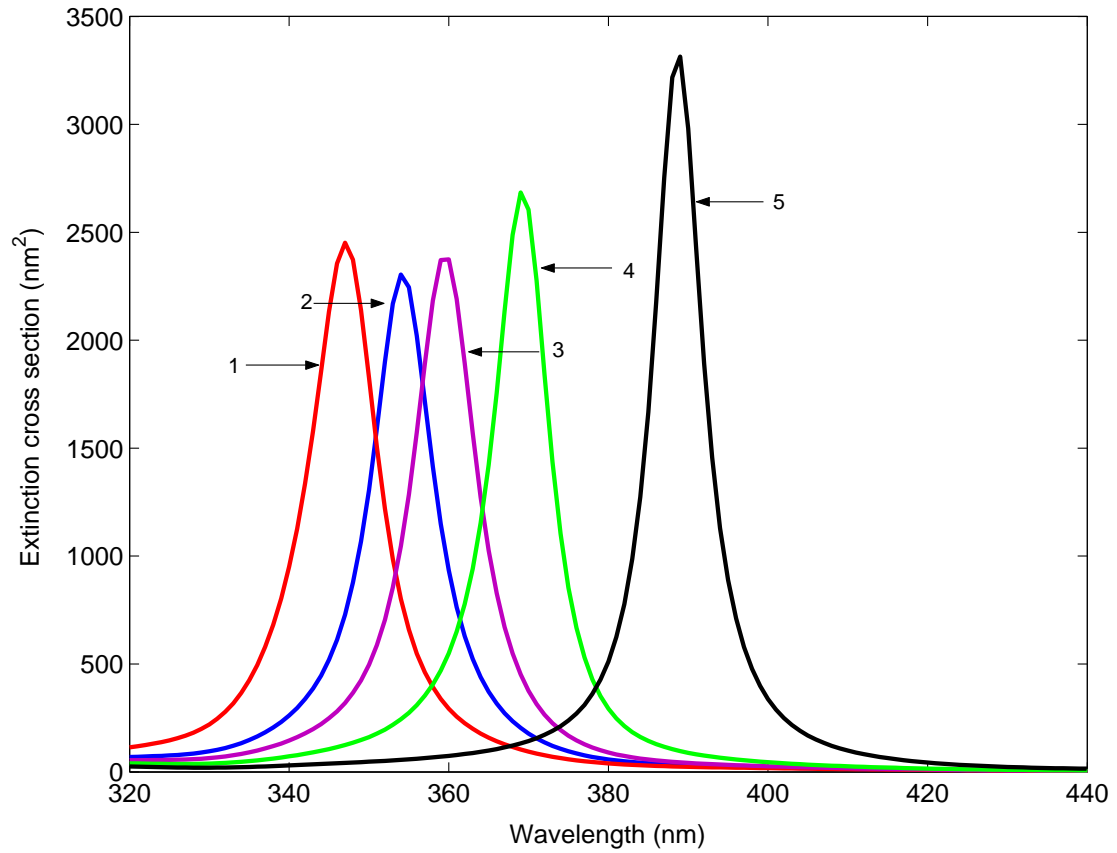


Figure 4.5: Computational results of the extinction cross section of a single Ag nanoellipsoid, with different aspect ratios: 1:1:0.8, 1:1:1, 1:1:1.2, 1:1:1.4, 1:1:1.6 for curve 1, 2, 3, 4, 5, respectively.

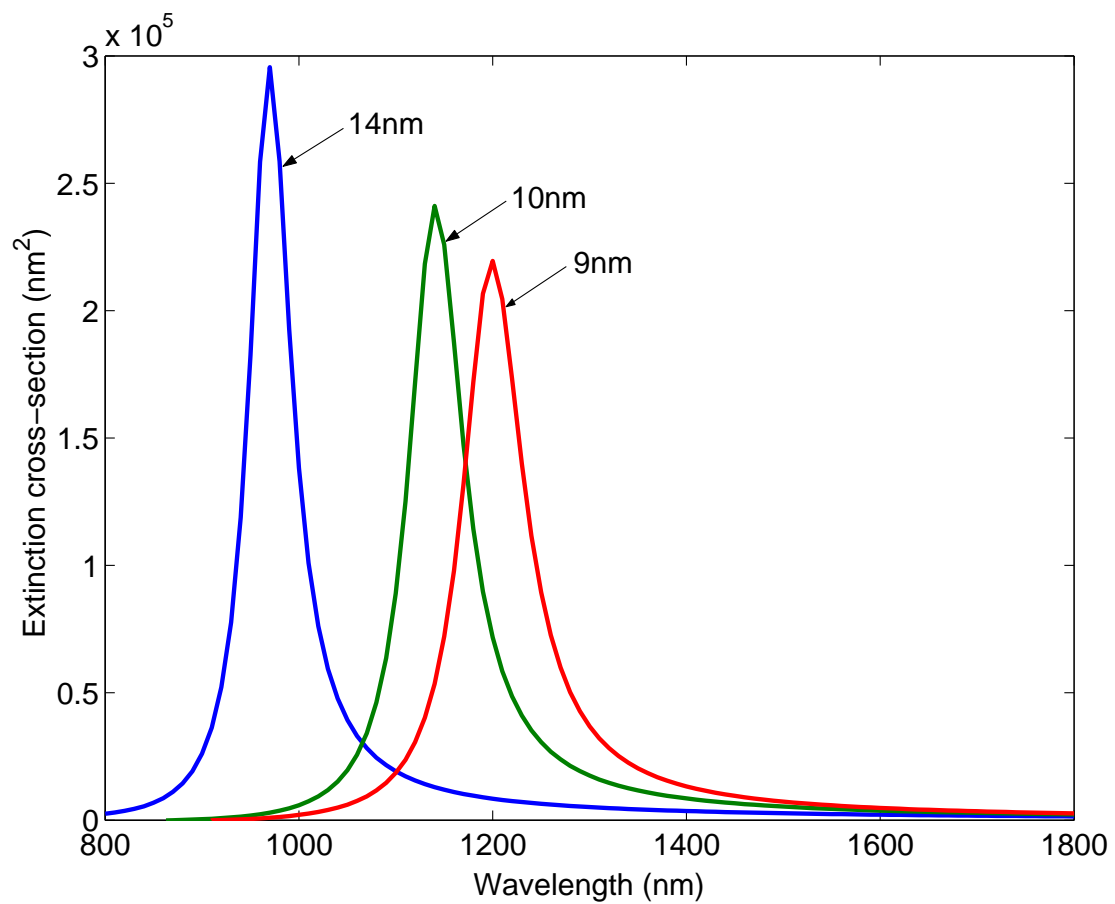


Figure 4.6: Computed extinction cross sections of Au nanorings placed on substrate, the dimensions of these rings are provided in Table 2.3.

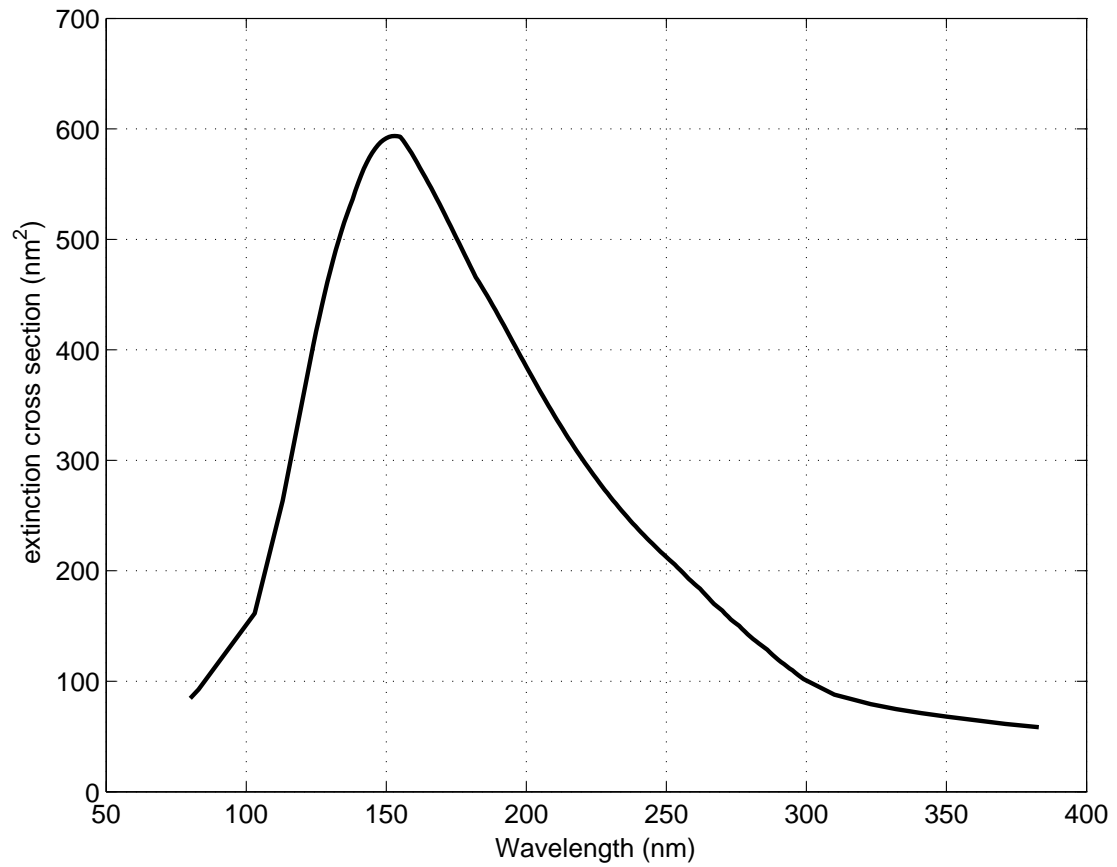


Figure 4.7: Computational extinction cross section of a single InSb nanosphere (diameter = 20 nm) placed on a glass substrate  $\epsilon = 2.25\epsilon_0$ .

## 4.4 Numerical analysis of plasmon waveguides of light

Plasmon waveguides of light have been the focus of considerable research lately [10, 11, 12]. These plasmon waveguides consist of an array of metallic nanoparticles with their resonance frequencies in the region of optical waveguiding. These nanoparticle-structured waveguides hold the unique promise for light guiding and bending at the nanoscale. For this reason, they are considered very instrumental in the emerging field of nanophotonics where the information transmission and processing occur entirely at the optical level. In this section, the technique for the calculation of resonance frequencies of nanoparticle-structured waveguides is presented. This technique is based on the boundary integral equation method and, in this sense, it can be considered as the further extension of the technique for the analysis of plasmon resonances in metallic nanoparticles developed in previous part of this dissertation.

### 4.4.1 The numerical technique

To start the discussion, consider a chain of identical metallic nanoparticles subject to incident optical radiation on its left edge (see Figure 4.8). At specific frequencies, this optical incident radiation will excite plasmon resonances in the first nanoparticle, which then through near-field coupling will induce plasmon resonances in all nanoparticles that form the chain. This is, in a nutshell, the physical mechanism of light plasmon waveguiding.

It is well known that plasmon resonances occur when the free-space wavelength of light is large in comparison with particle dimensions. For this reason, the time-

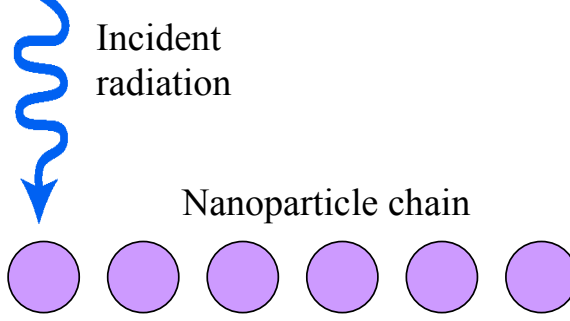


Figure 4.8: Schematic of plasmonic waveguide of light.

harmonic electromagnetic fields within each nanoparticle and around it vary almost with the same phase. In other words, at any instant of time, the fields locally (around each particle) look like electrostatic fields. By using this fact, the following integral equation can be derived for each particle in the chain:

$$\sigma_p(Q) - \frac{\lambda}{2\pi} \oint_{S_p} \sigma_p(M) \frac{\mathbf{r}_{MQ} \cdot \mathbf{n}_Q}{r_{MQ}^3} dS_M = -2\lambda\epsilon_0 \mathbf{n}_Q \cdot \mathbf{E}_{ap}, \quad (4.109)$$

$$\lambda = \frac{\epsilon_+(\omega) - \epsilon_0}{\epsilon_+(\omega) + \epsilon_0}. \quad (4.110)$$

Here,  $p$  is the nanoparticles number in the chain,  $\sigma$  is the fictitious single layer of charges distributed over boundary  $S$ ,  $\mathbf{E}_{ap}$  is the electric field that has two distinct parts (the incident field as well as the field scattered by all other nanoparticles), and  $\epsilon_+(\omega)$  and  $\epsilon_0$  are the dielectric permittivities of nanoparticles and the surrounding medium, respectively.

The dimensions of the waveguiding chain are usually comparable to the wavelength of the incident radiation. As a result, the phase shift in time-harmonic electromagnetic fields scattered by different particles cannot be neglected. This

situation can be accounted for in equation (4.109) as follows:

$$\sigma_p(Q) - \frac{\lambda}{2\pi} \oint_{S_p} \sigma_p(M) \frac{\mathbf{r}_{MQ} \cdot \mathbf{n}_Q}{r_{MQ}^3} dS_M = -2\lambda\epsilon_0 \mathbf{n}_Q \cdot (\mathbf{E}_{in} + \mathbf{E}_{scat}), \quad (4.111)$$

where  $\mathbf{E}_{in}$  is the electric field of incident radiation, while  $\mathbf{E}_{scat}$  is the field scattered by all other nanoparticles in the chain that can be computed by using the formula

$$\mathbf{E}_{scat}(Q) = \frac{1}{4\pi\epsilon_0} \oint_{S_p} \sigma(M) \left( ik + \frac{1}{r_{MQ}} \right) \frac{\mathbf{r}_{MQ} e^{ikr_{MQ}}}{r_{MQ}^2} dS_M, \quad \tilde{S}_p = \sum_{k \neq p} S_k. \quad (4.112)$$

By solving the coupled integral equations, the extinction cross-section and its dependence on the frequency can be computed [8]. The frequency at which the extinction cross-section achieves its maximum value can be identified as the resonance frequency for which the light guiding is the most efficient.

Next, we briefly describe the discretization technique for the solution of integral equation (4.111). In a similar procedure to what we did before, let us partition  $S_p$  into  $N$  small pieces  $\Delta S_j$ , although the kernel in this case will be hybrid. Nevertheless, equation (4.111) can be transformed to the following matrix form:

$$\sum_{j=1}^N \omega_{ij} X_j - \frac{2\pi}{\lambda} X_i + \sum_{k=1, k \neq p}^M \sum_{j=1}^N \Omega_{km} = -4\pi\epsilon_0 I_i, \quad (4.113)$$

where

$$\omega_i(M) = \int_{\Delta S_j} \frac{\mathbf{r}_{MQ} \cdot \mathbf{n}_Q}{r_{MQ}^3} dS_Q, \quad (4.114)$$

$$X_i = \int_{\Delta S_j} \sigma(Q) dS_Q, \quad (4.115)$$

$$I_i = \int_{\Delta S_j} \mathbf{n}_Q \cdot \mathbf{E}_{in}^{(p)} \mathbf{n}_Q, \quad (4.116)$$

$$\Omega_i = \int_{\Delta S_j} \mathbf{n}_Q \cdot \mathbf{r}_{MQ} \left( ik + \frac{1}{r_{MQ}} \right) \frac{\mathbf{r}_{MQ} e^{ikr_{MQ}}}{r_{MQ}} dS_Q. \quad (4.117)$$

The linear system defined by (4.113) can be efficiently solved by using the GMRES algorithm. The numerical technique based on discretization (4.113) has been software implemented and extensively tested. This technique is illustrated by the examples presented in the following section.

#### 4.4.2 Numerical results

First, we present the results of computations and their comparison with available experimental data [11] for a chain of seven spherical gold nanoparticles of 50nm diameter and separated by 25nm from one another. The comparison between the resonance waveguide frequencies found experimentally in [11] and our computational results for these frequencies is presented in the Table 4.1. This table reveals fairly good agreement between computational and experimental results.

The extinction cross sections for longitudinal and transverse polarizations of incident radiation are shown in Figure 4.9. It is apparent from this figure that the longitudinal mode has better transmission properties than the transverse mode; this is not surprising because the longitudinal mode offers better confinement of plasmon resonant fields. The silver and gold dispersion relations published in [9] have been used in our calculations. Furthermore, we have performed computations for the 11-gold-sphere waveguides with the different nanoparticles arrangements. In these simulations, the nanoparticles of 50nm in diameter and 75nm center-to-center distance have been used. For the chain structure (Fig. 4.10), the extinction cross sections for the longitudinal mode are shown in Figure 4.11). By comparing this figure with Table 4.1, it can be observed that the resonance frequency of the

11-sphere chain is about 605nm, which is further shifted to the longer wavelength.

Figures 4.13 and 4.15 present the extinction cross-sections for the T-shape (Fig. 4.12) and L-shape (Fig. 4.14) nanoparticle waveguides, respectively. For the T-shape waveguide, the transverse polarization excitation is at the short end. When the plasmon resonant fields are coupled to the longer arm, the mode becomes longitudinal. For the L-shape waveguide, the longitudinal polarization excitation is at the end of the long arm. In these structures, the right angles between particle arrays are responsible for the polarization transformations.

In this section, the novel numerical approach to the analysis of nanoparticle-structured plasmon waveguides of light has been presented. The extinction cross-sections and resonance (propagation) frequencies are computed for various geometries of these waveguides and compared with available experimental data. The computational results for resonance frequencies corresponding to different light polarizations are illustrated as well.

Table 4.1: Resonance frequencies for gold 7-sphere-chain waveguide.

	Experimental result [11]	Computational results
Transverse polarization	585 nm	534 nm
Longitudinal polarization	602 nm	572 nm



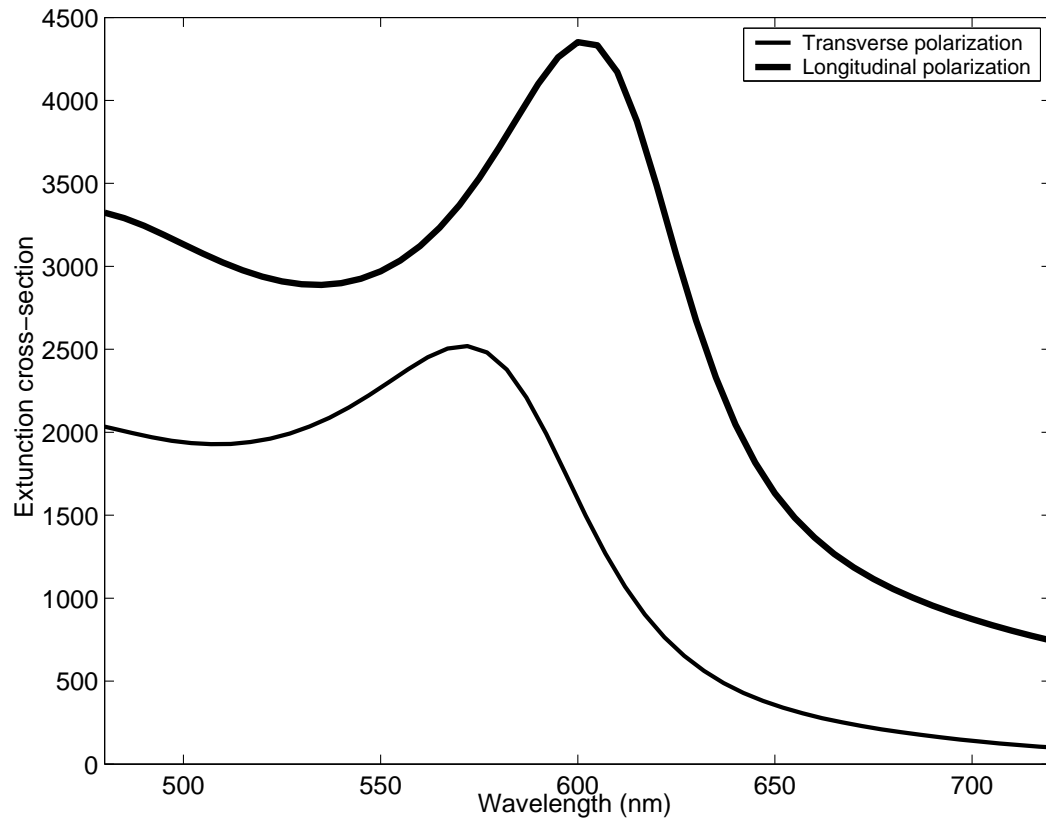


Figure 4.9: Computed extinction cross sections of gold 7-sphere-chain waveguide for the transverse and longitudinal polarization modes (diameter = 50nm, center-to-center distance = 25nm).

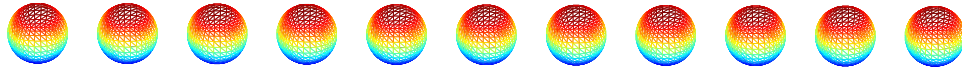


Figure 4.10: Schematic of gold 11-sphere-chain waveguide of light

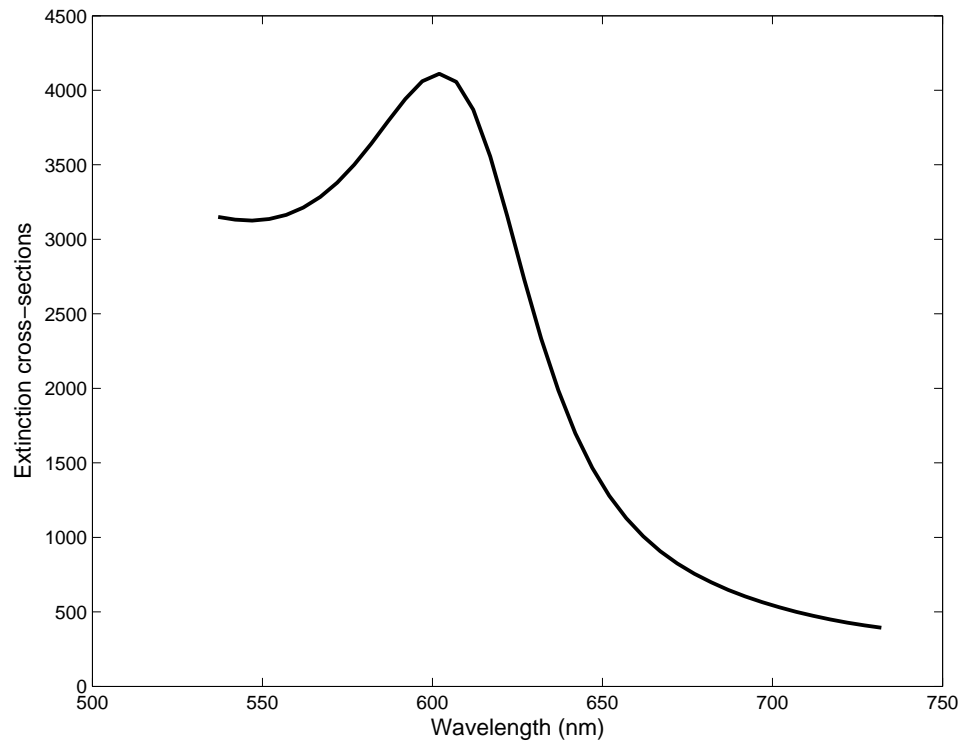


Figure 4.11: Computed extinction cross sections of gold 11-sphere-chain waveguide for the longitudinal polarization mode (diameter = 50nm, center-to-center distance = 25nm).

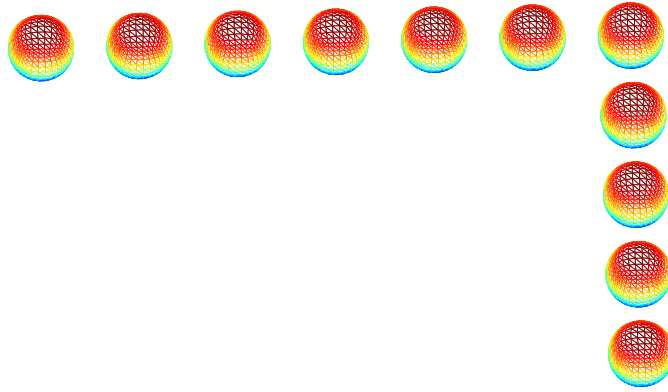


Figure 4.12: Schematic of gold L-shape 11-sphere waveguide of light

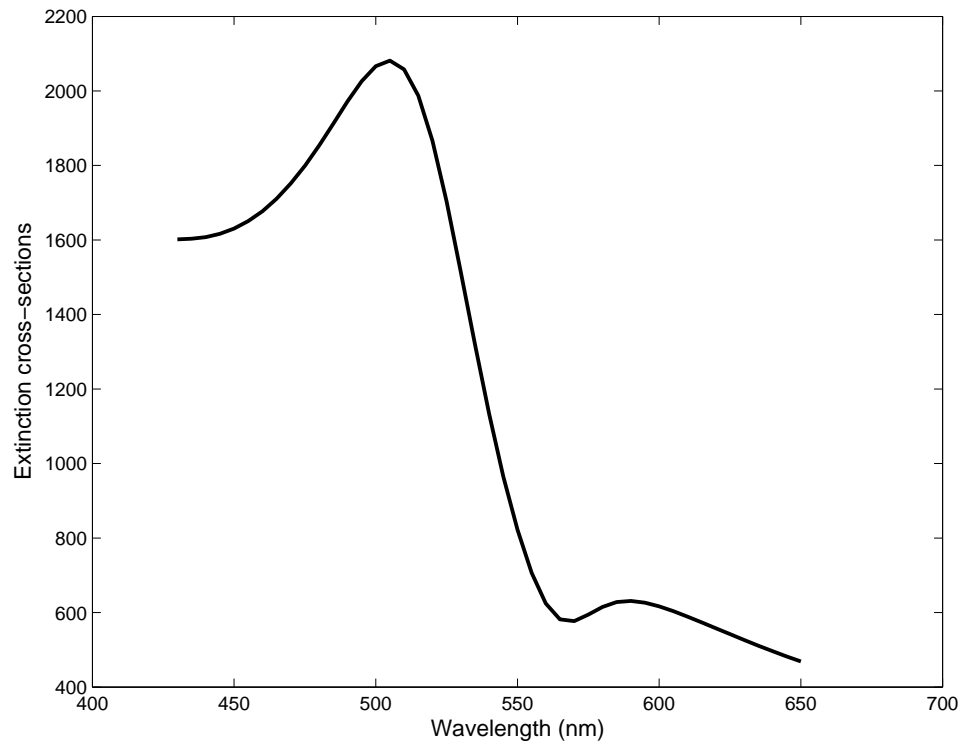


Figure 4.13: Computed extinction cross sections of gold L-shape 11-sphere waveguide for the longitudinal polarization mode (diameter = 50nm, center-to-center distance = 25nm).

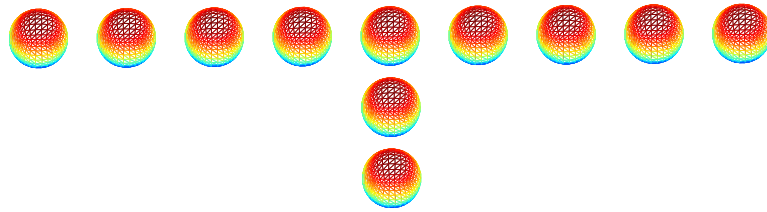


Figure 4.14: Schematic of gold T-shape 11-sphere waveguide of light

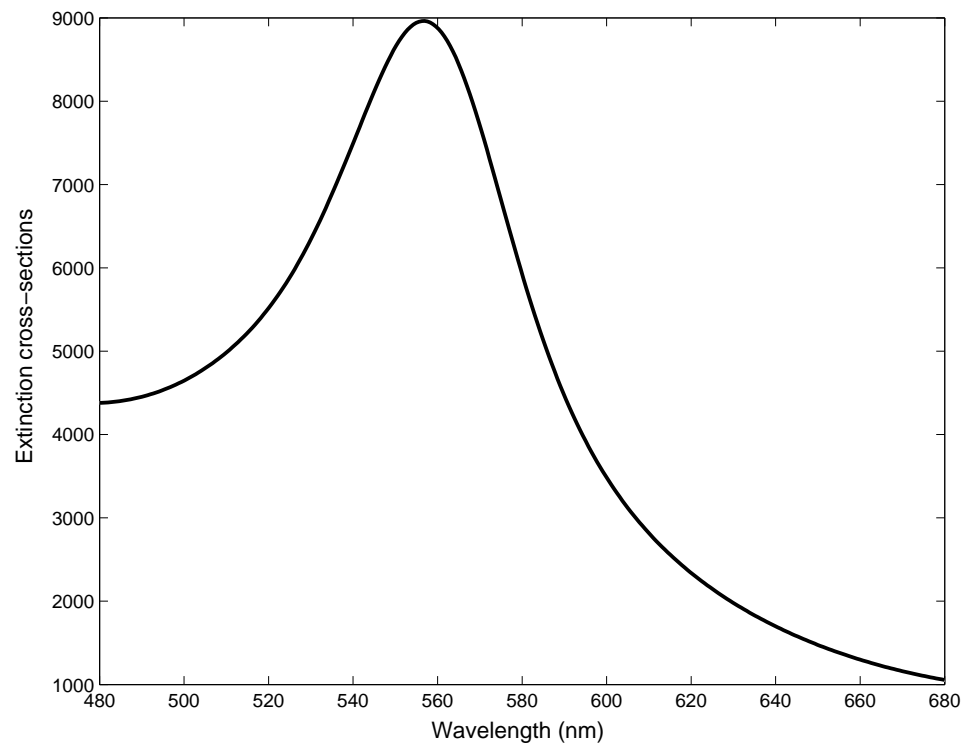


Figure 4.15: Computed extinction cross sections of gold T-shape 11-sphere waveguide for the longitudinal polarization mode (diameter = 50nm, center-to-center distance = 25nm).

## Chapter 5

### **Conclusion**

Plasmon resonance in nanoparticles is a unique nanoscale phenomenon which has numerous scientific and technological applications in such areas as near-field microscopy, nano-lithography, surface enhanced Raman scattering, nanophotonics, biosensors, optical data storage, etc. For this reason, the understanding of the optical properties of nanoparticles holds both fundamental and practical significance. While considerable experimental and theoretical work has been done in this field, the accurate and efficient modeling of plasmon resonances in three-dimensional nanoparticles for arbitrary shape remains a challenge.

In this dissertation, we developed a robust and efficient technique to fully characterize the plasmon resonances and performed a comprehensive numerical analysis of plasmon resonances in three-dimensional nanostructures. This surface integral equation technique is based on the observations that plasmon resonances in nanoparticles occur at specific frequencies for which the particle permittivity is negative and the free-space wavelength of the radiation is large in comparison with particle dimensions. By using perturbation technique to Maxwell's equations, the problem of determining resonance frequencies is framed as a classical eigenvalue problem. It is shown that the resonance values of dielectric permittivities as well as resonance frequencies can be directly found through the solution of this eigenvalue problem

for three-dimensional nanoparticles.

This integral equation method leads to fully populated discretized matrix equations that are computationally expensive to solve, especially when a large number of particles are involved in the nanostructures. Since the fully populated matrices are generated by integrals with  $1/r$ -type kernel, this computational problem can be appreciably alleviated by using the fast multipole method. This method greatly speeds up the matrix-vector multiplications. By implementing the FMM algorithm in the solution of the eigenvalue problem, the integral equation technique becomes computationally very efficient compared to other technique such as finite-difference time-domain (FDTD) method.

We have extended this technique to the computation of extinction cross sections from which important information such as the strength and FWHM of plasmon resonances can be obtained. The applications of plasmon resonances have also been considered. We performed extensive numerical studies for metallic nanoshells and plasmon waveguides of light, which are very promising for bio-sensing applications and light guiding and bending under the diffraction limit, respectively. It can be seen that the technique developed throughout this dissertation can be very instrumental for the design of plasmon resonant nanoparticles and tailor their optical properties for various applications.

To further advance the understanding of optical properties of nanoparticles and pursue its applications in new promising technology, the following issues can be foreseen in the near future:

- (1) Time dynamic analysis of plasmon resonances. The temporal analysis of

specific plasmon modes is the least studied area of plasmonics. Nevertheless, the temporal analysis of plasmon modes is much needed in order to fully comprehend the time-dynamics of their excitation as well as their saturation and decay. This temporal analysis can also be very instrumental in the area of light controllability of plasmon resonances in semiconductor nanoparticles, where proper time synchronization of excitation of specific plasmon modes may be required. During our future research work on this project, the temporal analysis of plasmon modes should be addressed.

(2) Plasmon resonances in semiconductor nanoparticles. Plasmon resonances can be controlled through the manipulation of conduction electron density. In semiconductors, the manipulation of conduction electron density can be accomplished by doping as well as by optical and depletion means. Indeed, by appropriate doping of semiconductor nanoparticles, the wide range of controllability of  $\omega_p$  can be achieved and, in this way, the semiconductor nanoparticles can be tuned to resonate at desirable frequencies. The optical controllability is especially attractive because it could be utilized for the development of nanoscale light switches and all-optical nano-transistors.

(3) Loss reduction in plasmonic circuits. A major obstacle for the applications of plasmonic sub-wavelength waveguides and circuits is the high losses compared to conventional optical waveguides. The losses are mainly due to the absorption, scattering and coupling. This problem can be attacked from two aspects: one is to design novel metallic nanostructures to minimize the coupling losses; the other one is to embed the nanostructures into an optically active medium to compensate for

the absorption and scattering losses. The successful solution of this problem could lead to the realization of plasmonic chips.

The surface integral technique is a powerful tool for the study of plasmon resonances in nanoparticles and their applications. We hope that future developments and improvement will greatly expand its capabilities and make it an indispensable tool in this exciting and promising area.



## BIBLIOGRAPHY

- [1] National Science and Technology Council and Subcommittee on Nanoscale Science, “*National Nanotechnology Initiative: The Initiative and its Implementation Plan*”, Engineering and Technology Report, July 2000.
- [2] S. Link and M. A. El-Sayed, “Optical Properties and Ultrafast Dynamics of metallic Nanocrystals”, *Annu. Rev. Phys. Chem.* vol.54, pp.331-366, 2003.
- [3] U. Kreibig and M. Vollmer, *Optical properties of metal clusters*, Springer Series in Material Science, vol.25, 1995.
- [4] G. Mie, “A contribution to the optics of turbid media special colloidal metal solutions”, *Ann. Phys.* 25, pp.377-445, 1908.
- [5] M. C. Daniel and D. Astruc, “Gold nanoparticles: assembly, supramolecular chemistry, quantum-size-related properties, and applications toward biology, catalysis and nanotechnology”, *Chem. Rev.* vol.104, pp.293-346, 2004.
- [6] B. Wiley, Y. Sun, J. Chen, H. Cang, Z.-Y. Li, X. Li, and Y. Xia, “Shape-controlled synthesis of silver and gold nanostructures”, *MRS Bull.*, vol.30, pp.356-361, 2005.
- [7] R. C. Jin, Y. W. Cao, C. A. Mirkin, K. L. Kelly, G. C. Schatz and J. G. Zheng, “Photoinduced conversion of silver nanospheres to nanoprisms”, *Science*, vol.294, pp.1901-1903, 2001.

- [8] W. L. Barnes, A. Dereux and T. W. Ebbesen, "Surface plasmon subwavelength optics", *Nature*, vol.424, pp.824-830, 2003.
- [9] I. D. Mayergoyz and Z. Zhang, "Numerical Analysis of Nanoparticle-structured Plasmon Waveguides of Light", *IEEE Transactions on Magnetics*, vol.43, pp.1685-1688, 2007.
- [10] S. A. Maier, P. G. Kik and H. A. Atwater, "Observation of coupled plasmon-polariton modes in Au nanoparticle chain waveguides of different lengths: Estimation of waveguide loss", *Applied Physics Letters*, vol.81, pp.1714-1716, 2002.
- [11] S. A. Maier, P. G. Kik and H. A. Atwater, "Optical Pulse Propagation in Metal Nanoparticle Chain Waveguide", *Physical Review B*, vol.67, 205402, 2003.
- [12] S. A. Maier, P. G. Kik, H. A. Atwater, S. Meltzer, E. Harel, B. E. Koel and Ari Requicha, "Local detection of electromagnetic energy transport below the diffraction limit in metal nanoparticle plasmon waveguides", *Nature Materials*, vol.2, pp229-232, 2003.
- [13] J. C. Hulteen, D. A. Treichel, M. T. Smith, M. L. Duval, T. R. Jensen and R. P. Van Duyne, *J. Phys. Chem. B*, vol.103, pp.3854-3863, 1999.
- [14] C. L. Haynes and R. P. Van Duyne, "Nanosphere Lithography: A Versatile Nano-fabrication Tool for Studies of Size-Dependent Nanoparticles Optics", *J. Phys. Chem. B*, vol.105, pp.5599-5611, 2001.

- [15] P. G. Kik, S. A. Maier, and H. A. Atwater, "Plasmon Printing A New Approach to Near-field Lithography", *Mater. Res. Soc. Symp. Proc.*, vol.705, pp.66-71, 2002.
- [16] M. Moskovits, "Surface-enhanced spectroscopy", *Rev. Mod. Phys.*, vol.57, pp.783-826, 1985.
- [17] S. Nie and S. R. Emory, "Probing Single Molecules and Single Nanoparticles by Surface-Enhanced Raman Scattering", *Science*, vol.275, pp.1102-1106, 1997.
- [18] K. Kneipp, Y. Wang, H. Kneipp, L. T. Perelman, I. Itzkan, R. R. Dasari, and M. S. Feld, "Single Molecule Detection Using Surface-Enhanced Raman Scattering (SERS)", *Physical Review Letter*, vol.78, 1667, 1997.
- [19] D. R. Fredkin and I. D. Mayergoyz, "Resonance Behavior of Dielectric Objects (Electrostatic Resonances)", *Physical Review Letter*, vol. 91, 253902, 2003.
- [20] I. D. Mayergoyz, D. R. Fredkin and Z. Zhang, "Electrostatic (Plasmon) Resonance in Nanoparticles", *Physical Review B* 72, 155412, 2005.
- [21] J. Tominnaga, C. Mihalcea, D. Buchel, H. Fukuda, T. Nakano, N. Atoda, H. Fuji and T. Kikukawa, "Local Plasmon Photonic Transistor", *Applied Physics Letters*, vol.78, pp.2417-2419, 2001.
- [22] R. Elghanian, J. J. Storhoff, R. C. Mucic, R. L. Letsinger and C. A. Mirkin, "Selective Colorimetric Detection of Poly-nucleotides Based on The Distance-Dependent Optical Properties of Gold Nanoparticles", *Science*, vol.277, pp.1078-1081, 1997.

- [23] S. Schultz, D. R. Smith, J. J. Mock, and D. A. Schultz, "Single-target molecule detection with nonbleaching multicolor optical immunolabels", *Proc. Natl. Acad. Sci.*, vol.97, pp.996-1001, 2000.
- [24] Kagan Kerman et al., "Recent Trends in Electrochemical DNA biosensor technology", *Measurement Science and Technology*, vol.15, pp.R1-R11, 2004.
- [25] G. P. Mitchell, C. A. Mirkin and R. L. Letsinger, "Programmed assembly of DNA functionalized quantum dots", *J. Am. Chem. Soc.*, vol.121, pp.8122-8123, 1999.
- [26] T. A. Taton, C. A. Mirkin and R. L. Letsinger, "Scanometric DNA Array Detection with Nanoparticle Probes", *Science* 289, pp.1757-1760, 2000.
- [27] E. Prodan, C. Radloff, N. J. Halas and P. Nordlander, "A Hybridization Model for The Plasmon Response of Complex Nano-structures", *Science*, vol.32, pp.419-422, 2003.
- [28] S. Lal, S. L. Westcott, R. N. Taylor, J. B. Jackson, P. Nordlander and N. J. Halas, "Light Interacting Between Gold Nanoshells Plasmon Resonance and Planar Optical Wave-guides", *Journal of Physical Chemistry B*, vol.106, pp.5609-5612, 2002.
- [29] J. B. Pendry, A. J. Holden, W. J. Stewart and I Youngs, "Extremely Low Frequency Plasmon in Metallic Meso-structures", *Physical Review Letter*, vol.76, 4773, 1996.

- [30] G. Shvets and Y. A. Urzhumov, “Engineering the electromagnetic properties of periodic nanostructures using electrostatic resonances”, *Physical Review Letter*, vol.93, 243902, 2004
- [31] A. Alu, A. Salandrino, and N. Engheta, “Negative effective permeability and left-handed materials at optical frequencies”, *Optical Express*, vol.14, pp.1557-1567, 2006.
- [32] J. Tominnaga, T. Nakano and N. Atoda, *Proc. SPIE*, vol.3467, pp.282-286, 1999.
- [33] H. Ditlbacher, J. R. Krenn, B. Lamprecht, A. Leitner and F. Aussenegg, “Spectrally Coded Optical Data Storage by Metal Nanoparticles”, *Optical Letters*, vol.25, pp.563-565, 2000.
- [34] L. Men, J. Tominaga, H. Fuji, Q. Chen and N. Atoda, “High-density optical data storage using scattering-mode superresolution near-field structure”, *Proc. SPIE*, vol.4085, pp.204-207, 2001.
- [35] T. J. Silva and S. Schultz “A scanning near-field optical microscope for the imaging of magnetic domains in reflection”, *Rev. Sci. Instrum.*, vol.67, pp.715-725, 1996.
- [36] R. M. Stockle, Y. D. Suh, V. Deckert and R. Zenobi, “Nanoscale chemical analysis by tip-enhanced Raman spectroscopy”, *Chem. Phys. Lett.*, vol.318, pp.131-136, 2000.

- [37] B. P. Rand, P. Peumans, and S.R. Forrest, “Long-range absorption enhancement in organic tandem thin-film solar cells containing silver nanoclusters”, *Journal of Applied Physics*, vol.96, pp.7519-7526, 2004.
- [38] N. M. Lawandy, “Localized surface plasmon singularities in amplifying media”, *Applied Physics Letter*, vol.85, pp.5040-5042, 2004.
- [39] Craig F. Bohren and Donald R. Huffman, *Absorption and scattering of light by small particles*, John Wiley & Sons Press, 1983.
- [40] I. Grigorenko, S. Haas and A. F. J. Levi, “Electromagnetic Response of Broken-Symmetry Nanoscale Clusters”, *Phys. Rev. Lett.*, vol.97, 036806, 2006.
- [41] K. L. Kelly, A. A. Lazarides and G. C. Schatz, “Computational Electromagnetics of Metal Nanoparticles and Their Aggregates”, *Computing in Science and Engineering*, vol.3, pp.67-73, 2001.
- [42] E. Hao, G. C. Schatz and J. T. Hupp, “Synthesis and optical properties of anisotropic metal nanoparticles”, *Journal of Fluorescence*, vol. 14, pp.331-341, 2004.
- [43] E. M. Purcell and C. R. Pennypacker, “Scattering and absorption of light by nonspherical dielectric grain”, *The Astrophysical Journal*, vol.186, pp.705-714, 1973.
- [44] B. T. Draine, “The discrete-dipole approximation and its application to interstellar graphite grains”, *The Astrophysical Journal*, vol.333, pp.848-872, 1988.

- [45] S. K. Gray and T. Kupka, “Propagation of light in metallic nanowire arrays: Finite-difference time-domain studies of silver cylinders”, *Physical Review B* 68, 045415, 2003.
- [46] A. Taflov, *Computational Electrodynamics: The Finite-Difference Time-Domain Method*, Artech House, Boston, 3rd edition 2005.
- [47] K. S. Yee, “Numerical solution of initial boundary value problems involving Maxwells equations in isostropic media”, *IEEE Trans. Antennas Propag.*, vol.14, pp.302-307, 1966.
- [48] D. W. Mackowski and M. I. Mishenko, “Calculation of the T Matrix and the Scattering Matrix for Ensembles of Spheres”, *J. Optical Society America A*, vol. 35, pp.2266-2278, 1996.
- [49] M. I. Mishchenko, L. D. Travis, D. W. Mackowski, “T-matrix computations of light scattering by nonspherical particles: A review”, *J. Quant. Spectrosc. Radiat. Transfer*, vol.55, pp.535-575, 1996.
- [50] B. Peterson, S. Strom, “T-matrix formulation of electromagnetic scattering from multilayered scatterers”, *Phys. Rev. D*, vol.10 pp.2670-2684, 1974.
- [51] E. Moreno, D. Erni, C. Hafner, and R. Vahldieck, “Multiple multipole method with automatic multipole setting applied to the simulation of surface plasmons in metallic nanostructures”, *J. Opt. Soc. Am. A*, vol.19, pp.101-111, 2002.
- [52] L. Novotny, D.W. Pohl, and B. Hecht, “Scanning Near-Field Optical Probe with Ultrasmall Spot Size”, *Optical Letters*, vol. 20, pp.970C972, 1995.

- [53] C. Hafner, *The Generalized Multipole Technique for Computational Electromagnetics*, Artech House, Boston, 1990.
- [54] I. Mayergoyz, *Iterative Techniques for the Analysis of Static Fields in Inhomogeneous, Anisotropic and Nonlinear Media*, Naukova Dumka, Kyiv, 1976.
- [55] O. Tozoni and I. Mayergoyz, *Analysis of 3D Electromagnetic Fields*, Technika, Kyiv, 1974.
- [56] F. Ouyang and M. Isaacson, *Philos. Mag. B*, vol.60, pp.481, 1989.
- [57] F. Ouyang and M. Isaacson, *Ultramicroscopy*, vol.31, pp.345, 1989.
- [58] Z. Zhang and I. D. Mayergoyz, N. Gumerov, R. Duraiswami, "Numerical Analysis of Plasmon Resonances Based on Fast Multipole Method", *IEEE Transactions on Magnetics*, vol.43, pp.1465-1468, 2007.
- [59] I. D. Mayergoyz and Z. Zhang, "Numerical Analysis of Plasmon Resonances in Metallic Nanoshells with Silicon Core", *IEEE Transactions on Magnetics*, vol.43, pp.1689-1692, 2007.
- [60] I. D. Mayergoyz and Z. Zhang, "The Computation of Extinction Cross-sections of Resonant Metallic Nanoparticles Subject to Optical Radiation", *IEEE Transactions on Magnetics*, vol.43, pp.1681-1684, 2007.
- [61] I. D. Mayergoyz, Z. Zhang and G. Miano, "Analysis of Dynamics of Excitation and Dephasing of Plasmon Resonance Modes in Nanoparticle", *Physical Review Letters*, vol.98, 147401, 2007.



- [62] I. D. Mayergoyz and Z. Zhang, “Numerical Analysis of Plasmon Resonances in Nanoparticle”, IEEE Transactions on Magnetics, vol.42, pp.759-762, 2006.
- [63] I. D. Mayergoyz and Z. Zhang, “Modeling of The Electrostatic (Plasmon) Resonance in Metallic and Semiconductor Nanoparticle”, Journal of Computational Electronics, vol.4, pp.139-143, 2005.
- [64] L. Greengard, and V. Rokhlin, “A fast algorithm for particle simulations”, J. Comput. Phys., vol.73, pp.325-348, 1987
- [65] N. A Gumerov and R. Duraiswami, *Fast Multipole Methods for the Helmholtz Equation in Three Dimensions* (The Elsevier Electromagnetism Series), Elsevier Science, 2005.
- [66] N. A. Gumerov, R. Duraiswami and E. A. Borovikov, “Data structure, optimal choice of parameters, and complexity results for generalized multilevel fast multipole methods in d dimensions”, UMIACS TR 2003-28, University of Maryland, College Park, 2003.
- [67] Zhihui Tang, “Fast transforms based on structured matrices with applications to the fast multipole method”, Ph.D Dissertation, University of Maryland, 2004.
- [68] P. B. Johnson and R. W. Christy, “Optical Constant of The Noble Metals”, Physical Review B, vol.6, pp.4370-4379, 1972.
- [69] E. D. Palik, *Handbook of Optical Constant of Solids*, The Academic Press, 1985.

- [70] O. D. Kellogg, *Foundation of Potential Theory*, McGraw-Hill, New York, 1929.
- [71] S. G. Mikhlin, *Mathematical Physics, an Advanced Course*, North-Holland, Amsterdam, 1970.
- [72] J. Aizpurua and P. Hanarp and D. S. Sutherland and M. Kall and Garnett W. Bryant and F. J. Garcia de Abajo, *Phys. Rev. Lett.*, vol.90, 57401, 2003.
- [73] K. H. Su, Q. H. Wei, X. Zhang, J. J. Mock, D. R. Smith, and S. Schultz “Interparticle Coupling Effects on Plasmon Resonances of Nano-gold Particles”, *Nano Letters*, vol.3, pp.1087-1090, 2003.
- [74] L. J. Sherry, S. H. Chang, G. C. Schatz, and R. P. Van Duyne, “Localized surface plasmon resonance spectroscopy of single silver nanocubes”, *Nano Lett.*, vol.5, pp.2034-2038, 2005.
- [75] W. C. Chew, J. Jin, E. Michielssen and J. Song, “Fast and Efficient Algorithms in Computational Electromagnetics”, Artech House Publishers, 2000.
- [76] L. Greengard, “Fast algorithms for classical physics”, *Science*, vol.265, pp.909-914, 1994.
- [77] V. Rokhlin, “Rapid solution of integral equations of classical potential theory”, *Journal of Computational Physics*, vol.60, pp.187-207, 1983.
- [78] I. D. Mayergoyz, P. Andrei and M. Dimian, “Nonlinear magnetostatic calculations based on fast multipole method”, *IEEE Transactions on Magnetism*, vol.39, pp.1103-1106, 2003.

- [79] L. Greengard, *The Rapid Evaluation of Potential Fields in Particle System*, The MIT Press (ACM Distinguished Dissertation 1987), 1987.
- [80] N. A. Gumerov and R. Duraiswami, “Multiple scattering from N spheres using multipole reexpansion”, *J. Acoust. Soc. Am.*, vol.112, pp.2688-2701, 2002.
- [81] N. A. Gumerov, R. Duraiswami and E.A. Borovikov, “Data Structures, Optimal Choice of Parameters, and Complexity Results for Generalized Multilevel Fast Multipole Methods in d Dimensions”, UMIACS TR 2003-28, Also issued as Computer Science Technical Report CS-TR-4458, University of Maryland, College Park, 2003.
- [82] N. A. Gumerov and R. Duraiswami, “Comparison of the efficiency of translation operators used in the fast multipole method for the 3D Laplace equation”, UMIACS TR 2005-09, University of Maryland, College Park, 2005.
- [83] K. Li, M. Stockman, and D. J. Bergman, “Self-similar chain of metal nanospheres as an efficient nanolens”, *Phys. Rev. Lett.*, vol.91, 227402, 2003.
- [84] K. Sato, K. Hosokawa, and M. Maeda, “Rapid aggregation of gold nanoparticles induced by non-cross-linking DNA hybridization”, *J. Amer. Chem. Soc.*, vol.125, pp.8102-8104, 2003.
- [85] L. Tsang, J. A. Kong, K-H. Ding, *Scattering of Electromagnetic Waves — Theories and Applications*, John Wiley & Sons, 2000.
- [86] G. Dassios and R. Kleinman, *Low Frequency Scattering*, Oxford university press, 2000.

- [87] J. D. Jackson, *Classical Electrodynamics*, John Wiley and Sons Press, 3rd edition, 1999.